UNIVERSITY OF ROCHESTER
LABORATORY FOR LASER ENERGETICS

Volume 123
April–June 2010
DOE/NA/28302-964

LLE Review

Quarterly Report

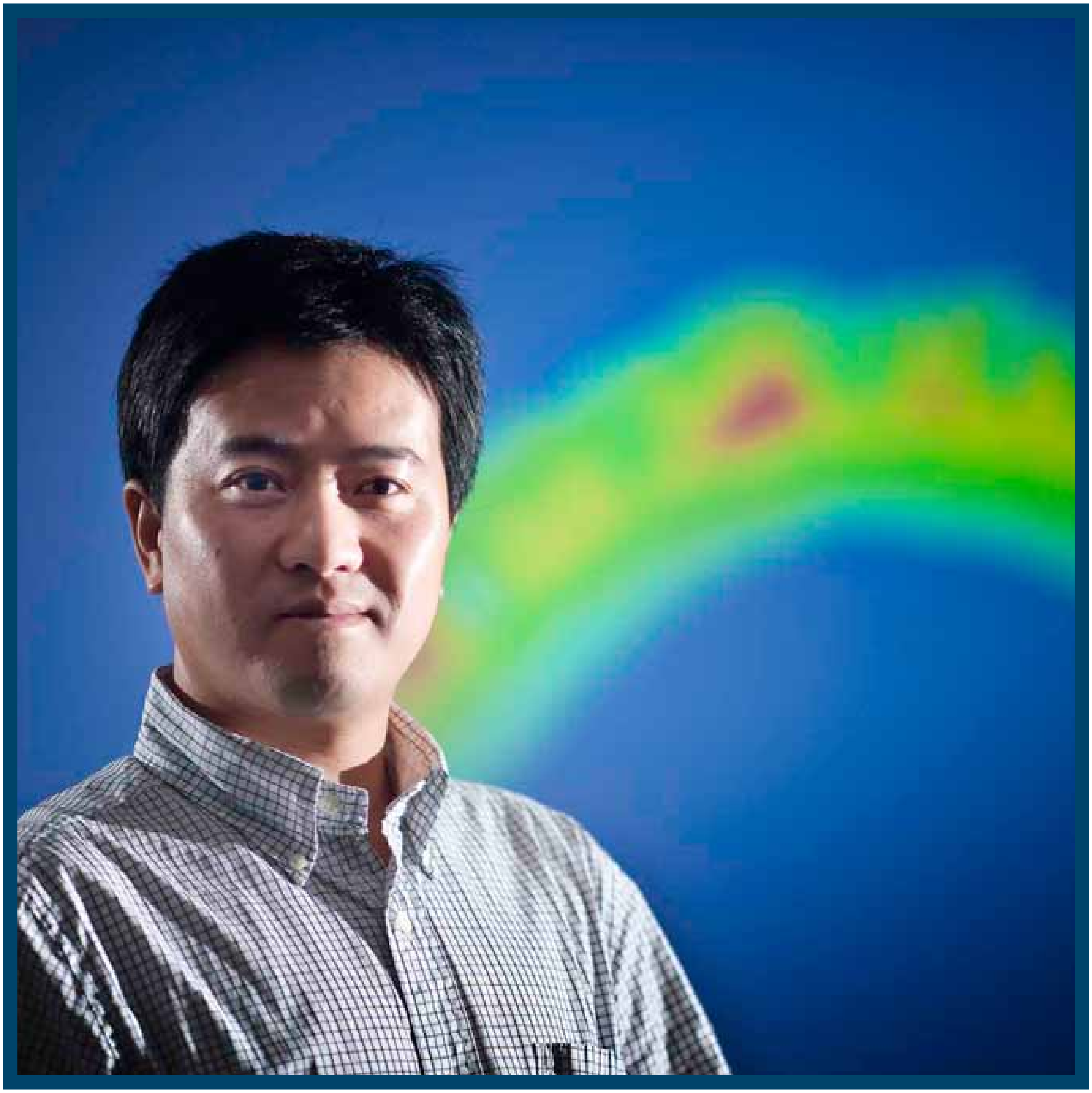

About the Cover:

The cover photo shows Dr. Suxing Hu, who led an effort to study the effects of various nonuniformities on neutron yield in cryogenic deuterium–tritium (DT) implosions on OMEGA (see p. 111). In the background is a contour map of density in an implosion from a two-dimensional *DRACO* simulation, including the actual laser and target perturbations observed in experiments. The authors investigated both large-scale (e.g., target offset, power imbalance, beam mistiming and mispointing) and small-scale (e.g., ice-surface roughness and beam imprinting) nonuniformities to identify and quantify the dominant sources. As a result of this work, Dr. Hu and his colleagues have proposed requirements for achieving yields on hydro-equivalent NIF-ignition targets that scale to minimum ignition conditions on the NIF.

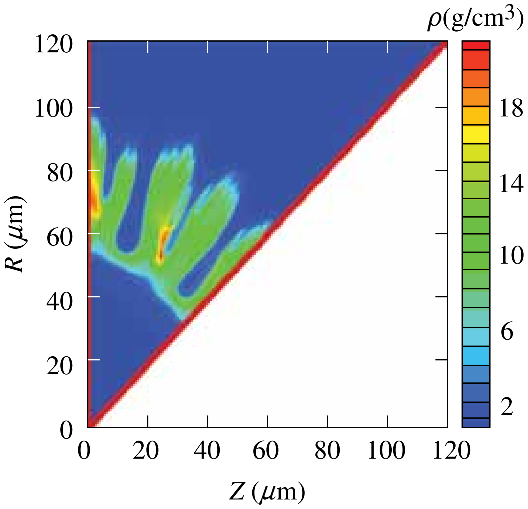

The image at the left shows a *DRACO* simulation (over a 45° wedge) of the effect of beam imprinting on a cryo-DT implosion. The plot shows density contours at the end of acceleration with the beam smoothed via smoothing by spectral dispersion (SSD). The density contours clearly show the "bubble" and "spike" growth characteristic of beam imprinting. Such nonuniformities significantly reduce neutron yield, although the use of SSD is predicted to reduce these effects by a factor of ~2.

The work described in this volume includes current research at the Laboratory for Laser Energetics, which is supported by New York State Energy Research and Development Authority, the University of Rochester, the U.S. Department of Energy Office of Inertial Confinement Fusion under Cooperative Agreement No. DE-FC52-08NA28302, and other agencies.

Printed in the United States of America
Available from
National Technical Information Services
U.S. Department of Commerce
5285 Port Royal Road
Springfield, VA 22161
Price codes: Printed Copy A04
Microfiche A01

For questions or comments, contact Brian E. Kruschwitz, Editor, Laboratory for Laser Energetics, 250 East River Road, Rochester, NY 14623-1299, (585) 273-5104.

Worldwide-Web Home Page: http://www.lle.rochester.edu/
(Color online)

UNIVERSITY OF ROCHESTER
LABORATORY FOR LASER ENERGETICS

Volume 123
April–June 2010
DOE/NA/28302-964

LLE Review

Quarterly Report

Contents

In Brief

This volume of the LLE Review, covering April–June 2010, features "Two-Dimensional Simulations of the Neutron Yield in Cryogenic-DT Implosions on OMEGA" by S. X. Hu, V. N. Goncharov, P. B. Radha, J. A. Marozas, S. Skupsky, T. R. Boehly, T. C. Sangster, D. D. Meyerhofer, and R. L. McCrory. The article (p. 111) reports the use of two-dimensional *DRACO* simulations to systematically investigate the impact of nonuniformities seeded by target and laser perturbations on neutron yield in cryogenic deuterium–tritium (DT) implosions. Two sources of nonuniformity accounted for observed neutron-yield reduction according to the *DRACO* simulations: target offset from the target chamber center and laser imprinting. The integrated simulations for individual shots reproduce the experimental yield-over-clean (YOC) ratio to within a factor of 2. Typically, the YOC in OMEGA experiments is ~5%. The simulation results suggest that YOC can be increased to the ignition hydro-equivalent level of 15% to 20% (with $\langle \rho R \rangle$ = 200 to 300 mg/cm^2) by maintaining a target offset of less than 10 μm and employing beam smoothing by spectral dispersion.

Additional highlights of research presented in this issue include the following:

- R. Epstein, J. A. Delettrez, V. N. Goncharov, P. W. McKenty, F. J. Marshall, D. D. Meyerhofer, P. B. Radha, S. P. Regan, T. C. Sangster, V. A. Smalyuk, W. Theobald, and B. Yaakobi (LLE); R. Tommasini, N. Landen, and A. MacKinnon (LLNL); and M.-J. Tsay and M. Young (LLE Summer High School Research Program) describe the use of x-ray radiography to characterize cryogenic implosions on OMEGA (p. 128). The first radiographs of cryogenic implosions on OMEGA have been obtained using short-pulse, K-shell emission-line backlighters driven by the OMEGA EP laser. Simulations show that radiography near peak compression is feasible. Backlighter composition is chosen so that the emission lines occur at energies where the opacity profiles of the imploded cores will provide a measurable range of optical depth, and the specific intensity of the backlighter is capable of overcoming the core self-emission. Simulations of the first measured implosion radiographs are used to assess the implosion performance at times in advance of peak compression. Radial mass distributions are obtained from the radiographs using Abel inversion and the known temperature and density dependence of the free-free opacity of the hydrogen shell. Radiography based on Compton scattering of hard backlight x rays is being investigated as an alternative approach. The relative advantages of both methods of radiography are compared.
- C. Stoeckl, M. Cruz, V. Yu. Glebov, J. P. Knauer, K. L. Marshall, C. Mileham, T. C. Sangster, and W. Theobald (LLE), and R. Lauck (Physikalisch Technische Bundesanstalt, Braunschweig, Germany) have developed a gated liquid-scintillator–based neutron detector to be used for fast-ignitor experiments and down-scattered neutron measurements (p. 145). The detection of neutrons in these experiments is very challenging since it requires the neutron-detection system to recover within 50 to 500 ns from a high background signal many orders of magnitude stronger than the signal of interest. The background signal is either the hard x-ray emission from a short-pulse laser interaction with a target for the fast-ignitor experiments or the primary neutron signals for the down-scattered neutron measurement. The liquid-scintillator–based detector uses a gated microchannel photomultiplier that suppresses the high background signal and an oxygen-enriched liquid scintillation material that eliminates the afterglow present in conventional plastic scintillators.

- W. Wang and T. B. Jones (Department of Electrical and Computer Engineering, University of Rochester), and D. R. Harding (LLE and Department of Chemical Engineering, University of Rochester) describe an on-chip double emulsion droplet assembly for laser-target fabrication (p. 149). The double emulsion droplets used to fabricate cryogenic foam targets for inertial confinement fusion experiments require precisely controlled volumes. On-chip, electric-field–actuated, microfluidic assembly of double emulsion droplets can be used to achieve such precision. The electrowetting-on-dielectric and dielectrophoresis effects make it possible to manipulate both conductive and dielectric droplets simultaneously on a substrate. Aqueous and non-aqueous liquid droplets precisely dispensed from two reservoirs on a microfluidic chip are transported and combined to form oil-in-water-in-air or water-in-oil-in-air double emulsion droplets. The dispensing reproducibility is studied as a function of a set of operation parameters. Conditions for spontaneous emulsification for double emulsion formation are developed in terms of droplet surface energies.

- F. J. Marshall, T. DeHaas, and V. Yu. Glebov report on a study of charge-injection-device performance in the high-energy-neutron environment of laser-fusion experiments (p. 159). Charge-injection devices (CIDs) are being used to image x rays in laser-fusion experiments on the OMEGA Laser System, up to the maximum neutron yields generated ($\sim 10^{14}$ DT). The detectors are deployed in x-ray pinhole cameras and Kirkpatrick–Baez microscopes. The neutron fluences ranged from $\sim 10^7$ to $\sim 10^9$ neutrons/cm^2, and useful x-ray images were obtained even at the highest fluences. It is intended to use CID cameras at the National Ignition Facility (NIF) as a supporting means of recording x-ray images. The results of this work predict that x-ray images should be obtainable on the NIF at yields up to $\sim 10^{15}$, depending on distance and shielding.

Brian E. Kruschwitz
Editor

Two-Dimensional Simulations of the Neutron Yield in Cryogenic-DT Implosions on OMEGA

Introduction

Inertial confinement fusion (ICF) has been actively pursued for decades[1] since it was proposed in the early 1970s (Ref. 2). In the so-called "hot-spot" ignition designs, a capsule containing a cryogenic deuterium–tritium (DT) ice layer and low-density DT gases is imploded directly by intense laser pulses[3] or indirectly by x rays in a hohlraum.[4] The ultimate goal of ICF is to ignite the imploding target, producing net energy gain. To reach this goal, the cryogenic-DT shell must be sufficiently low in temperature that it can be compressed to an extremely high density (>1000× solid-DT density), resulting in an areal density ($\rho R \geq 1$ g/cm^2) to provide sufficient inertial confinements for burn-wave propagation. The temperature in the hot spot must be sufficiently high so that the resulting fusion α particles can "trigger" the burn-wave propagation for ignition. Both conditions are necessary for the success of hot-spot ICF ignition. Nonuniformities seeded by target and laser perturbations grow exponentially via Rayleigh–Taylor (RT) instability[5] during the acceleration and deceleration of the fuel shell. This perturbation growth can disrupt the neutron yield (α-particle production) from the core through cooling the hot spot by either injecting "cold" material into the core or increasing heat flow out of the hot spot because of the increased surface area. This reduces the effective hot-spot volume, density, and temperature.[6] The yield-over-clean (YOC), defined as the ratio of experimental neutron yield to its value from one-dimensional (1-D) simulations, is conventionally used to describe the neutron-yield reduction caused by perturbations. It has been shown[7] that a minimum YOC requirement ($\text{YOC}_{\text{min}} \geq 40\%$ to 50%) must be met at the National Ignition Facility (NIF)[8] for both direct- and indirect-drive–ignition designs to be successful. By scaling the hydro-equivalent NIF-ignition designs to OMEGA, it has been suggested that the YOC of cryogenic-DT implosions on OMEGA should be ~15% to 20% (Ref. 7) to have confidence that a scaled NIF target will ignite.

Over the past years RT growth of various perturbations has been extensively studied for both planar and spherical targets through theoretical analyses/simulations[9] and experiments.[10–14] These perturbations include the target offset from target chamber center, the ice roughness of the cryogenic-DT layer, and the laser nonuniformities. Understanding the effects of each of the perturbation sources and their combination on the neutron-yield reduction through multidimensional simulations compared with experiments is critical to identifying the major nonuniformity sources that should be improved. For ICF ignition designs, the perturbation growth generally depends on the target design and laser pulse shapes. A comprehensive study of cryogenic deuterium (D_2) implosions on OMEGA[15] has been presented in Ref. 16. As opposed to the cryogenic-D_2, continuous-pulse implosions, the high-compression [$\langle \rho R \rangle >$ 200 mg/cm^2] cryogenic-DT implosions are driven by triple-picket designs with a higher convergence ratio and small hot spot. This article is devoted to a thorough understanding of the neutron-yield performance in cryogenic-DT implosions on OMEGA.[17,18] Two-dimensional (2-D) *DRACO*[19] simulations have been performed to systematically investigate each of the perturbation sources and their combined effects on the neutron yield. The *DRACO* simulations reproduced the trends observed in experiments. The simulated YOC's agree with the experimental YOC within a factor of 2 or better, and the simulated neutron-averaged ion temperatures agree with measurements within the experimental uncertainty. Major nonuniformity sources are identified for the triple-picket plus step-pulse designs:[17,18] the target offset with respect to the target chamber center and laser imprinting. This is in contrast to the cryogenic-D_2 implosions[16] where the ice-layer roughness is much more dominant. The simulations of DT implosions suggest that to increase YOC from the current level of ~5% to the hydro-equivalent ignition level of ~15% to 20% (maintaining $\langle \rho R \rangle$ = 200 to 300 mg/cm^2), the target offset must be less than ~10 μm and smoothing by spectral dispersion (SSD) must be applied.

The following sections (1) briefly describe the experiments and the basics of 2-D radiation–hydrodynamic simulations for cryogenic-DT implosions, respectively; (2) describe the detailed simulation results that examine each of the nonuniformity sources and their combined perturbation effects on the neutron-yield reduction; (3) discuss the integrated *DRACO* simulations for individual cryogenic-DT shots by including the actual target and laser nonuniformities in experiments; (4) compare the simulated YOC and the neutron-averaged ion temperature with experiments; and (5) formulate the relationship between YOC and the temperature-over-clean (TOC), indicating how much distortion occurs in the hot-spot formation. Conclusions are presented in the last section.

Experiments of Cryogenic-DT Implosions on OMEGA

Low-adiabat ($\alpha \sim 2.0$ to 2.5, which is conventionally defined as the ratio of DT-fuel pressure to the Fermi-degenerate pressure), cryogenic-DT implosion experiments have been conducted on OMEGA with the multiple-picket drive pulses[17,18] shown in Figs. 123.1(a) and 123.1(b). The targets, shown in Fig. 123.1(c), were energy scaled from the ignition design on the National Ignition Facility (NIF).[17] The OMEGA target had an 860-μm diameter, with an ~10-μm plastic (CD) ablator filled with approximately 650 atm of DT (nominally 50:50) gas at standard temperature and pressure. When cooled to the triple point (approximately 18.7 K), a DT-ice layer (~65 μm thick) formed inside the shell. The targets were mounted on 17-μm-diam SiC stalks. The triple-picket design[17,18] is motivated by the desire to precisely tune the multiple shock waves to maintain a low-implosion adiabat and to minimize shock preheating of the fuel. The pickets launch a series of decaying shocks that are designed to coalesce nearly simultaneously with the main shock near the inner surface of the cold fuel. Shock-timing measurements in liquid deuterium with a velocity interferometer system for any reflector (VISAR)[20] are used to obtain a laser pulse shape that places the DT fuel on the desired adiabat. By adjusting the picket energies, low-adiabat ($\alpha \sim 2$), high-compression [$\langle \rho R \rangle_n \sim 300 \pm 47$ mg/cm^2 inferred by a magnetic recoil spectrometer (MRS)[21]] implosions have been demonstrated on OMEGA.[17,18]

For the OMEGA cryogenic-DT experiments, both the triple-picket (TP) plus square main pulse [Fig. 123.1(a)] and triple-picket plus step main pulse [Fig. 123.1(b)] have been used to drive target implosions. The former design resulted in an in-flight adiabat of $\alpha \sim 2.5$ and a convergence ratio of $C_R \sim 19$, while the step main pulse drove a lower-adiabat ($\alpha \sim 2.0$) implosion with a higher convergence ratio of $C_R \sim 24$ (resulting in higher $\langle \rho R \rangle$). The total laser energy was 23 kJ for the square main pulse and 25 kJ for the step main pulse. With a peak intensity of ~8×10^{14} W/cm^2, the predicted implosion velocity in these designs is $v_{\text{imp}} = 3 \times 10^7$ cm/s. Details of the compression dynamics, the areal-density (ρR) measurement, and the triple-picket ignition design for the NIF can be found in Refs. 17 and 18.

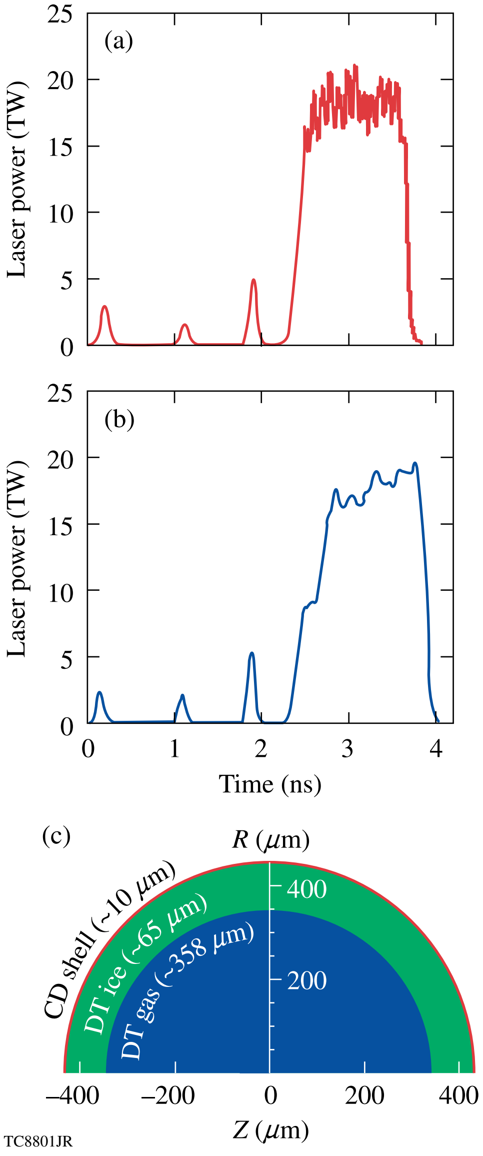

Figure 123.1
(a) The triple-picket plus square main pulse and (b) the triple-picket plus step main pulse used for cryogenic-DT implosions on the OMEGA laser. (c) A schematic diagram of a cryogenic-DT target.

The neutron yields from DT fusion were measured with a combination of activation, scintillation, and track recorder detectors. The yield of these implosions, 1×10^{12} to 6×10^{12} neutrons, varied from ~3% to ~10% of the 1-D hydrodynamic simulation prediction, depending on the pulse shape, target offset, ice roughness, and beam smoothing. The neutron-averaged ion temperature ($\langle T_i \rangle_n$) was inferred using neutron time-of-flight spectroscopy.[22] The accuracy of these measurements was approximately ±0.5 keV, depending on the measurement configuration and the neutron-hit statistics in the detectors. Improvements to reduce the error bar in $\langle T_\mathrm{i}\rangle_\mathrm{n}$ measurements are underway. The measured $\langle T_\mathrm{i}\rangle_\mathrm{n}$ and the absolute neutron yields are lower than the 1-D–predicted values, as a consequence of laser and target perturbations including ice roughness, laser-drive nonuniformity (primarily pointing- and single-beam nonuniformity), capsule-surface imperfections associated with the stalk mount, and target offsets from the locus of laser-beam pointing. The subsequent sections provide a systematic investigation of how these nonuniformities reduce the neutron yield and the ion temperature in the hot spot. The simulations are used to identify the major perturbation sources and to suggest possible improvements for the implosion-yield performance.

Two-Dimensional *DRACO* Simulations

To understand the various laser and target perturbation effects on the cryogenic-DT implosion experiments, multidimensional hydrodynamic simulations were performed. The two-dimensional, radiation hydrodynamics code *DRACO* has been developed at LLE for both implosion and planar-target simulations.[19] For spherical implosion simulations, the *DRACO* coordinates are defined by the cylindrical axis **Z** and the radius **R**, with the assumption of azimuthal symmetry. This study used *DRACO*'s Lagrangian version. Laser absorption in the plasma corona by inverse bremsstrahlung was modeled by three-dimensional (3-D) ray tracing with OMEGA's port geometry.[23] The equation-of-state (EOS) of materials was determined from the *SESAME* EOS table.[24] The radiation transport in *DRACO* used the multigroup diffusion model, in which the Astrophysics Opacity Table (AOT)[25] is applied.

In direct-drive ICF implosions, the laser energy absorbed near the critical-density region is thermally transported to the ablation surface mainly by electrons. The thermal-transport model in direct-drive ICF is crucial for properly simulating the target drive. Flux-limited Spitzer thermal conductivity is often used in laser–plasma fluid modeling.[26] The standard flux limiter $f = 0.06$ was used in the 2-D simulations. Previous experiments with planar and spherical targets[27–29] have shown that this flux limiter works well for the laser intensities used here. The 1-D simulations of the cryogenic-DT implosions were modeled using both classical (flux-limited) heat transport and a nonlocal heat-transport model[30] and were found to be insensitive to the transport model.

A series of planar and spherical experiments were conducted to benchmark the *DRACO* simulations.[11–14,16,19,29,31,32] The code capability of simulating the Rayleigh–Taylor instability growth has been demonstrated with intense laser-driven planar/spherical target experiments on OMEGA.[11–14] The RT growth of perturbations either by pre-imposed mass modulation[11,12] or by direct laser imprinting[13,14] has been properly predicted by *DRACO* simulations. A systematic study of the neutron yield in cryogenic-D_2 implosions on OMEGA was performed with 2-D *DRACO* simulations.[16] The simulation results generally reproduced the experimental trend in YOC versus target offset and ice roughness for 5-μm-thick CD-shell targets, while for 10-μm-thick CD-shell targets, laser imprinting reduced the yield by a factor of 2. Following our previous experience in simulating cryogenic-D_2 implosions, cryogenic-DT implosions are systematically investigated for each of the perturbation sources and their combined effects on the yield performance. Comparing simulations with experiments elucidates the major perturbations and suggests how to increase the neutron yield in the experiments.

Simulation Results for Various Laser and Target Perturbations

In cryogenic-DT experiments, a variety of laser and target perturbations determine the implosion performance. Two kinds of laser perturbations will be addressed: (a) long-wavelength beam-to-beam perturbations ($\ell < 20$) such as mistiming, mispointing, and power imbalance among beams and (b) single-beam laser imprinting in the high-mode regime (up to $\ell \sim 200$). The target perturbations include the target offset from the target chamber center and the inner surface roughness of the ice layer. In this section, each of the nonuniformity sources will be investigated separately and their combined effect on yield performance will be examined.

1. Long-Wavelength Laser Nonuniformities

The 60-beam OMEGA Laser Facility[15] can deliver up to 30-kJ, 351-nm UV energies on target. Each laser beam, coming from ports in a 3-D geometry, is equipped with a super-Gaussian (SG-4) phase plate[33] and polarization smoothing[34] is employed. The low-mode (long-wavelength) perturbation effects include the power imbalance (PIB) among beams, the beam-to-beam mistiming (MT), and the static mispointing (MP) of each beam. Their effects have been investigated separately with *DRACO* simulations of cryogenic-DT target performance using different levels of perturbation σ_rms. The results are summarized in Tables 123.I–123.III. A normal distribution of random perturbation amplitudes from each laser beam is assumed for a given σ_rms. For example, Table 123.I shows that for the square main pulse, the YOC decreases from 94.1% to 81.1% as the mistiming changes from σ_rms = 9 ps to σ_rms = 40 ps. Table 123.II shows that a static mispointing of σ_rms = 50 μm reduces the YOC to 65%. For power imbalance among the beams, the pickets' power imbalance is more important than the main drive pulse because the PIB nonuniformity can be more efficiently seeded during the pickets. As shown in Table 123.III, a PIB of σ_{rms} = 10% during the pickets can reduce the YOC to 74%, even when the main pulse's PIB is σ_{rms} = 3%. This level of PIB during the pickets has been seen in cryogenic-DT experiments. The PIB in cryogenic-DT pulse shapes has recently been improved to an overall σ_{rms} = 3% to 4%, which recovers the YOC to a level of ~90%.

Table 123.I: YOC dependence on beam-to-beam mistiming for the square main pulse.

Beam-to-beam mistiming	YOC (%)
σ_{rms} = 9 ps	94.1
σ_{rms} = 25 ps	90.4
σ_{rms} = 40 ps	81.1

Table 123.II: YOC dependence on beam mispointing for the step main pulse.

Static beam mispointing	YOC (%)
σ_{rms} = 10 μm	91.9
σ_{rms} = 30 μm	77.0
σ_{rms} = 50 μm	65.0

Table 123.III: YOC dependence on beam-power imbalance for the step main pulse.

Beam-power imbalance	YOC (%)
σ_{rms} = 3% (pickets) and 3% (main pulse)	92.9
σ_{rms} = 3% (pickets) and 10% (main pulse)	90.3
σ_{rms} = 10% (pickets) and 3% (main pulse)	74.0

By using a nominal laser perturbation level for each source on OMEGA, the simulation results of their combined effects on the cryogenic-DT yield performance are listed in Table 123.IV for both pulse shapes. The combined effects of the three nominal perturbations (MT: σ_{rms} = 9 ps; MP: σ_{rms} = 10 μm; PIB: σ_{rms} = 3% overall) reduce the yield by ~7% for the square main pulse and by ~17% for the step main pulse. The latter is more sensitive to perturbations since it drives a lower-adiabat, high-convergence implosion. In the following sections, these nominal low-ℓ-mode laser nonuniformities have been included since they are always present in OMEGA experiments.

2. Target Offset

The target can be offset from the target chamber center as a result of vibration when the cryogenic shroud is retracted. It is measured at shot time using time-integrated x-ray pinhole cameras. As shown in cryogenic-D_2 implosions,[16] the target offset imposes a dominant $\ell = 1$ perturbation. This is due to the asymmetry of laser illumination on the target, which results in less laser absorption in the offset direction. As a result, the shock breaks out asymmetrically and the overdriven side converges more and achieves a higher density. The uneven drive compresses the target asymmetrically, reducing the final hot-spot volume, temperature, and density. The density contours for the square-main-pulse design are plotted in Figs. 123.2(a) and 123.2(b) at peak compression for the cases of 20-μm and 40-μm offsets from the target chamber center. The corresponding ion-temperature contour plots are shown in Figs. 123.2(c) and 123.2(d). As the target offset increased, the compression asymmetry increased; the ion temperature and effective volume for neutron production in the hot spot were reduced, leading to a reduction in neutron yield. The target offsets of 20 μm and 40 μm caused the YOC to decrease to 72% and 36.4%, respectively.

Carrying out *DRACO* simulations for different target offsets, the YOC was plotted as a function of target offset in Fig. 123.3 for both the square main pulse (red circles) and the step main

Table 123.IV: YOC degradation caused by the smallest low-mode beam perturbations on OMEGA.

Smallest OMEGA beam nonuniformities	YOC (%) (square main pulse)	YOC (%) (step main pulse)
Mistiming (σ_{rms} ~ 9 ps)	94.1	92.2
Mispointing (σ_{rms} ~ 10 μm)	93.8	91.9
Power imbalance (σ_{rms} ~ 3% overall)	93.6	92.9
All above perturbations together	93.4	83.3

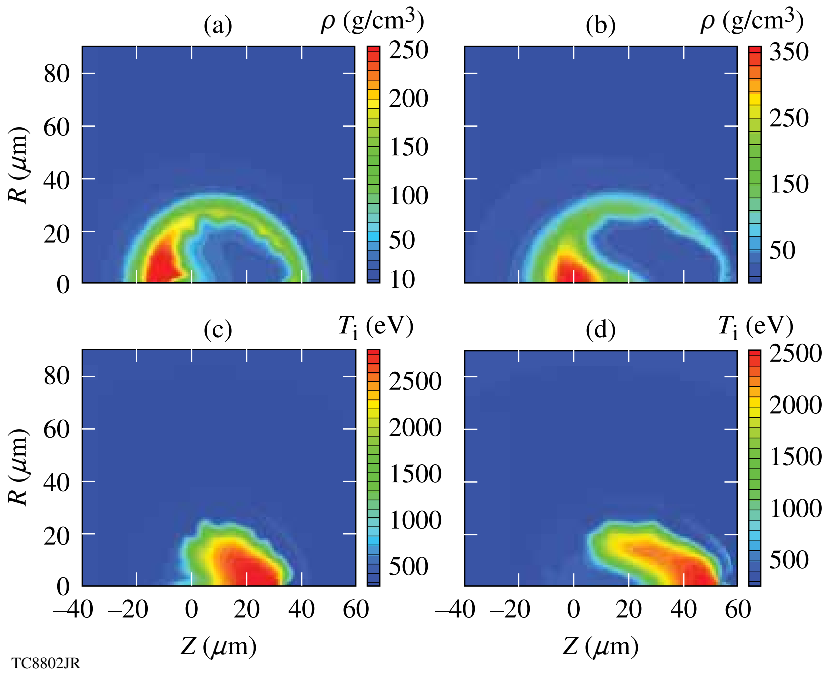

Figure 123.2
The density contour plots at peak compression for target offsets of (a) 20 μm and (b) 40 μm from the target chamber center, for the square-main-pulse case. The corresponding ion temperatures are shown in (c) and (d), respectively.

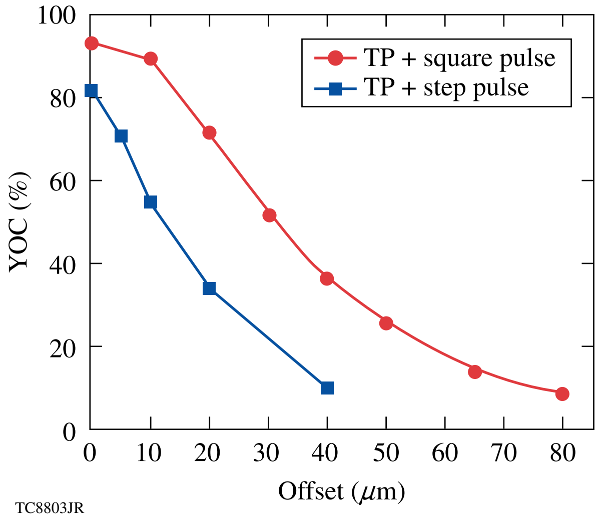

Figure 123.3
The YOC is plotted as a function of target offset for the two types of pulses shown in Figs. 123.1(a) and 123.1(b).

pulse (blue squares). The step main pulse is more sensitive to the target offset than the square main pulse. For example, at 20-μm offset the YOC is ~72% for the square main pulse, while it is ~34% for the step-main-pulse design. This factor of ~2 reduction is consistent with the experimental observations for these two pulse shapes (see ***DRACO* Simulations of Individual Cryogenic-DT Shots**, p. 122). The dominant $\ell = 1$ perturbation has been confirmed by experimental ρR measurements. As shown in Fig. 123.2(b), if the ρR detector is sitting along the $+z$ axis (along the target offset), it measures the smallest ρR; while, if it sits on the $-z$ axis (against the target offset), it will measure the largest ρR. Indeed, two shots with large offsets (35 μm and 39 μm) have shown such asymmetric ρR results [$\langle \rho R\rangle_{\text{CPS}_1}$ = 50 mg/cm^2 and $\langle \rho R\rangle_{\text{CPS}_2}$ = 180 mg/cm^2], experimentally inferred from the knock-on-deuteron (KOd) spectrum following elastic (n,D) scattering.[35] For these two shots, the two charged-particle spectrometers (CPS$_1$ and CPS$_2$) were roughly in line with the direction of target offset. The shape of the KOd spectrum evolves dramatically as the fuel areal density increases up to 180 mg/cm^2; above 180 mg/cm^2, the shape of the spectrum no longer changes with increasing areal density and the measurement is saturated.[35]

3. Ice Roughness

For the cryogenic-DT targets imploded on OMEGA, 10-μm CD shells were permeation filled with an equimolar mixture of DT to 650 atm. The shell and gas were then slowly cooled to just below the DT triple point (18.7 K). By controlling the exchange-gas pressure and the temperature of the copper-layering sphere, a spherical isotherm can be maintained at the ice surface inside the capsule, and β-layering produces high-quality layers.[36,37] During formation of the ice layer, the inner ice surface was characterized using optical shadowgraphy.[38] A typical shadowgraph of a cryogenic-DT target is shown in Fig. 123.4(a); the inner-surface position is "unwrapped" azimuthally around the center of the capsule to form a line in

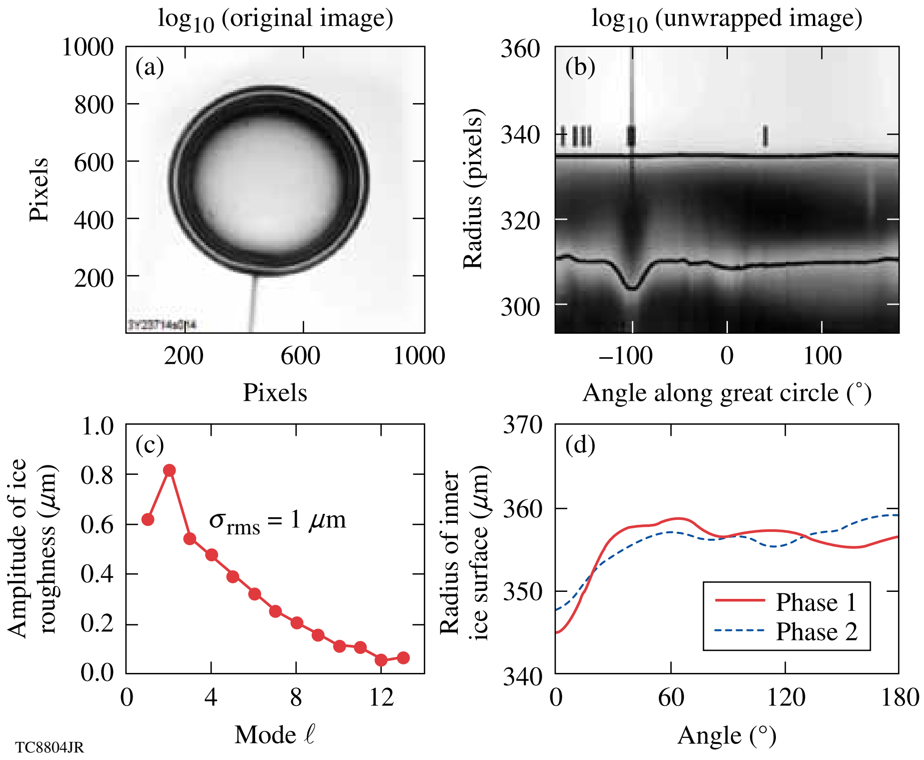

Figure 123.4
(a) A typical cryogenic-DT target view; (b) the ice-layer radius plotted versus angle; (c) a typical spectrum of ice roughness ($\sigma_{\text{rms}} = 1.0\ \mu$m) at the inner surface (the thick part near the stalk has been excluded); (d) the angle-dependent radius of the inner ice surface for two different phases but same σ_{rms}, which were composed for our *DRACO* simulations.

radius–azimuth space [Fig. 123.4(b)]. Figure 123.4(c) shows the typical power spectrum of the ice roughness ($\sigma_{\text{rms}} = 1\ \mu$m) as a function of the mode number, which was generated by fitting the Fourier amplitudes of the radial variation as a function of the azimuth.[39] Using the measured spectrum, the ice-layer thickness (ΔR) was composed for the *DRACO* simulations,

$$\Delta R(\theta) = \Delta R_0 + \sum_{\ell=1}^{n} \pm A_\ell \cos(\ell\theta), \qquad (1)$$

where ΔR_0 is the average thickness of the ice layer and A_ℓ is the perturbation amplitude of the ℓth mode. Because of the azimuthal symmetry imposed in 2-D *DRACO*, the phase among different modes must be either 0 or π, giving a plus (+) or minus (–) sign in the superposition of each mode. Different combinations of these signs provide various "phases" of the ice layer, which give different perturbed shell thicknesses along the polar angle θ, even though σ_{rms} is the same. The inner-surface radius as a function of angle has been plotted in Fig. 123.4(d) for two such phases, respectively, by solid (red) and dashed (blue) lines. The "dips" in radius around the stalk were modeled with the superposition of a Gaussian bump, around $\theta = 0°$.

Different phases of ice roughness can vary the target-yield performance. Examples are shown in Figs. 123.5(a) and 123.5(b) for density contours at peak compression for phase 1 and phase 2 [shown in Fig. 123.4(d)], respectively, at $\sigma_{\text{rms}} = 1.0\ \mu$m with the step main pulse. The simulations show a neutron yield of YOC = 78% for phase 1 and YOC = 56% for phase 2. The "ice bump" around the stalk has not yet been included in the ice-roughness-only studies but will be included in the individual shot simulations. Considering only the ice roughness (without the localized ice bump), Fig. 123.5(c) shows the YOC as a function of ice roughness σ_{rms} from *DRACO* simulations for both $\sigma_{\text{rms}} = 1.0\ \mu$m and $\sigma_{\text{rms}} = 3.0\ \mu$m with three random phases. The error bar for each case represents the range of YOC's caused by the different phases. As expected, the YOC decreases with increasing ice roughness.

4. Combined Target Offset and Ice Roughness

The combined effects of target offset and ice roughness on cryogenic-DT implosion yields are studied in this subsection. Both pulse shapes shown in Figs. 123.1(a) and 123.1(b) are simulated for ice roughnesses of $\sigma_{\text{rms}} = 1.0\ \mu$m and σ_{rms} =

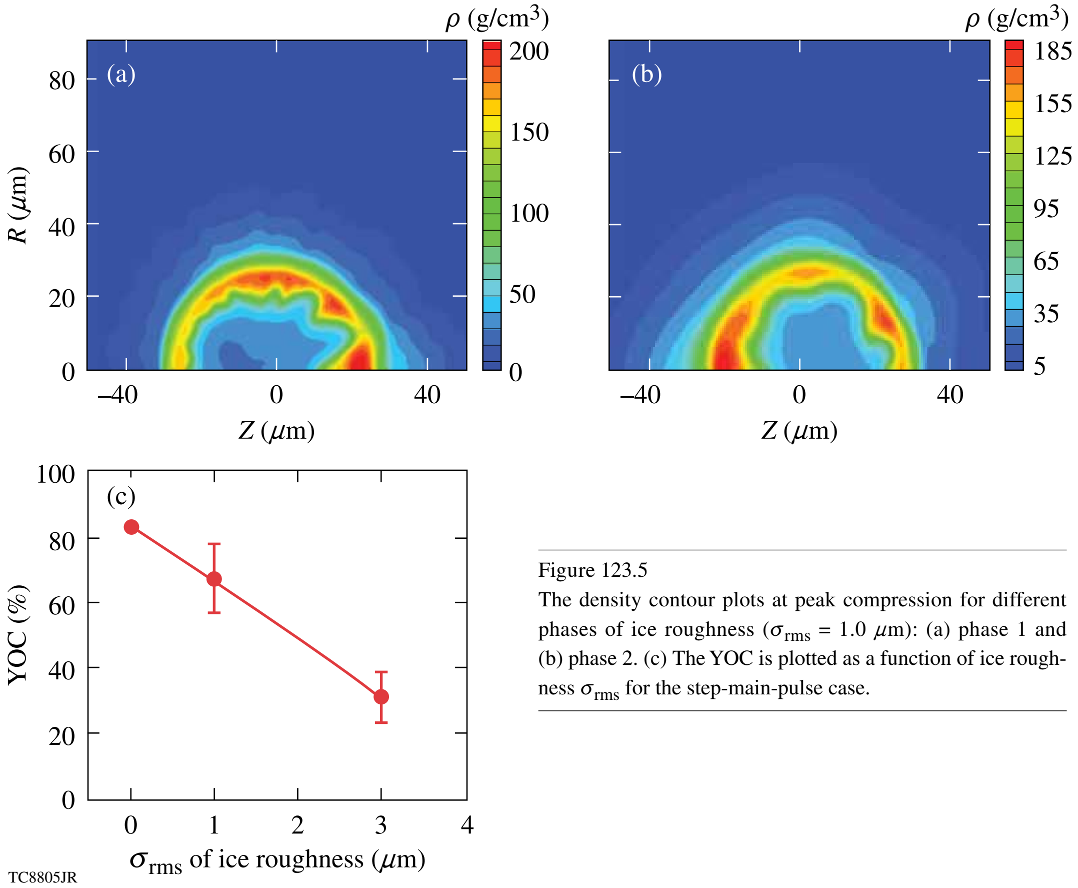

Figure 123.5
The density contour plots at peak compression for different phases of ice roughness (σ_{rms} = 1.0 μm): (a) phase 1 and (b) phase 2. (c) The YOC is plotted as a function of ice roughness σ_{rms} for the step-main-pulse case.

3.0 μm. The simulation results are shown in Figs. 123.6 and 123.7, respectively, by red circles (square main pulse) and blue squares (step main pulse). For the typical cryogenic-DT target ice roughness (σ_{rms} = 1.0 μm), Fig. 123.6 shows that the step main pulse resulted in more yield reduction than the square main pulse, again because of its lower adiabat and higher convergence. At an offset of about 20 μm, the square main pulse gives a factor-of-2-higher YOC than the step-main-pulse case, which is consistent with the experimental observation (discussed in ***DRACO*** **Simulations of Individual Cryogenic-DT Shots**, p. 122). A steeper drop in YOC is found for a target offset larger than 10 μm, especially for the step-main-pulse design, as illustrated in Fig. 123.6.

At a large ice roughness σ_{rms} = 3.0 μm, the YOC difference between the two pulse shapes is no longer significant since an increase in ice roughness dominates the performance and reduces the YOC to 30% to 40% (indicated by Fig. 123.7), even for target offsets ≤30 μm. The step main pulse is more sensitive to the phase of the ice roughness, as indicated by the large YOC ranges in Fig. 123.7. To reach a high YOC level (≥50%), the target must have a small offset (≤10 μm for the step pulse and ≤20 μm for the square pulse) and maintain a high-quality ice layer (ice roughness σ_{rms} ≤ 1 μm).

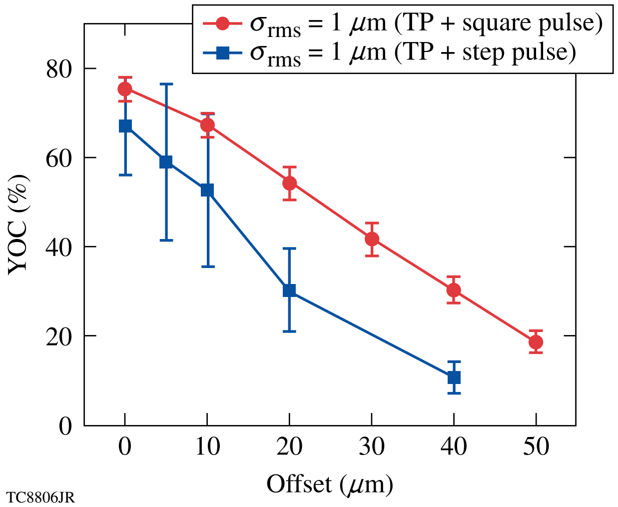

Figure 123.6
The YOC is plotted as a function of target offset with ice roughness σ_{rms} = 1.0 μm for the two pulse shapes shown in Figs. 123.1(a) and 123.1(b).

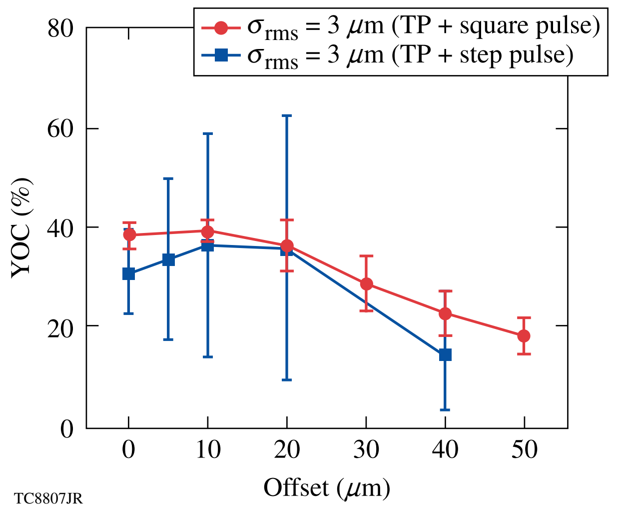

Figure 123.7
Same as Fig. 123.6 but for ice roughness σ_{rms} = 3.0 μm.

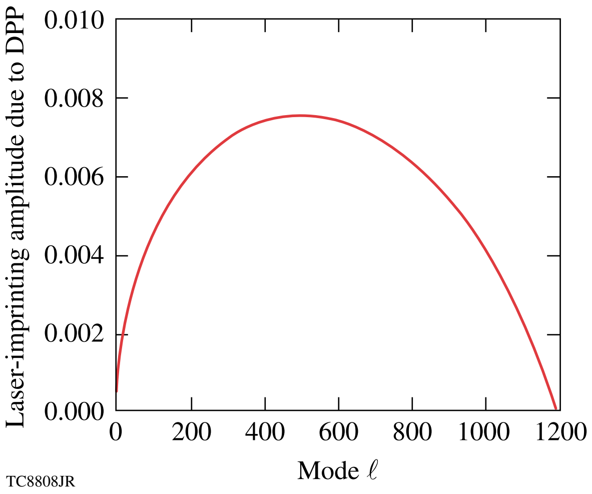

Figure 123.8
A typical SG-4 DPP spectrum on the OMEGA laser.

5. Laser Imprinting

Laser nonuniformities seed the instabilities at the ablation surface and can be categorized into long- and short-wavelength perturbations. The long-wavelength perturbations caused by beam mistiming, beam mispointing, and power imbalance have been discussed in **Long-Wavelength Laser Nonuniformities**, p. 113. The short-wavelength, single-beam nonuniformity caused by laser imprinting is addressed here.[40] An analytical model[41] describing the nonuniformity of super-gaussian (SG) distributed phase plates (DPP's) is used to modulate the laser illumination on target. The experimentally confirmed SG-4 DPP spectrum[42] is shown in Fig. 123.8. Polarization smoothing reduces the amplitudes by $\sqrt{2}$ (Ref. 34). Smoothing by spectral dispersion (1-THz, 2-D SSD) with one-color cycle[43] is applied for some shots. SSD is simulated using an analytical model.[44] The amplitudes of laser imprinting at the ablation surface are defined at the outer 1/e point of maximum density. These amplitudes seed the RT growth during the acceleration phase. Laser-imprinting effects are considered for both SSD-on and SSD-off cases.

Single-mode laser-imprinting simulations for the step-main-pulse design up to mode ℓ = 500 were performed with *DRACO* simulations either in a 45° wedge or in a half sphere. The resulting modulation amplitude at ablation surface is plotted as a function of time in Figs. 123.9(a)–123.9(d) for laser-imprinting modes $\ell = 30$ ($\lambda \approx 73.3$ μm), $\ell = 120$ ($\lambda \approx 18.3$ μm), $\ell = 200$ ($\lambda \approx 11.0$ μm), and $\ell = 400$ ($\lambda \approx 5.5$ μm), respectively.

The SSD-off cases are represented by dashed (red) curves and the SSD-on cases by solid (green) lines. For mode $\ell = 30$, Fig. 123.9(a) shows continuous imprinting before the start of acceleration at $t \approx 2.8$ ns. For modes $\ell \geq 120$, the laser imprinting decoupled during the first picket, when the distance from the laser deposition to the ablation surface became larger than the imprinting wavelength. The Richtmyer–Meshkov and preliminary RT growth caused by the unstable interference between the CD shell and the ice layer increase the amplitude. Phase reversals are seen in the high-mode laser-imprinting simulations, shown in Figs. 123.9(b)–123.9(d). After the acceleration starts at $t \approx 2.8$ ns, the $\ell = 30$ mode continuously grows until the end of acceleration ($t = 3.98$ ns), while the high modes of $\ell = 200$ and $\ell = 400$ quickly grow and nonlinearly saturate. The intermediate mode $\ell = 120$ grows linearly for about 600 ps; when its amplitude reaches ~10% of its wavelength, nonlinear behavior in RT growth begins. This can be seen in Fig. 123.10(a) where the Fourier transform of the single mode ($\ell = 120$) at the ablation surface (SSD on) is shown at two distinct times of $t = 3.4$ ns and $t = 3.96$ ns. At $t = 3.4$ ns, the $\ell = 120$ mode grows linearly, but at $t = 3.96$ ns, harmonics emerge as evidence of nonlinear growth.[9] At the end of the acceleration phase, the shell radius converges to $R = 100$ μm so that for the $\ell = 120$ mode, its wavelength is about ~5 μm, but $\lambda = 21$ μm for a low mode $\ell = 30$. At $t = 3.96$ ns, the $\ell = 120$ mode grows to an amplitude of ~0.8 μm [see Fig. 123.9(b)], which is ~16% of its wavelength. The mode $\ell = 120$ becomes nonlinear at the end of acceleration. For the low-mode $\ell = 30$

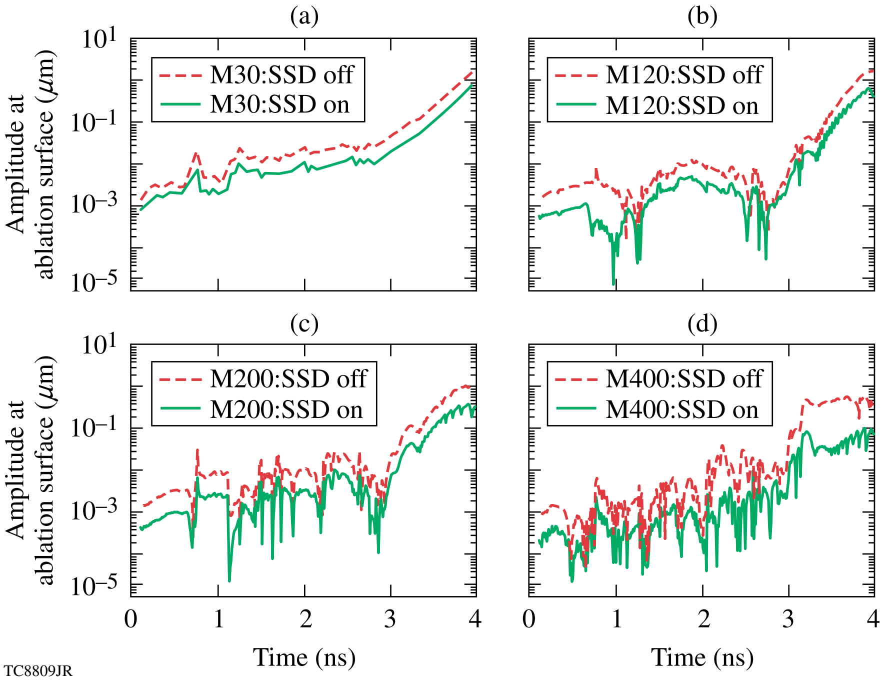

Figure 123.9
The laser-imprinting mode growth as a function of time for both SSD-off and SSD-on cases from single-mode simulations: (a) $\ell = 30$, (b) $\ell = 120$, (c) $\ell = 200$, and (d) $\ell = 400$.

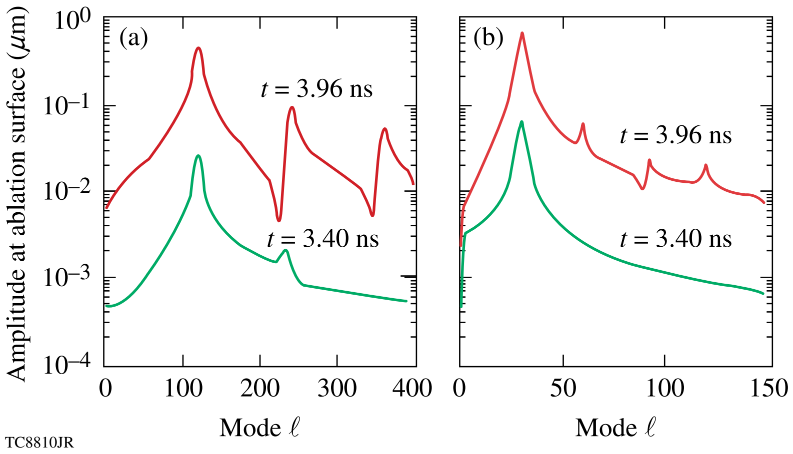

Figure 123.10
The modal spectrum for our single-mode simulations (SSD on) at two distinct times $t = 3.40$ ns and $t = 3.96$ ns, for two cases (a) $\ell = 120$ and (b) $\ell = 30$.

case, the RT growth remained in a linear stage to the end of acceleration, which is confirmed by the absence of harmonics in Fig. 123.10(b).

By scanning the different single-mode simulations, the modulation amplitudes at the ablation surface as a function of laser-imprinting mode are shown in Figs. 123.11(a) and 123.11(b) at the start and end of acceleration, respectively. Both SSD-on (green squares) and SSD-off (red circles) cases are shown in Fig. 123.11. The simulation results show that SSD reduces the modulation amplitude by a factor of 3 to 4, depending on the mode range. Overall, the laser-imprinting spectra (at the end of acceleration) show two distinct peaks around $\ell = 30$ and $\ell = 120$ for the triple-picket, step-main-pulse, cryogenic-DT design. The laser-imprinting spectra for the triple-picket design are compared with previous continuous-pulse, 5-μm-CD-shell designs[45,46] in Fig. 123.12(a) at the start of the acceleration phase and Fig. 123.12(b) at the end of the

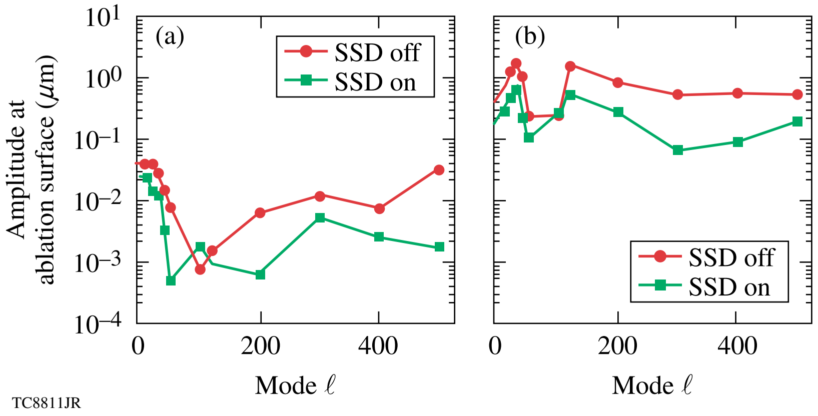

Figure 123.11
The laser-imprinting spectrum at (a) the start of acceleration and (b) the end of acceleration, for both SSD-off and SSD-on cases.

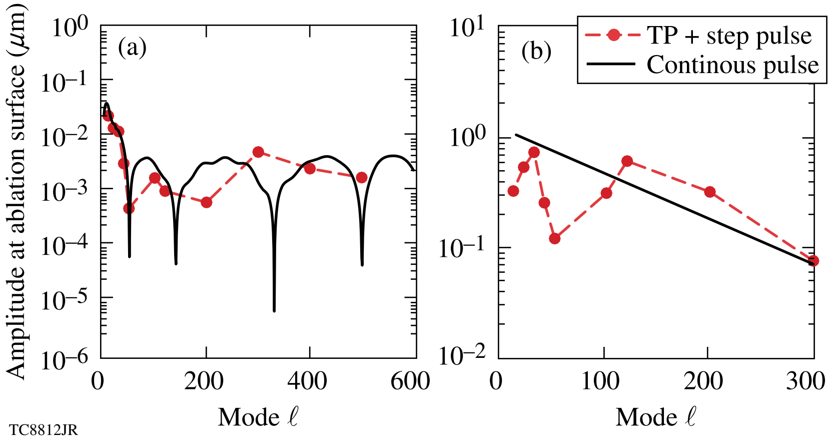

Figure 123.12
The laser-imprinting comparison between the triple-picket plus step-pulse (circles) and the continuous-pulse designs (solid lines) at (a) the start of acceleration and (b) the end of acceleration for the SSD-on case.

acceleration phase for the SSD-on case. The laser imprinting for the triple-picket design is comparable to the imprinting of the continuous-pulse and 5-μm-CD-shell designs, even though a 10-μm-thick CD shell was used in the triple-picket design (for the purpose of reducing potential fast-electron preheat[47]). This is accomplished with the strong adiabat shaping[46,48] caused by the three pickets.

The single-mode studies were performed up to a very high mode of ℓ = 500, where there was evidence that short-wavelength (high-mode) RT growth can be stabilized in high-intensity drives at $I \sim 10^{15}$ W/cm^2 in planar experiments.[11,12] At such high intensity, the corona temperature is about $T_e \approx$ 3 keV, resulting in a heat-carrying electron energy of around 15 to 20 keV. These electrons nonlocally affect the heat transport.[29,49] They can penetrate to provide an extra heating at the ablation surface, which may in turn cause the ablation velocity to increase, leading to the short-wavelength RT stabilization, as the growth rate[50] scales as $\gamma - 0.94\sqrt{kg/(1+kL_m)} - 1.5\,kV_a$, with wave number k, acceleration g, density scale length L_m, and ablation velocity V_a. Planar experiments with a wavelength of $\lambda = 20\ \mu$m have shown no RT growth at such high-intensity drive conditions.[11,12] For the cryogenic-DT, triple-picket designs, the laser intensity peaks at $I \sim 8 \times 10^{14}$ W/cm^2, which results in a corona temperature of ~2.7 keV. Since the mean free path of the heat-carrying electrons scales with $\sim T_e^2$, it is estimated that perturbations with $\lambda < 15$ to 16 μm should be stabilized, which corresponds to modes $\ell \geq 150$ to 200 (at the initial radius of $R = 350\ \mu$m at the start of acceleration). Therefore, for the multimode simulations the maximum mode was chosen to be ℓ_{max} = 200. The multimode simulations were performed using a 45° wedge. To satisfy the boundary conditions, every fourth mode was included in the simulations. The amplitudes of the skipped ($\Delta\ell = 4$) modes were added in quadrature to conserve the total σ_{rms} of laser imprinting. Sixteen grid points per wavelength were used for the maximum laser-imprinting mode. The grid can support the harmonic growth of lower laser-imprinting modes ($\ell < 100$). The result of a simulation with ℓ_{max} = 200 is shown in Fig. 123.13(a), where the density contours are plotted in the SSD-on case at the end of acceleration. It indicates two distinct features: (a) the dominant mode is around ℓ = 32; (b) the second laser-

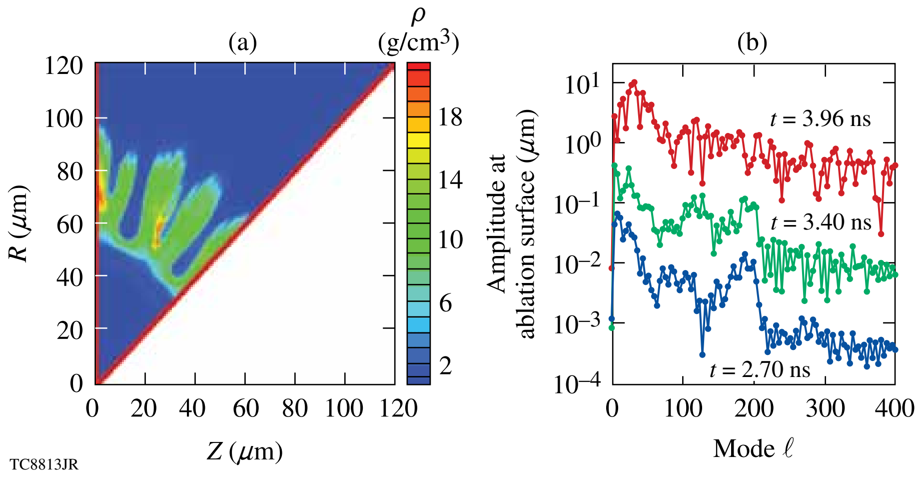

Figure 123.13
(a) The density contour plot for a multimode simulation (up to mode $\ell_{max} = 200$ with SSD on) at the end of acceleration; (b) the modal spectrum at different times for the same simulation.

imprinting peak is located around $\ell = 120$. Both features are consistent with the single-mode simulation results shown in Fig. 123.11(b). Figure 123.13(a) shows the "bubble" and "spike" growth, indicating the nonlinear growth and mode coupling.[9] The Fourier transform of the ablation surface [Fig. 123.13(b)] shows the history of RT-growth modal spectra at times of $t = 2.7$ ns, $t = 3.4$ ns, and $t = 3.96$ ns. At $t = 2.7$ ns, the lower (blue) curve in Fig. 123.13(b) indicates a sharp cutoff at $\ell = 200$, the same as the maximum laser-imprinting seeds included. The modal spectra grow almost linearly to $t = 3.4$ ns with distinct features peaking at $\ell = 32$ and $\ell = 120$ beginning to appear. At the end of acceleration, the two overall peaks around $\ell = 32$ and $\ell = 120$ appear in the upper curve ($t = 3.96$ ns), which is consistent with the single-mode predictions. The nonlinear growth for imprinting modes $\ell = 100$ to 200 has washed out the mode cutoff around $\ell = 200$. Mode coupling caused by high-mode nonlinear growth enhances the low-mode growth that leads to effective disruption of the neutron production from the hot spot.

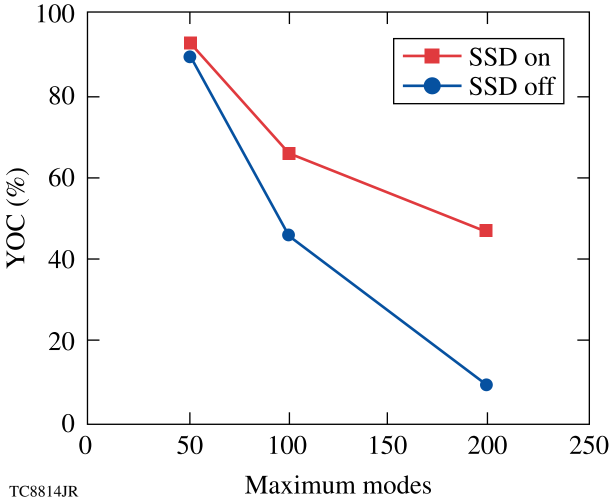

Figure 123.14
The YOC is plotted as a function of maximum modes included in multimode simulations, for the step main pulse in SSD-off and SSD-on cases.

By including the maximum modes up to $\ell_{max} = 50$, $\ell_{max} = 100$, and $\ell_{max} = 200$ separately in six multimode simulations, we obtained the laser-imprinting effects on the YOC. The results are shown in Fig. 123.14 for the step-main-pulse design in the SSD-on (red squares) and SSD-off (blue circles) cases. Figure 123.14 shows that simulations with multimodes up to $\ell_{max} = 50$ hardly reduce the yield, even though the first imprinting peak around $\ell = 30$ has been included. This again indicates the laser imprinting to the yield-reduction effect is through the enhanced low-mode growth that is "fed" by the high-mode nonlinear saturation. High modes $\ell > 150$ may be stabilized by nonlocal electron heating of the ablation surface. This effect was not included in the *DRACO* simulations; therefore, the $\ell_{max} = 200$ results may overestimate the laser-imprinting effects. The multimode simulation up to about $\ell_{max} = 150$ shows that the resultant YOC ratio of the SSD-on case to the SSD-off is ~2. This agrees well with experimental observations that will be discussed in ***DRACO* Simulations of Individual Cryogenic-DT Shots**, p. 122. Laser-imprinting effects reduced the YOC to ~50% in the SSD-on case and further to ~25% in the SSD-off case. Turning on the SSD improved the yield by a factor of ~2, which has been seen in both *DRACO* simulations and experiments.

Separate studies for each nonuniformity source (in the case of the step main pulse) have identified three dominant nonuniformities that affect the cryogenic-DT implosion performance: (a) a power imbalance ($\ell < 10$) of ~10% (pickets) and ~3% (main pulse) reduce the YOC to ~74%; (b) even with a high-quality ice layer ($\sigma_{\rm rms} = 1\ \mu$m), a target offset ($\ell = 1$) > 20 μm reduces the YOC to ~30%; and (c) the laser imprinting ($\ell = 20$ to 150) decreases the YOC to a level of ~25% (SSD off) and ~50% (SSD on). If these three major perturbation effects were taken as a product (assuming they behave independently in a different modal range), the yield would be about YOC $\simeq$ 5% (SSD off) and YOC $\simeq$ 10% (SSD on). This is in agreement (within a factor of ~2) with the measured YOC.

DRACO Simulations of Individual Cryogenic-DT Shots

A series of low-adiabat ($\alpha = 2.0$ to 2.5), cryogenic-DT target implosions have been performed using the triple-picket pulse designs [Figs. 123.1(a) and 123.1(b)] on OMEGA. Detailed compression dynamics and areal-density measurements up to $\langle \rho R \rangle \simeq 300$ mg/cm^2 have been described in Refs. 17 and 18. Integrated *DRACO* simulations for nine individual cryogenic-DT shots that resulted in a large, absolute areal density of $\langle \rho R \rangle > 180$ mg/cm^2 (>80% of their 1-D designs) have been performed, including the actual experimental laser and target conditions. Low-mode ($\ell \le 50$) *DRACO* simulations included the long-wavelength laser nonuniformities, target offset, and ice roughness (high-mode laser imprinting was not included). The low-mode simulation results (blue squares) shown in Fig. 123.15(a) compare the simulated YOC with the experimental values (red symbols) versus the target offset. Three phases of ice roughness have been examined for each shot in the *DRACO* simulations. The nine experimental shots are divided into three laser conditions: (1) triple-picket plus square main pulse with SSD on (red diamonds); (2) triple-picket plus square main pulse with SSD off (red triangles); and (3) triple-picket plus step main pulse with SSD off (red circles). Figure 123.15(a) shows that for those shots with an offset larger than ~25 μm, the low-mode *DRACO* predictions can explain the experimental YOC since the target offset together with ice roughness ($\sigma_{\rm rms} = 1$ to 2 μm) is the dominant perturbation source. The low-mode *DRACO* neutron-yield predictions at small offsets are generally higher, however, than the experimental observations, in which the laser imprinting dominates.

A full simulation including both the low-mode perturbations discussed above and the high-mode laser imprinting has been performed up to $\ell_{\max} = 200$ for a shot with a 3-μm offset. The resultant YOC is shown by the orange square in Fig. 123.15(b). Compared to the low-mode modeling ($\ell < 50$), the high-mode simulation reduces the YOC by a factor of ~4 for this shot (SSD off). This is in agreement with the results presented in **Laser Imprinting**, p. 118. For other shots, the laser-imprinting effects were taken into account by "scaling" low-mode simulation results by either a factor of ~2 reduction in the case of SSD on or a factor of ~4 reduction in the case of SSD off. The resultant high-mode predictions shown in Fig. 123.15(b) are compared with experiments. The high-mode *DRACO* predictions with laser-imprinting effects now agree with experimental YOC within a factor of 2 or better for all shots. From Fig. 123.15(b), two distinct features can be seen: (a) the square-main-pulse shots with SSD on give an experimental YOC of ~9% (red diamonds), which is twice as high as that of the same pulse shape with SSD off (red triangles); (b) the three step-main-pulse shots (red circles) with SSD off

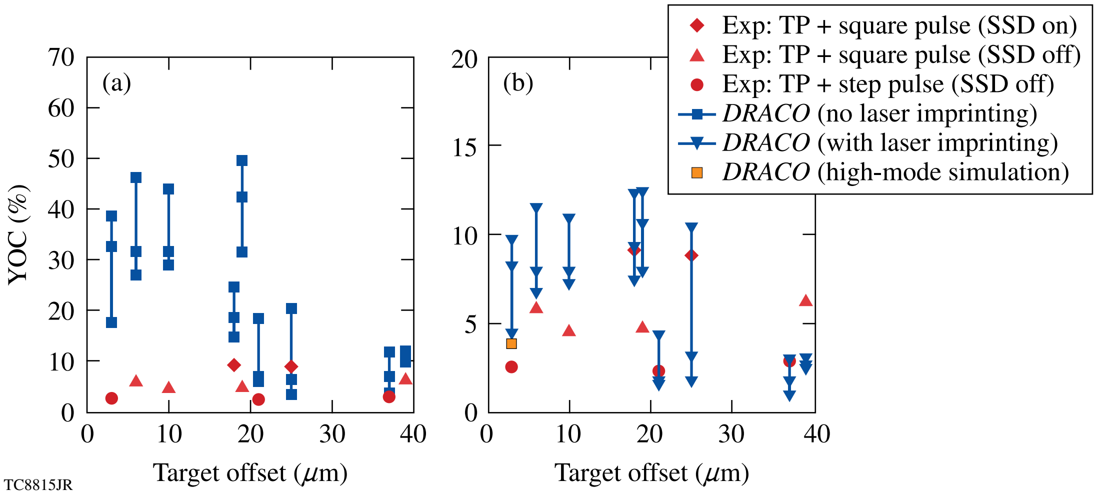

Figure 123.15
The YOC comparison between experiments and *DRACO* simulations for individual shots: (a) without laser imprinting and (b) with laser imprinting considered.

have a YOC level of 2% to 3%, which is a factor of 2 below the square main pulse (red triangles) with SSD off. All of these behaviors are well reproduced by the *DRACO* simulations (see also Figs. 123.6 and 123.14).

The simulated ion temperatures for these individual shots are compared with experimental measurements in Fig. 123.16. In experiments, the neutron-averaged ion temperature $\langle T_\mathrm{i}\rangle$ is inferred by neutron time-of-flight spectroscopy.[22] The measurement uncertainty is about ±0.5 keV, shown in Fig. 123.16. The simulated $\langle T_\mathrm{i}\rangle$ for each shot has three entries based on the phases examined. To take into account laser-imprinting effects, the high-mode scaling of $\langle T_\mathrm{i}\rangle$ was done by either 10% or 15% reduction to the low-mode simulated $\langle T_\mathrm{i}\rangle$, respectively, to the shots with SSD on and SSD off, as has been seen in the direct high-mode simulations. Figure 123.16 indicates that the *DRACO*-simulated $\langle T_\mathrm{i}\rangle$ agrees with measurements within the experimental error bars. The TOC is defined as the ratio of experimental or *DRACO*-simulated $\langle T_\mathrm{i}\rangle$ to its 1-D–designed value, e.g., TOC = $\langle T_\mathrm{i}\rangle_{\text{exp or 2-D}} \big/ \langle T_\mathrm{i}\rangle_{\text{1-D}}$. The YOC versus TOC for all the shots is shown in Fig. 123.17. The experimental points are represented by red circles and the *DRACO* simulations by blue squares. The *DRACO* simulations tracked the experimental trend very well. The experimental error bar and simulation range of TOC are shown. A fitting line, YOC $\simeq 0.25 \times (\mathrm{TOC})^4$, just passes through both experimental and simulated points for the SSD-off shots. For the cryogenic-DT implosion conditions, the neutron yield N is proportional to the hot-spot volume (V), density (ρ), ion temperature (T_i), and the burn time (t_b) as

$$N \propto V \times t_\mathrm{b} \times \rho^2 \times T_\mathrm{i}^4. \qquad (2)$$

If Eq. (2) is divided by the 1-D clean values on each side, it gives

$$\mathrm{YOC} = \left[\frac{\rho\sqrt{Vt_b}}{\left(\rho\sqrt{Vt_b}\right)_{\text{1-D}}}\right]^2 \times (\mathrm{TOC})^4. \qquad (3)$$

The prefactor "0.25" of the solid green fitting line in Fig. 123.17 means that the product of hot-spot density and the square root of its volume and burn time reduced to ~50% of its 1-D value. This fitting characterizes the hot-spot distortion. The two shots with SSD on are above the fitting line. To have a fitting line with the same format passing through these two points, the prefactor is roughly about 0.49, meaning less hot-spot distortion (i.e., the product of hot-spot density and the square root of its volume and burn time has been reduced to ~70% of its 1-D value when SSD is turned on). The dashed red fitting line for the SSD-on case plotted in Fig. 123.17 confirms the importance of SSD for these implosions.

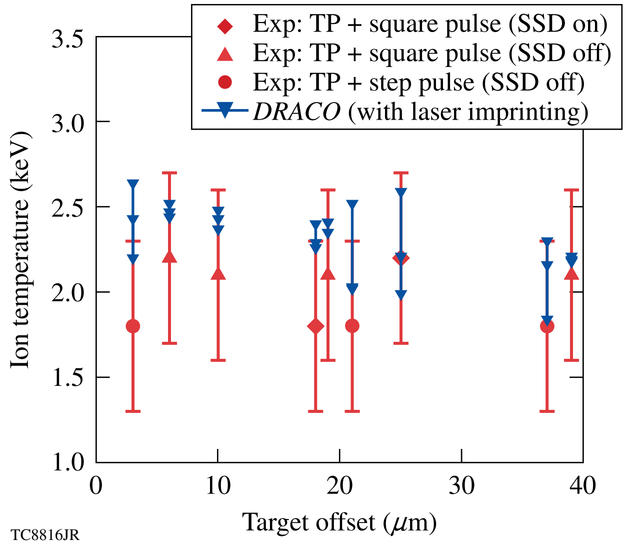

Figure 123.16
The neutron-averaged ion temperature comparison between experiments and *DRACO* simulations (with laser imprinting) for individual shots.

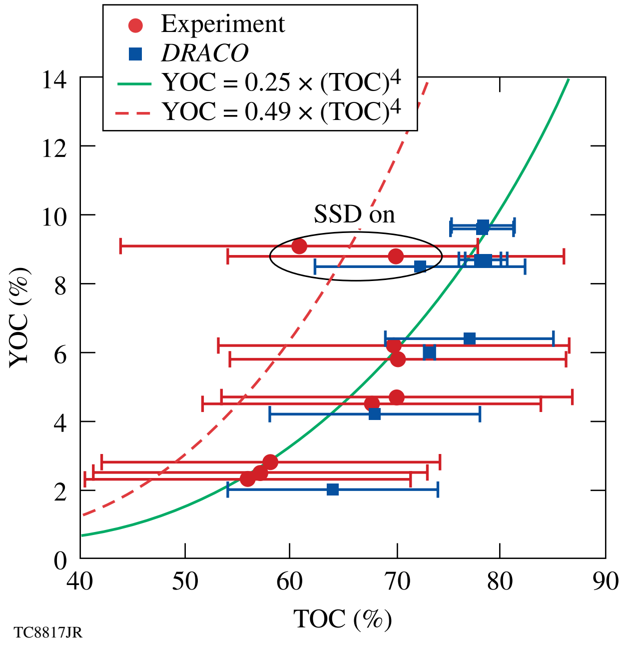

Figure 123.17
The relationship between YOC and TOC indicates the distortion of the hot-spot volume and density.

To have an insight into the hot-spot distortion caused by different perturbations, we calculated the clean volume fraction (CVF) and the volume-weighted surface area at the peak neutron-production time for different perturbed cases. The CVF is defined as the ratio of perturbed volume within the T_i = 3-keV contour to the uniform case, i.e., $\mathrm{CVF} = V\left(T_\mathrm{i} > 3\,\mathrm{keV}\right) \big/ V_{1\text{-D}}\left(T_\mathrm{i} > 3\,\mathrm{keV}\right)$. The surface area ($A$) along the T_i = 3-keV contour can also be calculated from the simulations. Since the heat conduction loss is proportional to the surface area, we define the volume-weighted surface-area increase factor (SAIF) to be $\mathrm{SAIF} = (A/V)\big/(A/V)_{1\text{-D}}$. In Fig. 123.18, we plot the YOC as a function of CVF and SAIF for (a) different target offsets of 40 μm, 20 μm, 10 μm, and 5 μm, and (b) the laser-imprinting effect. Figure 123.18(a) shows that as the target offset increases, the CVF decreases and the volume-weighted surface area increases, leading to a smaller effective volume for neutron production and more heat loss. Therefore, when the target offset increases, the YOC becomes smaller and smaller, as does the neutron burn width. A similar analysis was also carried out for the laser-imprinting effect. The results, plotted in Fig. 123.18(b), show the different maximum modes (ℓ_max = 50, 100, and 200) included in the SSD-on simulations (same as Fig. 123.14). When more modes were included, the clean volume fraction decreased and the surface area increased, resulting in a decrease in YOC. We noticed that the target offset did not change the peak neutron-production time, while the laser imprinting caused peak neutron production earlier than in the uniform case. This was caused by the laser imprinting inducing "spikes" that pinched into the hot spot to increase the hot-spot pressure so that the shell tended to stagnate earlier. These analyses indicate that the major perturbations of both the target offset and laser imprinting cause a reduction in hot-spot volume and an increase in hot-spot surface area (leading to quick hot-spot cooling), which ultimately lead to neutron-yield reduction.

The areal density inferred from 2-D simulations is discussed briefly here; detailed discussions were presented in Ref. 18. Using the 2-D simulations, the down-scattered neutron spectrum from which the areal density $\langle \rho R \rangle$ is inferred was calculated. An example is shown in Fig. 123.19, where the blue diamonds indicate the angle-averaged $\langle \rho R \rangle$ expected from 2-D simulations, which compare to the 1-D–designed value represented by the dashed red line. This is for the square-main-pulse case with the offset-only perturbation. The $\langle \rho R \rangle$ range

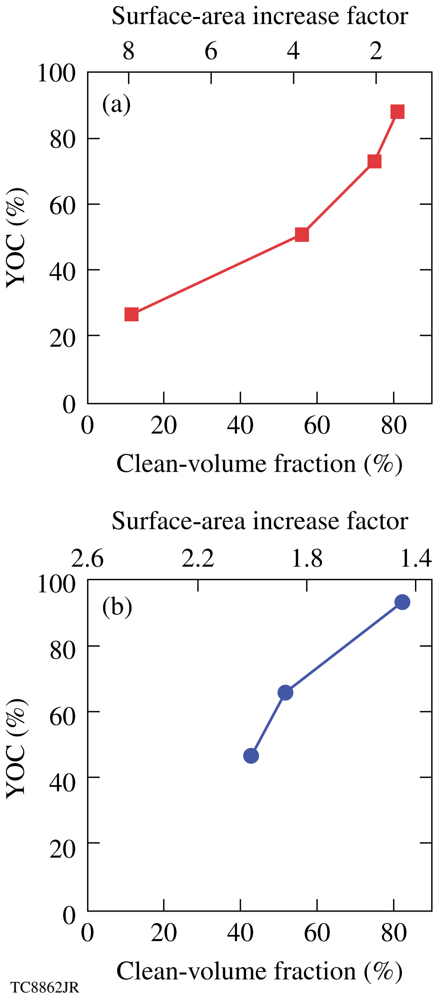

Figure 123.18
YOC as a function of the clean-volume fraction and the hot-spot surface-area-increase factor for (a) the target-offset effect and (b) the laser-imprinting effect (with step-pulse design).

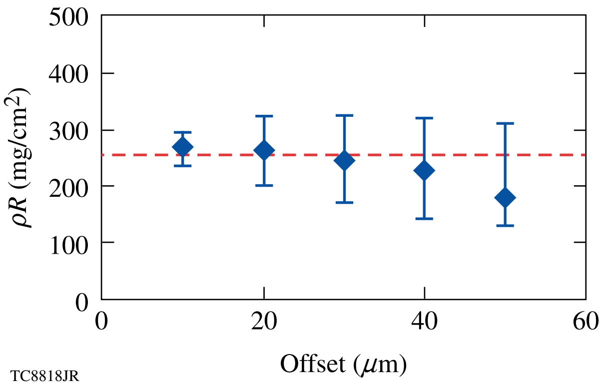

Figure 123.19
The areal density ($\langle \rho R \rangle$) inferred from the down-scattered neutron spectrum is plotted against the target offset. The dashed red line represents the corresponding 1-D value of $\langle \rho R \rangle$.

(error bar) is due to the different viewing angles around the target. Figure 123.19 indicates that the angle-averaged $\langle \rho R \rangle$ agrees with its 1-D–designed value if the offset is less than 20 μm. The angle-dependent range of $\langle \rho R \rangle$ is within the MRS measurement uncertainty of ±20%. Examinations of other perturbation sources show that the $\langle \rho R \rangle$ variation caused by perturbations is within the MRS measurement uncertainty.

Conclusions

In summary, the neutron-yield performance caused by a variety of nonuniformity sources for the cryogenic-DT implosions on OMEGA has been systematically investigated. The experimental trends are well-reproduced by 2-D *DRACO* hydrodynamic simulations: the simulated YOC agrees with experiments within a factor of 2 or better and the simulated ion temperatures $\langle T_\mathrm{i} \rangle$ fall within the experimental uncertainty of measurements. The relationship between YOC and TOC provides an indication of how much the hot-spot volume, density, and burn time are reduced. Based on the simulations, two dominant nonuniformity sources have been identified: the target offset and laser imprinting, which mainly account for the yield reduction in the cryogenic-DT shots. Another important issue is the laser power imbalance during the pickets, which has now been improved to 3% to 4% from the previous ~10%. The simulations suggest that to increase the YOC to an ignition-scaled level of ~15% to 20% for the step-main-pulse design (maintaining high-compression $\langle \rho R \rangle$ = 200 to 300 mg/cm^2), the target offset must be ≤10 μm and SSD must be used.

ACKNOWLEDGMENT

This work was supported by the U.S. Department of Energy (DOE) Office of Inertial Confinement Fusion under Cooperative Agreement No. DE-FC52-08NA28302, the University of Rochester, and the New York State Energy Research and Development Authority.

REFERENCES

1. S. Atzeni and J. Meyer-ter-Vehn, *The Physics of Inertial Fusion: Beam Plasma Interaction, Hydrodynamics, Hot Dense Matter*, International Series of Monographs on Physics (Clarendon Press, Oxford, 2004); J. D. Lindl, *Inertial Confinement Fusion: The Quest for Ignition and Energy Gain Using Indirect Drive* (Springer-Verlag, New York, 1998).
2. J. Nuckolls *et al.*, Nature **239**, 139 (1972).
3. R. L. McCrory, D. D. Meyerhofer, R. Betti, R. S. Craxton, J. A. Delettrez, D. H. Edgell, V. Yu Glebov, V. N. Goncharov, D. R. Harding, D. W. Jacobs-Perkins, J. P. Knauer, F. J. Marshall, P. W. McKenty, P. B. Radha, S. P. Regan, T. C. Sangster, W. Seka, R. W. Short, S. Skupsky, V. A. Smalyuk, J. M. Soures, C. Stoeckl, B. Yaakobi, D. Shvarts, J. A. Frenje, C. K. Li, R. D. Petrasso, and F. H. Séguin, Phys. Plasmas **15**, 055503 (2008).
4. J. D. Lindl, Phys. Plasmas **2**, 3933 (1995).
5. S. E. Bodner, Phys. Rev. Lett. **33**, 761 (1974); H. Takabe *et al.*, Phys. Fluids **28**, 3676 (1985); H. J. Kull and S. I. Anisimov, Phys. Fluids **29**, 2067 (1986); A. B. Bud'ko and M. A. Liberman, Phys. Fluids B **4**, 3499 (1992); V. V. Bychkov, S. M. Goldberg, and M. A. Liberman, Phys. Plasmas **1**, 2976 (1994); J. Sanz, Phys. Rev. Lett. **73**, 2700 (1994); J. G. Wouchuk and A. R. Piriz, Phys. Plasmas **2**, 493 (1995).
6. R. Betti, V. N. Goncharov, R. L. McCrory, P. Sorotokin, and C. P. Verdon, Phys. Plasmas **3**, 2122 (1996); V. N. Goncharov, P. McKenty, S. Skupsky, R. Betti, R. L. McCrory, and C. Cherfils-Clérouin, Phys. Plasmas **7**, 5118 (2000).
7. P. Y. Chang, R. Betti, B. K. Spears, K. S. Anderson, J. Edwards, M. Fatenejad, J. D. Lindl, R. L. McCrory, R. Nora, and D. Shvarts, Phys. Rev. Lett. **104**, 135002 (2010).
8. J. Paisner *et al.*, Laser Focus World **30**, 75 (1994); E. M. Campbell and W. J. Hogan, Plasma Phys. Control. Fusion **41**, B39 (1999).
9. S. W. Haan, Phys. Rev. A **39**, 5812 (1989); M. M. Marinak *et al.*, Phys. Rev. Lett. **80**, 4426 (1998).
10. B. A. Remington *et al.*, Phys. Rev. Lett. **73**, 545 (1994); K. S. Budil *et al.*, Phys. Rev. Lett. **76**, 4536 (1996); C. J. Pawley *et al.*, Phys. Plasmas **6**, 565 (1999); J. P. Knauer, K. Anderson, R. Betti, T. J. B. Collins, V. N. Goncharov, P. W. McKenty, D. D. Meyerhofer, P. B. Radha, S. P. Regan, T. C. Sangster, V. A. Smalyuk, J. A. Frenje, C. K. Li, R. D. Petrasso, and F. H. Séguin, Phys. Plasmas **12**, 056306 (2005); V. A. Smalyuk, O. Sadot, J. A. Delettrez, D. D. Meyerhofer, S. P. Regan, and T. C. Sangster, Phys. Rev. Lett. **95**, 215001 (2005); H. Azechi *et al.*, Phys. Rev. Lett. **98**, 045002 (2007).
11. V. A. Smalyuk, S. X. Hu, V. N. Goncharov, D. D. Meyerhofer, T. C. Sangster, D. Shvarts, C. Stoeckl, B. Yaakobi, J. A. Frenje, and R. D. Petrasso, Phys. Rev. Lett. **101**, 025002 (2008).
12. V. A. Smalyuk, S. X. Hu, V. N. Goncharov, D. D. Meyerhofer, T. C. Sangster, C. Stoeckl, and B. Yaakobi, Phys. Plasmas **15**, 082703 (2008).
13. V. A. Smalyuk, S. X. Hu, J. D. Hager, J. A. Delettrez, D. D. Meyerhofer, T. C. Sangster, and D. Shvarts, Phys. Rev. Lett. **103**, 105001 (2009).
14. V. A. Smalyuk, S. X. Hu, J. D. Hager, J. A. Delettrez, D. D. Meyerhofer, T. C. Sangster, and D. Shvarts, Phys. Plasmas **16**, 112701 (2009).
15. T. R. Boehly, D. L. Brown, R. S. Craxton, R. L. Keck, J. P. Knauer, J. H. Kelly, T. J. Kessler, S. A. Kumpan, S. J. Loucks, S. A. Letzring, F. J. Marshall, R. L. McCrory, S. F. B. Morse, W. Seka, J. M. Soures, and C. P. Verdon, Opt. Commun. **133**, 495 (1997).
16. S. X. Hu, P. B. Radha, J. A. Marozas, R. Betti, T. J. B. Collins, R. S. Craxton, J. A. Delettrez, D. H. Edgell, R. Epstein, V. N. Goncharov, I. V. Igumenshchev, F. J. Marshall, R. L. McCrory, D. D. Meyerhofer, S. P. Regan, T. C. Sangster, S. Skupsky, V. A. Smalyuk, Y. Elbaz, and D. Shvarts, Phys. Plasmas **16**, 112706 (2009).
17. V. N. Goncharov, T. C. Sangster, T. R. Boehly, S. X. Hu, I. V. Igumenshchev, F. J. Marshall, R. L. McCrory, D. D. Meyerhofer, P. B. Radha, W. Seka, S. Skupsky, C. Stoeckl, D. T. Casey, J. A. Frenje, and R. D. Petrasso, Phys. Rev. Lett. **104**, 165001 (2010).

18. T. C. Sangster, V. N. Goncharov, R. Betti, T. R. Boehly, D. T. Casey, T. J. B. Collins, R. S. Craxton, J. A. Delettrez, D. H. Edgell, R. Epstein, K. A. Fletcher, J. A. Frenje, V. Yu. Glebov, D. R. Harding, S. X. Hu, I. V. Igumenshchev, J. P. Knauer, S. J. Loucks, C. K. Li, J. A. Marozas, F. J. Marshall, R. L. McCrory, P. W. McKenty, D. D. Meyerhofer, P. M. Nilson, S. P. Padalino, R. D. Petrasso, P. B. Radha, S. P. Regan, F. H. Seguin, W. Seka, R. W. Short, D. Shvarts, S. Skupsky, V. A. Smalyuk, J. M. Soures, C. Stoeckl, W. Theobald, and B. Yaakobi, Phys. Plasmas **17**, 056312 (2010).

19. P. B. Radha, T. J. B. Collins, J. A. Delettrez, Y. Elbaz, R. Epstein, V. Yu. Glebov, V. N. Goncharov, R. L. Keck, J. P. Knauer, J. A. Marozas, F. J. Marshall, R. L. McCrory, P. W. McKenty, D. D. Meyerhofer, S. P. Regan, T. C. Sangster, W. Seka, D. Shvarts, S. Skupsky, Y. Srebro, and C. Stoeckl, Phys. Plasmas **12**, 056307 (2005); D. Keller, T. J. B. Collins, J. A. Delettrez, P. W. McKenty, P. B. Radha, B. Whitney, and G. A. Moses, Bull. Am. Phys. Soc. **44**, 37 (1999).

20. T. R. Boehly, D. H. Munro, P. M. Celliers, R. E. Olson, D. G. Hicks, V. N. Goncharov, G. W. Collins, H. F. Robey, S. X. Hu, J. A. Marozas, T. C. Sangster, O. L. Landen, and D. D. Meyerhofer, Phys. Plasmas **16**, 056302 (2009).

21. J. A. Frenje, K. M. Green, D. G. Hicks, C. K. Li, F. H. Séguin, R. D. Petrasso, T. C. Sangster, T. W. Phillips, V. Yu. Glebov, D. D. Meyerhofer, S. Roberts, J. M. Soures, C. Stoeckl, K. Fletcher, S. Padalino, and R. J. Leeper, Rev. Sci. Instrum. **72**, 854 (2001).

22. T. J. Murphy, R. E. Chrien, and K. A. Klare, Rev. Sci. Instrum. **68**, 610 (1997).

23. J. A. Marozas, F. J. Marshall, R. S. Craxton, I. V. Igumenshchev, S. Skupsky, M. J. Bonino, T. J. B. Collins, R. Epstein, V. Yu. Glebov, D. Jacobs-Perkins, J. P. Knauer, R. L. McCrory, P. W. McKenty, D. D. Meyerhofer, S. G. Noyes, P. B. Radha, T. C. Sangster, W. Seka, and V. A. Smalyuk, Phys. Plasmas **13**, 056311 (2006).

24. B. I. Bennett *et al.*, Los Alamos National Laboratory, Los Alamos, NM, Report LA-7130 (1978).

25. W. F. Huebner *et al.*, Los Alamos National Laboratory, Los Alamos, NM, Report LA-6760-M (1977).

26. R. C. Malone, R. L. McCrory, and R. L. Morse, Phys. Rev. Lett. **34**, 721 (1975).

27. S. P. Regan, R. Epstein, V. N. Goncharov, I. V. Igumenshchev, D. Li, P. B. Radha, H. Sawada, W. Seka, T. R. Boehly, J. A. Delettrez, O. V. Gotchev, J. P. Knauer, J. A. Marozas, F. J. Marshall, R. L. McCrory, P. W. McKenty, D. D. Meyerhofer, T. C. Sangster, D. Shvarts, S. Skupsky, V. A. Smalyuk, B. Yaakobi, and R. C. Mancini, Phys. Plasmas **14**, 056305 (2007).

28. T. R. Boehly, E. Vianello, J. E. Miller, R. S. Craxton, T. J. B. Collins, V. N. Goncharov, I. V. Igumenshchev, D. D. Meyerhofer, D. G. Hicks, P. M. Celliers, and G. W. Collins, Phys. Plasmas **13**, 056303 (2006).

29. S. X. Hu, V. Smalyuk, V. N. Goncharov, S. Skupsky, T. C. Sangster, D. D. Meyerhofer, and D. Shvarts, Phys. Rev. Lett. **101**, 055002 (2008).

30. V. N. Goncharov, O. V. Gotchev, E. Vianello, T. R. Boehly, J. P. Knauer, P. W. McKenty, P. B. Radha, S. P. Regan, T. C. Sangster, S. Skupsky, V. A. Smalyuk, R. Betti, R. L. McCrory, D. D. Meyerhofer, and C. Cherfils-Clérouin, Phys. Plasmas **13**, 012702 (2006).

31. S. X. Hu, V. A. Smalyuk, V. N. Goncharov, J. P. Knauer, P. B. Radha, I. V. Igumenshchev, J. A. Marozas, C. Stoeckl, B. Yaakobi, D. Shvarts, T. C. Sangster, P. W. McKenty, D. D. Meyerhofer, S. Skupsky, and R. L. McCrory, Phys. Rev. Lett. **100**, 185003 (2008).

32. I. V. Igumenshchev, F. J. Marshall, J. A. Marozas, V. A. Smalyuk, R. Epstein, V. N. Goncharov, T. J. B. Collins, T. C. Sangster, and S. Skupsky, Phys. Plasmas **16**, 082701 (2009).

33. Y. Lin, T. J. Kessler, and G. N. Lawrence, Opt. Lett. **20**, 764 (1995).

34. T. R. Boehly, V. A. Smalyuk, D. D. Meyerhofer, J. P. Knauer, D. K. Bradley, R. S. Craxton, M. J. Guardalben, S. Skupsky, and T. J. Kessler, J. Appl. Phys. **85**, 3444 (1999).

35. J. A. Frenje, C. K. Li, F. H. Séguin, D. T. Casey, R. D. Petrasso, T. C. Sangster, R. Betti, V. Yu. Glebov, and D. D. Meyerhofer, Phys. Plasmas **16**, 042704 (2009).

36. D. R. Harding, D. D. Meyerhofer, S. J. Loucks, L. D. Lund, R. Janezic, L. M. Elasky, T. H. Hinterman, D. H. Edgell, W. Seka, M. D. Wittman, R. Q. Gram, D. Jacobs-Perkins, R. Early, T. Duffy, and M. J. Bonino, Phys. Plasmas **13**, 056316 (2006).

37. T. C. Sangster, R. Betti, R. S. Craxton, J. A. Delettrez, D. H. Edgell, L. M. Elasky, V. Yu. Glebov, V. N. Goncharov, D. R. Harding, D. Jacobs-Perkins, R. Janezic, R. L. Keck, J. P. Knauer, S. J. Loucks, L. D. Lund, F. J. Marshall, R. L. McCrory, P. W. McKenty, D. D. Meyerhofer, P. B. Radha, S. P. Regan, W. Seka, W. T. Shmayda, S. Skupsky, V. A. Smalyuk, J. M. Soures, C. Stoeckl, B. Yaakobi, J. A. Frenje, C. K. Li, R. D. Petrasso, F. H. Séguin, J. D. Moody, J. A. Atherton, B. D. MacGowan, J. D. Kilkenny, T. P. Bernat, and D. S. Montgomery, Phys. Plasmas **14**, 058101 (2007).

38. J. A. Koch *et al.*, Fusion Technol. **38**, 123 (2000).

39. D. H. Edgell, W. Seka, R. S. Craxton, L. M. Elasky, D. R. Harding, R. L. Keck, and M. D. Wittman, Fusion Sci. Technol. **49**, 616 (2006).

40. V. N. Goncharov, S. Skupsky, T. R. Boehly, J. P. Knauer, P. McKenty, V. A. Smalyuk, R. P. J. Town, O. V. Gotchev, R. Betti, and D. D. Meyerhofer, Phys. Plasmas **7**, 2062 (2000).

41. R. Epstein, J. Appl. Phys. **82**, 2123 (1997).

42. S. P. Regan, J. A. Marozas, J. H. Kelly, T. R. Boehly, W. R. Donaldson, P. A. Jaanimagi, R. L. Keck, T. J. Kessler, D. D. Meyerhofer, W. Seka, S. Skupsky, and V. A. Smalyuk, J. Opt. Soc. Am. B **17**, 1483 (2000).

43. S. Skupsky, R. W. Short, T. Kessler, R. S. Craxton, S. Letzring, and J. M. Soures, J. Appl. Phys. **66**, 3456 (1989); J. E. Rothenberg, J. Opt. Soc. Am. B **14**, 1664 (1997).

44. J. A. Marozas, J. D. Zuegel, and T. J. B. Collins, Bull. Am. Phys. Soc. **54**, 306 (2009).

45. *LLE Review Quarterly Report* **82**, 49, Laboratory for Laser Energetics, University of Rochester, Rochester, NY, LLE Document No. DOE/SF/19460-344 (2000).

46. V. N. Goncharov, J. P. Knauer, P. W. McKenty, P. B. Radha, T. C. Sangster, S. Skupsky, R. Betti, R. L. McCrory, and D. D. Meyerhofer, Phys. Plasmas **10**, 1906 (2003).

47. V. A. Smalyuk, D. Shvarts, R. Betti, J. A. Delettrez, D. H. Edgell, V. Yu. Glebov, V. N. Goncharov, R. L. McCrory, D. D. Meyerhofer, P. B. Radha, S. P. Regan, T. C. Sangster, W. Seka, S. Skupsky, C. Stoeckl, B. Yaakobi, J. A. Frenje, C. K. Li, R. D. Petrasso, and F. H. Séguin, Phys. Rev. Lett. **100**, 185005 (2008).
48. K. Anderson and R. Betti, Phys. Plasmas **10**, 4448 (2003).
49. G. Schurtz *et al.*, Phys. Rev. Lett. **98**, 095002 (2007).
50. R. Betti, V. N. Goncharov, R. L. McCrory, and C. P. Verdon, Phys. Plasmas **5**, 1446 (1998).

X-Ray Radiography of Cryogenic Implosions on OMEGA

Introduction

Radiographs of cryogenic implosions on OMEGA[1] have been obtained using short-pulse, aluminum K-shell emission-line backlighters driven by the OMEGA EP short-pulse laser.[2] These experiments[3] have been designed to implode cryogenic D_2/DT shells and to achieve conditions that scale up to the thermonuclear ignition conditions[4] that can be attained with the much greater energy available on the NIF (National Ignition Facility).[5] X-ray radiography is being developed to verify the integrity of the imploding cryogenic shells and to corroborate the compression performance measured from charged-particle spectra.[3] The backlighter is chosen so that the emission-line energies occur where the energy-dependent optical thicknesses of the imploded cores will provide a measurable range of radiographic transmission near the time of peak compression. Backlighter simulations show that it can overcome the imploded core self-emission. The OMEGA EP short-pulse capability provides a backlight exposure time that is short enough to discern the overall shell integrity and convergence, as well as shell structure resulting from the low-order hydrodynamic effects of drive nonuniformity, target positioning offset, and ice-layer nonuniformity. Numerical simulations of the first measured cryogenic implosion radiographs[6] are used to assess the implosion performance in advance of peak compression. The radiographic simulation takes into account the spatial and temporal resolution, the camera spectral response, and the backlighter spectrum. Radial mass distributions are obtained from the radiographs using Abel inversion and the known temperature and density dependence of the free-free (FF) opacity of the hydrogen shell. This extends similar analyses of warm-shell radiographs, based on the simpler temperature and density dependence of the CH bound-free (BF) opacity, which has been applied to warm polar-drive implosions.[7] Radiography based on Compton scattering of hard backlight x rays approaching 100-keV energy[8,9] is being investigated as an alternative approach.

The measurements presented here are preliminary but are consistent with simulated implosion performance and radiography in advance of peak compression. They are valuable in planning future measurements that will be extended to the final phases of the implosion.

This article describes the experimental configurations. The atomic physics of both FF and Compton radiography, which is the basis for analyzing radiographs and for anticipating the relative advantages of each method, is described. The simulations demonstrate the feasibility of soft x-ray FF radiography and hard x-ray Compton radiography. Simulations of backlighters and radiographs are based on quantitative atomic physics and radiative transport. Finally, the available FF radiographs are analyzed, and conclusions are presented.

Experimental Configurations

The initial experimental configuration with FF radiography of cryogenic implosions includes a 10-μm-thick, 1-mm-sq Al-foil area backlighter target attached to the wire support for a silk-mounted target (Fig. 123.20). The backlighter foil is irradiated with a single 1-kJ, 10-ps OMEGA EP beam. Time-resolved backlit images are recorded through a pinhole array with an x-ray framing camera that provides 30-ps time gating.[10] The energy band, including the Al K-shell lines, is isolated using transmission filters and Ir-coated mirrors that reject hard backlighter x rays above 2 keV. One measured image is shown. The shadow of the imploding shell is visible against the emission from the irradiated spot on the backlighter foil. Further development of this diagnostic will include narrowing the camera bandwidth, possibly employing a monochromatic imaging device to further reduce the background caused by self-emission from the imploded target.

The experimental configuration for Compton radiography, shown in Fig. 123.21, is very similar to the configuration for FF backlighting.[11] The backlighter target is a 10-μm Au microwire embedded in a 300-μm-sq CH foil substrate. The 1-kJ, 10-ps OMEGA EP beam is focused onto a small 100-μm-diam spot to create a pulse of suprathermal electrons that drive a burst of K_α and bremsstrahlung emission from the microwire in a broad spectral range centered near 90 keV. By aligning the wire along the line of sight to the target, the end-on view

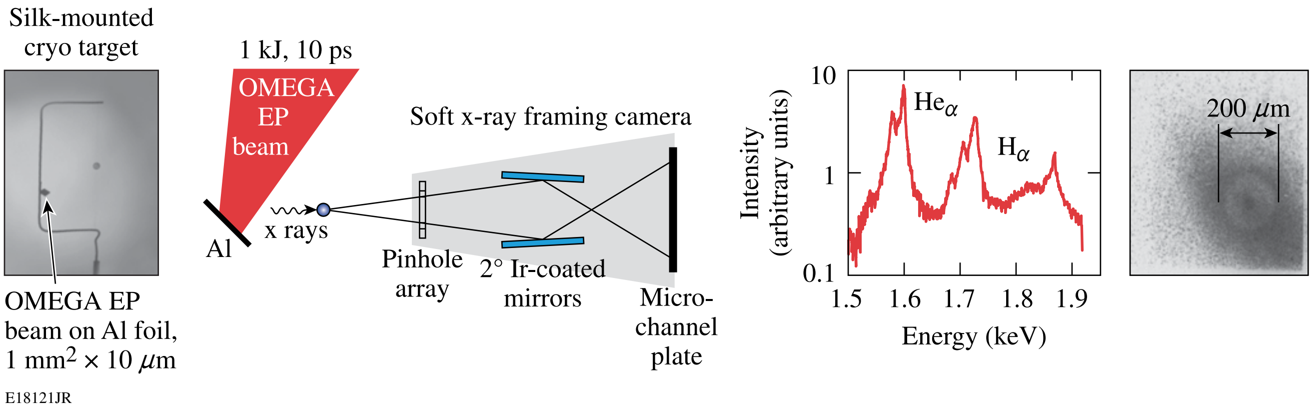

Figure 123.20
The configuration of our initial experiments with free-free (FF) radiography of cryogenic implosions includes an Al-foil area backlighter target attached to the wire support of a silk-mounted target. The backlight from the foil is driven with a single 1-kJ, 10-ps OMEGA EP beam. Time-resolved backlit images are recorded through a pinhole array with an x-ray framing camera. One measured image is shown. The shadow of the imploding shell is visible against the emission from the irradiated spot on the backlighter foil. The imaged photon energy band, including the Al K-shell lines, is isolated using transmission filters and Ir-coated mirrors.

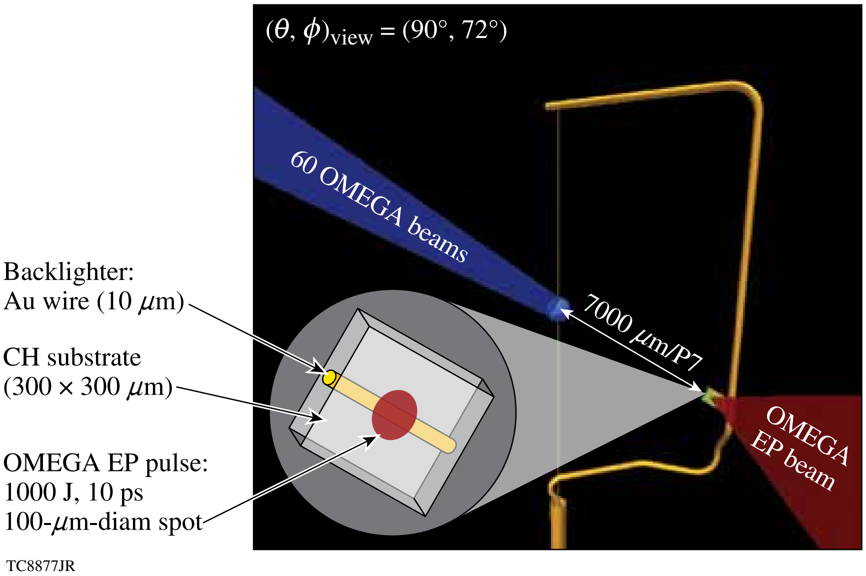

Figure 123.21
The configuration under development for Compton radiography is very similar to the configuration for FF backlighting. The backlighter target is a 10-μm Au microwire embedded in a CH-foil substrate. The 1-kJ, 10-ps OMEGA EP beam is focused to a small 100-μm-diam spot to create a burst of K$_\alpha$ and bremsstrahlung emission from the microwire in a broad spectral range centered near 90 keV. The end-on view of this wire appears to the image plate as a point backlighter.

of this wire appears from the direction of the image plate as a point backlighter. Preliminary radiographs of warm CH target implosions have been obtained with this configuration on OMEGA by Tommasini.[9] This method is currently being applied to cryogenic implosions.

Atomic Physics Basis for Radiography

A radiograph is formed by the attenuation of backlighter emission by an object, creating a shadow of the object in an imaging device. This process is illustrated in Fig. 123.22 for a spherical object creating a circularly symmetric shadow. The image intensity $I(x)$ is a central lineout of the measured intensity distribution along the x axis of the image plane coordinates x,y with y fixed accordingly. All the backlighter rays, propagating in parallel, create an orthographic projection of the object on the image plane, as if the backlighter were infinitely far away. The intensity $I(x)$ is the attenuated backlighter intensity I_{BL}. The attenuation is given by $I(x) = I_{\mathrm{BL}} \exp[-\tau(x)]$, where $\tau(x)$, the optical thickness of the object along a particular line of sight from the backlighter to the point x on the image plane, is the path integral $\tau(x) = \int \kappa(s)\,\mathrm{d}s$ of the opacity of the object $\kappa(s)$, expressed as a function of position along the path, indicated by the path-length parameter s (Ref. 12). If the opacity of the object is a known function of its conditions, an optical thickness measurement will provide a diagnostic of conditions along the line of sight. Writing $\kappa[r(s)]$ in Fig. 123.22 shows that the points on the path s correspond to points r in a spherical opacity distribution and that the two are related in a well-defined way. This relationship forms the basis for inferring $\kappa(r)$ from $\tau(x)$ by Abel inversion,[13] as described below.

The FF, bound-free (BF), and Compton radiography techniques are distinguished by the properties of the respective dominant absorption or scattering processes involved. The FF and BF processes have strong material dependence and share the same ν^{-3} spectral dependence, while the effective radiographic mass absorption coefficient of Compton scattering is only weakly dependent on material composition and the backlighter spectrum. Figure 123.23 shows these three individual contributions [FF (red), BF (blue), Compton (black)] plotted for deuterium (solid lines) at a typical coasting-phase shell condition, $\rho = 3$ g/cm^3 and $kT = 25$ eV, and for carbon (dashed lines) at $\rho = 0.5$ g/cm^3 and at a higher temperature, $kT = 100$ eV, where it might exist in trace concentrations at the outer edge of the imploding shell, near a cooling remnant of the hot ablation region. Blue ovals indicate the key process and typical spectral range for FF radiography of cryogenic D_2 shells, BF radiography of warm CH shells, and Compton radiography of most materials. For the purpose of radiography, it is acceptable to think of opacity or attenuation being caused by Compton scattering, even though Compton scattering is not an absorption process in which photons are destroyed. At the photon energies being considered, the scattering is only about 30% stronger in the forward direction than the backward direction.[14] This is sufficiently isotropic that nearly every scattered photon is effectively removed from the field of view, as if it has

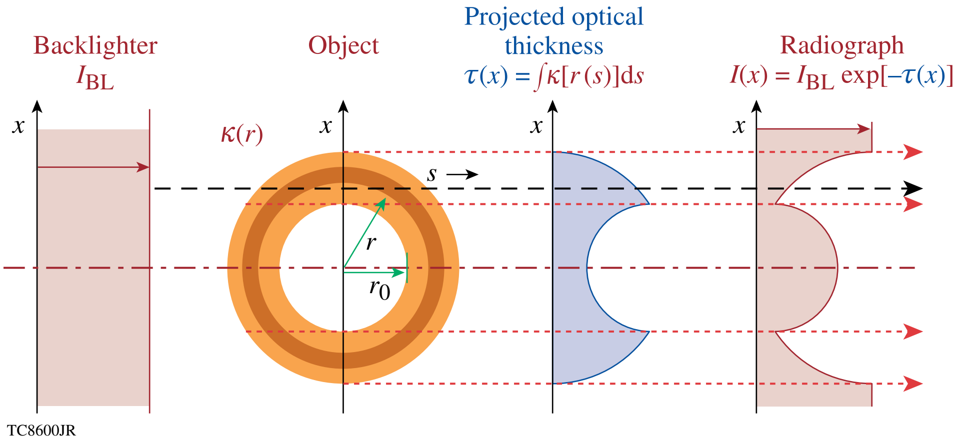

Figure 123.22
Hollow shells with radial opacity profiles $\kappa(r)$ form characteristically limb-darkened circularly symmetric shadows in the image plane, here represented as $I(x)$. A typical backlighter emission ray is shown sampling the absorbing shell on its way to the image plane, where the recorded intensity is determined by the integral of the opacity along its path, the projected optical thickness. Abel inversion recovers the radial opacity distribution from the optical depth profile projected onto the image plane.

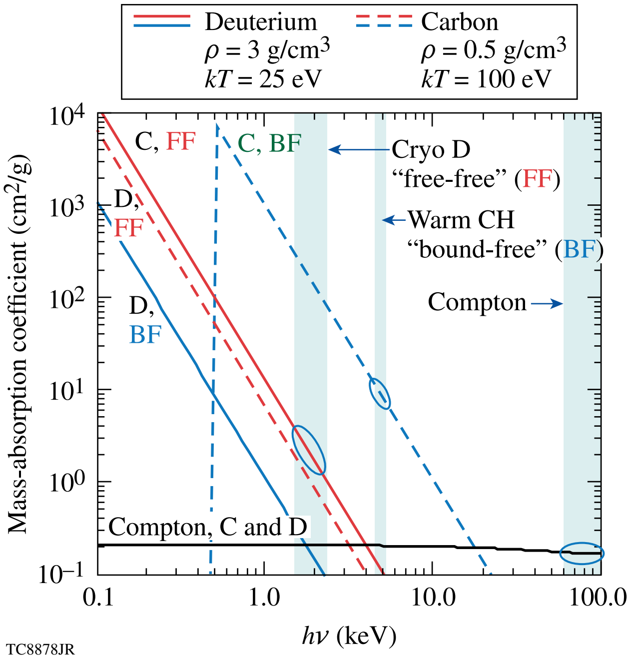

Figure 123.23
The FF, BF, and Compton radiographies are distinguished by the properties of the respective attenuation processes involved. FF and BF mass-absorption coefficients have strong material and spectral dependence, while the effective mass-absorption coefficient of Compton scattering is only weakly dependent on material composition and the backlighter spectrum. The individual process [FF (red), BF (blue), Compton (black)] contributions are plotted for carbon (dashed lines) and deuterium (solid lines) at a typical set of coasting-phase conditions for an imploding deuterium shell. Blue ovals indicate the key process and spectral region for FF radiography of cryogenic deuterium shells, BF radiography of warm CH shells, and Compton radiography of most materials.

been absorbed, so the total Compton-scattering cross section for radiography may be treated as an absorption cross section.

Target optical thicknesses of order unity are desirable for radiography. As a typical OMEGA target implosion approaches peak compression, the mass areal density of a shell grows by more than an order of magnitude within roughly 100 ps, peaking at roughly 0.3 g/cm^2 (Ref. 3). Based on this, the mass-absorption coefficients in the neighborhood of 10 cm^2/g are appropriate. For BF and FF radiography, which share the same strong ν^{-3} spectral dependence, this determines the appropriate range of backlighter energy. The Compton cross section, on the other hand, given by the Klein–Nishina formula, varies very slowly with photon energy out to 100 keV (Ref. 15), the upper limit of hard x-ray backlighters proposed thus far.[8] This makes Compton scattering the dominant radiography process for light elements at high-photon energies. The advantage of radiography with hard x rays is that the self-emission of the imploded target, which decreases rapidly with photon energy as $\exp(-h\nu/kT)$, does not create significant background intensity at these high backlighter photon energies. The main disadvantage of Compton radiography is that the attenuation by OMEGA-imploded shells is small, of the order of several percent at peak compression. An advantage of Compton scattering is that its very weak spectral dependence simplifies the analysis of Compton radiographs. With broadband BF and FF radiography, the spectral content of the backlighter and the spectral response of the imaging system must be known accurately because of the strong spectral dependence of BF and FF opacity. The weak spectral dependence of Compton scattering is also a disadvantage because one cannot adjust the backlighter energy to obtain anything more favorable than weak attenuation. Compton radiography will be better suited to the NIF,[5] where implosions approaching the 3.0-g/cm^2 mass areal density required for ignition[16] will provide optical thicknesses an order of magnitude larger than on OMEGA.

The mass-absorption-coefficient curves for Compton scattering by carbon and deuterium are indistinguishable, so they are represented by the same black curve in Fig. 123.23. For hard x rays, all electrons, free and bound, contribute identically to the mass-absorption coefficient.[15] Since most of the naturally occurring elements from helium through chlorine have equal proton and neutron numbers, they have very nearly the same number of electrons per mass and, therefore, very nearly equal Compton mass-absorption coefficients. The mass-absorption coefficient of heavier elements decreases slowly with atomic number, as the proton/neutron number ratio decreases. Under compressed-shell conditions beyond the late coasting phase, carbon is more opaque than hydrogen by a few orders of magnitude, due, in large part, to the strong atomic-number Z^4 scaling of the K-shell photoionization cross section and the dominant abundance of helium-like carbon, with two bound K-shell electrons per ion. Hydrogen, on the other hand, has a negligible population of bound states under these conditions and, as a result, absorbs primarily through FF absorption. This means that a trace of carbon impurity in an imploding hydrogen shell will dominate its radiograph. If the purpose of the radiograph is to observe the mass distribution, then a hydrodynamically irrelevant trace of carbon contaminant can substantially alter the apparent mass distribution in a FF radiograph of an imploding cryogenic shell, while Compton radiographs will remain largely unaffected. If the purpose of the radiograph is to detect carbon contamination by fuel–shell mix, it will be visible through its high BF opacity at the soft energies of FF radiography and invisible at the hard energies of Compton radiography.

In the case of radiography of CD shells,[7] the opacity is dominated by the BF opacity of the helium-like species of carbon over the wide range of temperature and density expected in imploding shells. The remaining dependencies are $\rho\nu^{-3}$. Assuming that the backlighter spectrum and the detector response define a single effective photon energy, the opacity becomes simply a product of the mass density ρ and a known constant factor. Consequently, each optical thickness measurement is equivalent to a measurement of $\int \rho \mathrm{d}s$, the areal density along a particular line of sight. The analysis of D_2 shell FF radiographs is simplified by the fact that ionization under imploded shell conditions is likely to be sufficiently complete that BF transitions will not compete with the FF opacity. The remaining parameter dependencies are $\rho^2 T^{-1/2}\nu^{-3}$, so each optical thickness measurement in a FF radiograph at a known ν is equivalent to a $\int \rho^2 T^{-1/2} \mathrm{d}s$ measurement. Given an independent determination of the temperature T, such as from another diagnostic or from a simulation, the integral $\int \rho^2 \mathrm{d}s$ remains. The radial density–squared profile can be obtained from this data by Abel inversion, just as has been done with CD shells.[7] The uncertainty of the density inferred from FF opacity is correlated with the uncertainty in the temperature, but only weakly, since the temperature scaling of FF opacity is $T^{-1/4}$, relative to the density dependence.

The opacities of both CD and D_2 follow these simple temperature and density-scaling laws over much of the range of conditions of compressed imploded shells. This is shown in Fig. 123.24 in two plots of their respective temperature-and-density–scaled opacities as functions of temperature. The photon energy is fixed at $h\nu = 2$ keV, and the scaled opacity is plotted for four different densities roughly a factor of 10 apart. In Fig. 123.24(a), the plotted quantity is equal to the opacity divided by ρ, corresponding to the scaling of BF absorption, which dominates the opacity of CD; Fig. 123.24(b) shows the opacity of D_2 divided by $\rho^2/T^{1/2}$, corresponding to the scaling of FF absorption, which dominates the opacity of D_2 under these conditions. The nearly constant value over a wide range of temperature indicates the validity of the respective temperature and density scalings. The CD opacity drops from this scaling at temperatures above 100 eV because the bound electrons are removed by collisional ionization and rises above this scaling at the highest density because of the contribution of FF absorption that grows with density as ρ^2. The simple scaling of the FF opacity of D_2 is seen to hold for all the conditions plotted, except for the lowest density, where bound electron

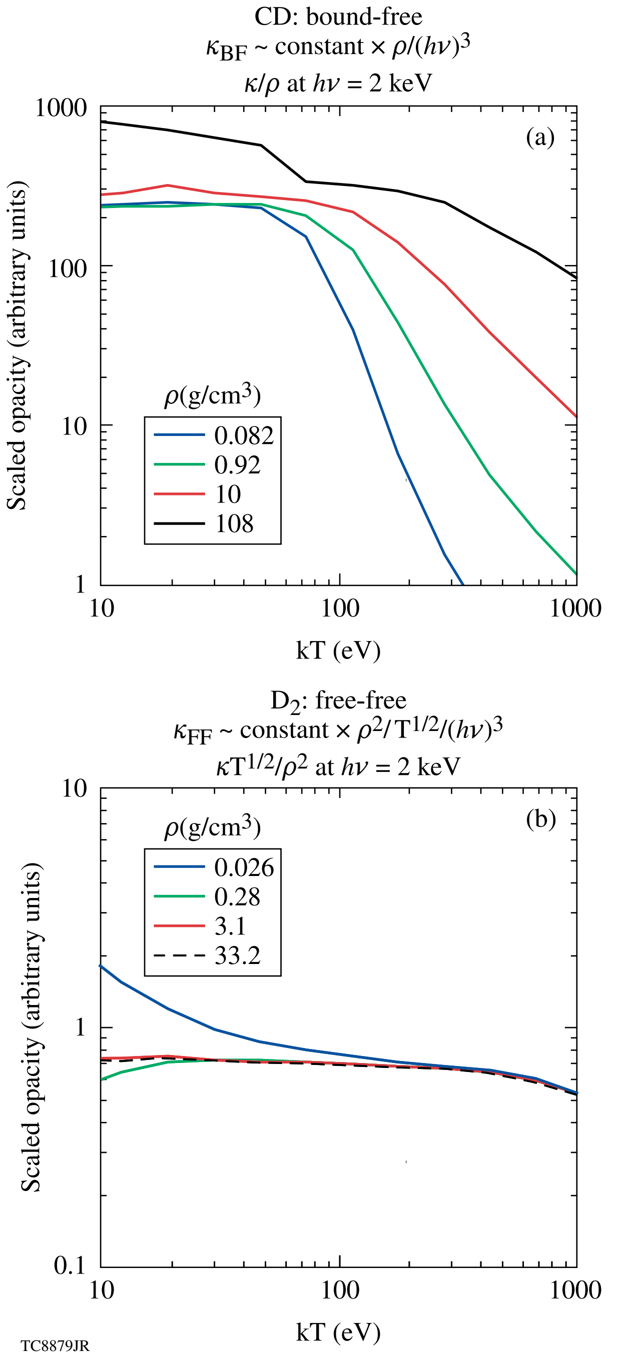

Figure 123.24
The opacities of CD and D_2 both follow simple temperature- and density-scaling laws that cover much of the range of conditions of compressed imploded shells. This is shown in two plots of their respective scaled opacities as functions of temperature. Plot (a) shows the opacity divided by ρ, corresponding to the scaling of BF absorption, which dominates the opacity of CD. Plot (b) shows the opacity of D_2 divided by $\rho^2/T^{1/2}$, corresponding to the scaling of FF absorption, which dominates the opacity of D_2 under these conditions. The scaled opacities are plotted for four different densities at roughly a factor of 10 apart. The photon energy is fixed at $h\nu$ = 2 keV.

states become marginally abundant at the lowest temperatures. The scaling of the FF opacity is not as simple as that of BF opacity, but it appears to be slightly more reliable, at least over the conditions and spectral range shown.

Ideally, the backlighter should be monochromatic so that ν is a known constant. If the opacity of the object varies significantly over the joint bandwidth defined by the backlighter spectrum and the detector response, it can significantly alter the transmitted backlighter spectrum. Therefore, however one might define a spectrum-averaged backlighter energy, its value may vary over the plane of the radiograph. This almost certainly will not be an issue with Compton radiography since the effective opacity, as shown in Fig. 123.23, varies very slowly with photon energy. In any case, the main benefit of a narrow-bandwidth detector is that it limits the background caused by self-emission from the target.

Feasibility of Soft X-Ray Free-Free Radiography

The simulation of cryogenic implosion radiography employs several tools. The target implosions are simulated in 1-D by *LILAC*[17] and in 2-D by *DRACO*,[18] which includes the effects of target offset and irradiation nonuniformity (see "Two-Dimensional Simulations of the Neutron Yield in Cryogenic-DT Implosions on OMEGA," p. 111). The short-pulse foil hydrodynamics are simulated in 1-D by *LILAC*. Both the backlight emission and the implosion radiography are simulated separately by the post-processor Spect3D.[19] Spect3D calculates radiation transport using tabulated opacity and emissivity data based on detailed atomic models for the radiograph simulations. For the backlighter simulations, these quantities are calculated in real time, using time-dependent, non-LTE atomic-level kinetics, including self-consistent nonlocal photoexcitation.

The radiographs are simulated from the opacity distributions within the object that are obtained from hydrodynamic simulations. The calculation takes into account the spectral, spatial, and temporal responses of the imaging device as well as the backlighter spectrum. This fully accounts for the finite-bandwidth effect discussed above.

Figure 123.25 shows a *DRACO*/Spect3D-simulated radiograph of a successful OMEGA cryogenic implosion. This implosion, shot 47206, reached a measured areal density of 202±7 mg/cm^2 (Ref. 20). The radiograph, which is shown in (b), shows the shadow of the simulated mass-density profile at the time of peak compression, which is shown in (a). This contour plot is a cross section of the density distribution in a plane intersecting the imploded shell along its vertical symme-

(a)
Shot 47206: 10-μm shell, 95 μm of cryo D_2
Mass-density profile at
peak compression, t = 4.1 ns

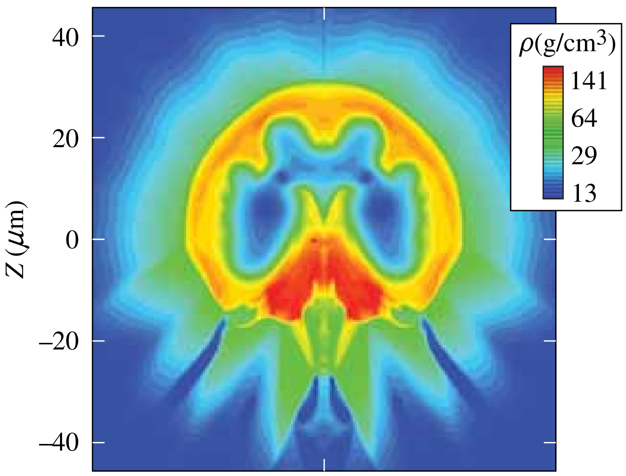

(b)
Al Ly$_\alpha$ radiograph;
30-ps, 10-eV, 1-μm resolutions
kT$_{\text{backlight}}$ = 500 eV

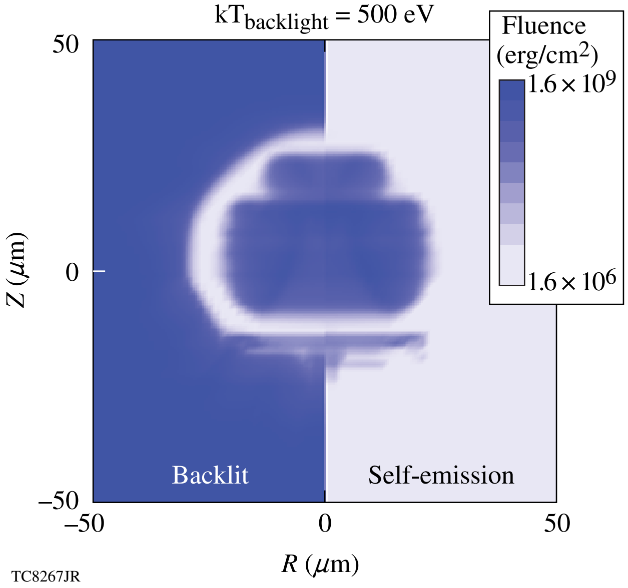

Figure 123.25
A *DRACO*/Spect3D-simulated radiograph of a successful OMEGA cryogenic implosion at peak compression is shown in the left "backlit" half of the split frame in (b). This implosion, shot 47206, reached a measured areal density of 202 mg/cm^2 (Ref. 20). The simulated mass density profile at this time is shown in cross section in the contour plot in (a). The coordinates (R,Z) refer to a cylindrical geometry with the symmetry (Z) axis in the vertical direction. The simulated radiograph in the left side of the split image in (b) was backlit at the H-like aluminum Ly$_\alpha$ emission line energy at a brightness temperature of 500 eV. The right half of the split image in (b) shows only the self-emission with no backlighter contribution. The imaging device is restricted to a 10-eV bandwidth, a 30-ps integration time, and a 1-μm spatial resolution.

try axis. The asymmetries of the imploded shell are the result of irradiation nonuniformity caused by target offset, beam imbalance, and the shape of the individual beam profile at the target surface. The cylindrical coordinates (R,Z) are defined with the symmetry (Z) axis in the vertical direction. The left-hand side of the split image in (b) shows the simulated radiograph of this density distribution, including the backlighter. The right-hand half of the image is the exact mirror image of the radiograph in (a), except that the backlighter contribution is not included, leaving only the self-emission. The imaging device is restricted to a bandwidth of 10 eV. The backlighter is assumed to be the Ly$_\alpha$ emission line of H-like aluminum at a brightness temperature of 500 eV, which corresponds to an intensity of about twice that of the shell's self-emission at this line energy, which peaks at about this time. This intensity has been exceeded in backlighter development experiments,[21] but it has been chosen here to illustrate the useful information available with a backlighter that does not overwhelm the self-emission. The 30-ps integration time, which is comparable to currently available gating times, takes into account the blurring effects of source motion. The 1-μm spatial resolution of the simulation is much better than will be available with current instrumentation, but it shows the amount of information that could be available with improved resolution.

Most of the structure seen in the shell mass distribution is visible in the radiograph [Fig. 123.25(b)]. At the bottom of the shell, the flow appears to have formed a dense concentration of mass that has preceded the rest of the shell toward the center. The shadow of such a dense concentration of shell material should be seen distinctly in the backlit portion of the image on the left-hand side of the frame, but it is very faint. Seeing how similar this cone-shaped concentration appears in the backlit side of the frame and in the self-emission side, one concludes that it is filling in its own shadow with its own emission. The inner-surface emission from the shell behind it is being blocked along with the backlighter. The falling radial temperature gradient and the rising radial density gradient create a surface of maximum emissivity at the interior of the shell. As has been shown with BF radiographs of warm polar-drive implosions,[7] the portion of the shell outside this emitting surface forms a shadow on the radiograph that may be analyzed. As long as this shell absorption is physically separated in the radiograph from the inner-surface self-emission, it can be measured. As this example demonstrates, however, self-emission is capable of hiding substantial amounts of shell mass.

Over the 30-ps integration time, the self-emission is dimmer than the hypothetical backlight but strong enough to reduce confidence in the absorption of the shadow of the shell limb. The shape of the shell is still apparent with this marginally intense hypothetical backlighter. Higher backlight intensity will be available that will compensate for the excess self-emission admitted by gating times that are longer than the backlight pulse and by spectral pass bands that extend past the spectral width of the backlighter.

The image contrast in a FF radiograph of an imploding cryogenic shell can change from nothing to saturation in a very short time because of the rapid approach to peak shell density, coupled with the strong ρ^2 density scaling of the FF opacity. The spectrum of the backlighter must be chosen so that the shell transmission produces optimum radiographic contrast at a chosen time. The contour plot in Fig. 123.26 shows the transmission of a ray passing through the center of the *DRACO* simulation shown in Fig. 123.25 as a function of time and backlighter photon energy. This plot is repeated, once with the Al K-shell line energies indicated and once with the energies of the H-like Ly$_\alpha$ lines of several possible backlighter materials indicated. At any one of these line energies, the lineout across the plot gives the transmission as a function of time. This transmission varies dramatically, reaching a minimum at maximum compression near 4.15 ns. For a particular backlighter energy, Fig. 123.26 shows the times at which a desired transmission value is likely to occur. Similarly, the contour corresponding to a desired transmission value gives, as a function of time, the backlighter photon energy that would provide this transmission value. If, for example, the contour at the transition from yellow to orange indicates a suitable transmission value, it crosses the aluminum K-shell line energies roughly 100 ps before peak compression, indicating that these lines are suitable backlight sources at this time. Materials with higher line energies will provide the same degree of contrast later in time.

Figure 123.27 shows the expected performance of an Al backlighter. The time-resolved spectrum in (a) represents the simulated spectral flux from a 10-μm aluminum foil irradiated with an 8-ps Gaussian pulse at 10^{18} W/cm^2. The strongest feature is the Ly$_\alpha$ emission line of the hydrogen-like species, but a great deal of energy is emitted in other spectral features, including continuum above 2.2 keV. This continuum would create a uniform background, were it not removed by iridium reflectors, as was explained earlier and shown in Fig. 123.20. The specific intensity at the Ly$_\alpha$ line center is shown in (b) as a function of time. This emission appears as a pulse lasting 5 ps, centered close to the laser pulse. The specific intensity of this emission line can be compared with that of the time-dependent self-emission expected from a cryogenic implosion

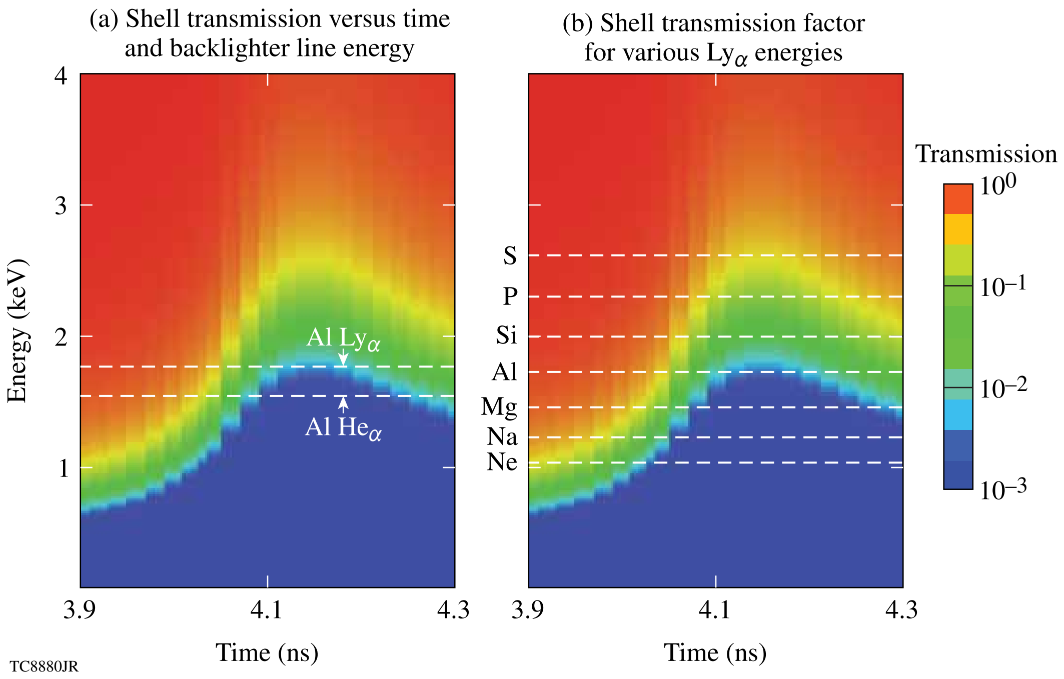

Figure 123.26
The image contrast in a FF radiograph is determined by the transmission of the imploded shell at the effective photon energy of the backlighter. The transmission of a ray at the center of a *DRACO*-simulated radiograph of shot 47206 is shown plotted as contours as a function of time and backlighter photon energy. This plot is repeated, once with the Al K-shell line energies indicated and once with the energies of the H-like Ly$_\alpha$ lines of several possible backlighter materials indicated. The backlighter energy giving a particular transmission value at a particular time can be read as a function of time by following the corresponding contour.

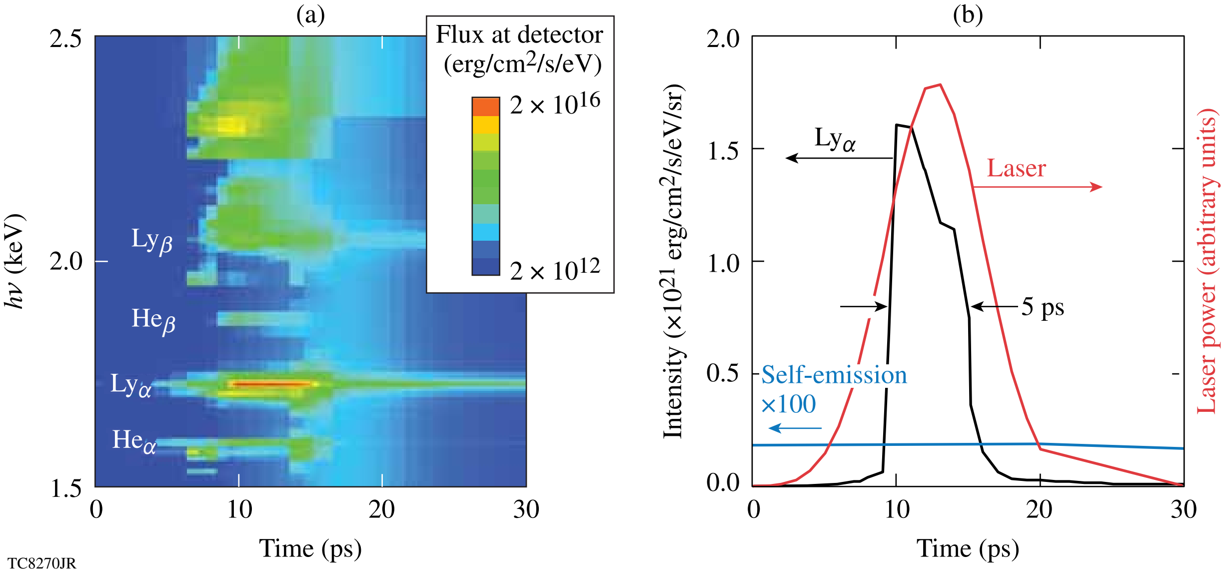

Figure 123.27
The simulated time-resolved spectrum in (a) represents the spectral flux from the surface of a 10-μm aluminum foil irradiated with an 8-ps Gaussian pulse at 10^{18} W/cm^2. The specific intensity centered at the Ly$_\alpha$ line is shown in (b) plotted as a function of time. This emission appears as a pulse lasting 5 ps, centered near that of the laser pulse, plotted in red. This emission line is much more intense than the self-emission expected from a cryogenic implosion on OMEGA. The blue curve represents 100× the specific intensity obtained from an implosion simulation, assuming that all the self-emission of a simulated imploded cryogenic core emerges from within a 20-μm-radius circle.

on OMEGA. The time scale of the simulated implosion has been shifted so that the peaks of the self-emission and the backlight line intensity coincide. The blue curve represents 100× the specific intensity obtained assuming that the entire self-emission of a simulated imploded cryogenic core emerges from within a 20-μm-radius circle. Clearly, the Ly$_\alpha$ line can provide a backlight source that is potentially two orders of magnitude more intense than the self-emission background. The self-emitted continuum lasts much longer, however, than the short duration of the backlighter and covers a much wider bandwidth than the backlighter spectral line, so short framing times and narrow bandwidths are essential for restricting the self-emission background to acceptable levels.

The simulated spectral fluence is compared in Fig. 123.28 with the measured time-integrated spectral emission from a similar experiment on the OMEGA EP laser. The consistency of the simulated and measured aluminum Ly$_\alpha$ fluence is encouraging. The irradiance of 1.25×10^{18} W/cm^2 in the simulation is slightly higher than the 5×10^{17} W/cm^2 average in the experiment, which anticipates the likelihood that more-intense portions of the nonuniform beam are dominating the spectral emission. To convert the measured fluence to a time-integrated specific intensity that can be compared directly with the simulated time-integrated emission, it is assumed that the measured fluence was emitted within a length of time equal to the backlighter laser pulse width and from within its nominal 23-μm laser-spot radius. With these assumptions, the simulated and measured Ly$_\alpha$ fluences are close. The measured He$_\alpha$ fluence, on the other hand, is much higher than the simulated level. The measured background continuum is also much higher than the simulated level. These discrepancies are probably due to emission from the foil outside the directly illuminated spot that has been heated by both thermal and nonthermal electron transport. The formation of a large, relatively cool radiating area surrounding the laser spot, following the absorption within the laser spot, has not been taken into account in the 1-D *LILAC* simulation. Even though the colder radiating area would be dimmer than the original hot area under the laser, it could be larger and longer lasting, resulting in a substantial contribution to the total fluence. The agreement in the Ly$_\alpha$ emission indicates that the prompt emission from the laser spot is modeled reasonably well. The He$_\alpha$ emission certainly comes from a lower temperature and a larger area than the Ly$_\alpha$ source because material producing more He$_\alpha$ emission than Ly$_\alpha$ emission can have a temperature of no more than about 500 eV. At this temperature, the blackbody limit on the line emission rules out the possibility that such a source could produce the observed He$_\alpha$ fluence in a time as short as the laser pulse width and from an area as small as the laser-spot area. If the Ly$_\alpha$ emission is prompt and the He$_\alpha$ emission is over an extended period of time, then it is the Ly$_\alpha$ emission that will be favored by the time gating of the x-ray framing camera. Given the ν^{-3} dependence of the FF opacity of the imploded shell, uncertainty as to which of these two spectral lines is dominating the backlighter over the gating time corresponds to less than a 24% uncertainty in the shell opacity to be used in the radiographic analysis. With reasonable progress in backlighter spectroscopy or by implementing narrow-band imaging, this uncertainty will diminish substantially.

For comparison, the time-integrated self-emission intensity from the previous simulated cryogenic implosion example is plotted as the blue curve in Fig. 123.28, assuming for the purposes of this estimate that the source is a disk with a 20-μm radius, which is very close to the image size at peak core emission. This self-emission is much lower than the Ly$_\alpha$ spectral fluence, indicating that the implosion radiographs can be substantially free of self-emission, with some tolerance of longer

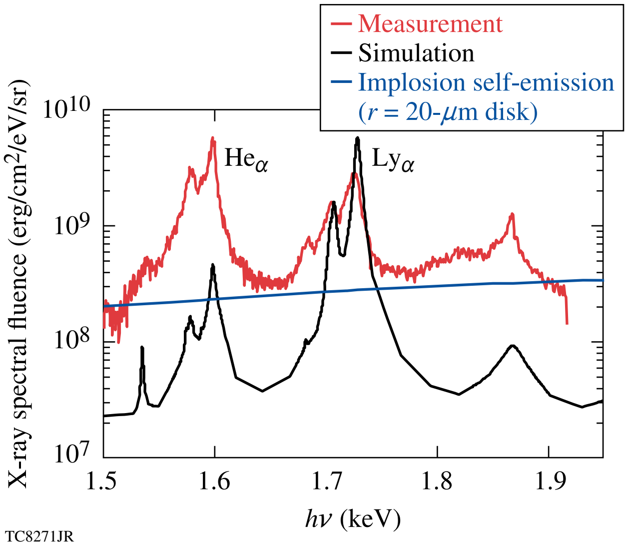

Figure 123.28
The measured and simulated spectral fluence from an aluminum foil target are compared, assuming identical pulse widths and similar irradiances and assuming that all emission comes from within a 23-μm laser spot. The simulated aluminum Ly$_\alpha$ time-integrated spectral fluence is consistent with the measured spectral emission. Agreement over the entire spectrum cannot be expected from a 1-D simulation like this because nonthermal electron transport to non-irradiated portions of the foil is not modeled. Agreement in the Ly$_\alpha$ fluence indicates that emission from the directly irradiated spot is modeled reasonably well and that useful backlighter intensities can be attained. The time-integrated intensity from a simulated cryogenic implosion is plotted for comparison, assuming that the effective source is a 20-μm-radius disk, which is very close to the core image size at peak core emission.

integration times and camera bandwidths that are slightly wider than the backlighter spectral line.

DRACO/Spect3D-simulated radiographs of the cryo implosion shown in Fig. 123.25, shot 47206, have been obtained using the simulated backlighter spectrum shown in Fig. 123.27. Three images, representing the 100 ps leading up to the time of peak compression, are shown in Fig. 123.29. The spectral interval used is 10 eV in width, centered at the aluminum Ly_α energy. These radiographs show a very rapid increase in image contrast, roughly an order of magnitude in each 50-ps time step. At this backlighter energy, the 100 ps shown is the extent of the useful time interval for radiography with Al lines, because of the loss of contrast at the early end of this interval. As explained above, the degree of radiographic contrast obtained at a given time in the implosion can be adjusted by changing the backlighter material. The simulated backlighter intensity is high enough in these radiographs to overcome the self-emission. The image at 4.1 ns shows the shadow of the mass concentration at the bottom of the imploded shell, which was not visible in the simulated radiograph in Fig. 123.25, obtained with marginally adequate backlighter intensity. The simulated spatial resolution of 5 μm allows one to see much of the detail of the mass distribution in Fig. 123.25. The assumed temporal resolution is 30 ps and the shell motion is taken into account. The effects of the assumed spatial resolution of 5 μm and the smearing resulting from shell motion during the 30-ps time gate are comparable.

Feasibility of Hard X-Ray Compton Radiography

Simulated Compton radiographs are obtained from *DRACO* and *LILAC* simulations using the same Spect3D postprocessor as the simulated FF radiographs. The effective opacity is much simpler. Along any line of sight, the density path integral $\int \rho \mathrm{d}s$, and the effective optical depth τ are very simply related by

$$\tau = \frac{\sigma_{\mathrm{KN}}(h\nu)}{m_{Z,A}/Z} \int \rho \mathrm{d}s, \tag{1}$$

where $\sigma_{\mathrm{KN}}(h\nu)$ is the Klein–Nishina total cross section for the Compton scattering of a photon.[14,15] This cross section varies very slowly over the 50- to 100-keV spectral range used for Compton radiography, and, at these energies, all electrons in the material, both bound and free, contribute equally to the effective opacity. Consequently, the areal electron density is obtained from the areal mass density by dividing by $m_{Z,A}/Z$, the mass per electron of the shell material, specified here by its atomic number Z and mass A. Since the mass per electron is about two atomic mass units, decreasing slowly with increasing atomic number, the effective opacity has a very weak material dependence.

The three *DRACO*/Spect3D-simulated radiographs of shot 47206 in Fig. 123.29 are calculated again and shown in Fig. 123.30 at the same times and spatial resolutions, but with

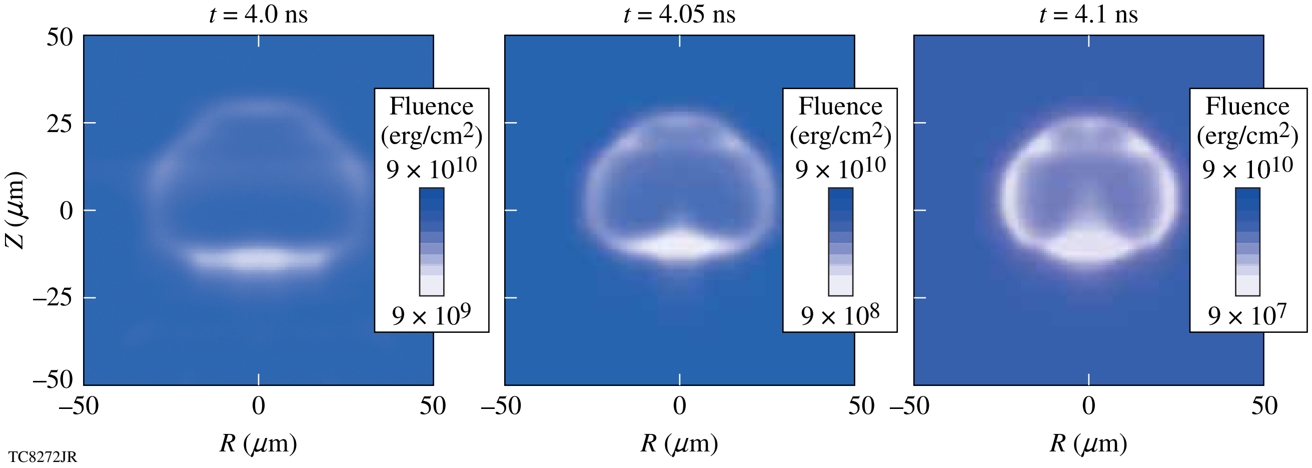

Figure 123.29
Three simulated FF radiographs leading up to the time of peak compression are shown, based on the same simulation shown in part in Fig. 123.25 and the backlighter spectrum shown in Fig. 123.28. The spectral interval used is 10 eV in width, centered at the aluminum Ly_α energy. The assumed spatial resolution is 5 μm and the temporal resolution is 30 ps. These images illustrate that useful detail is visible and also that radiographic contrast increases very rapidly as peak compression is approached.

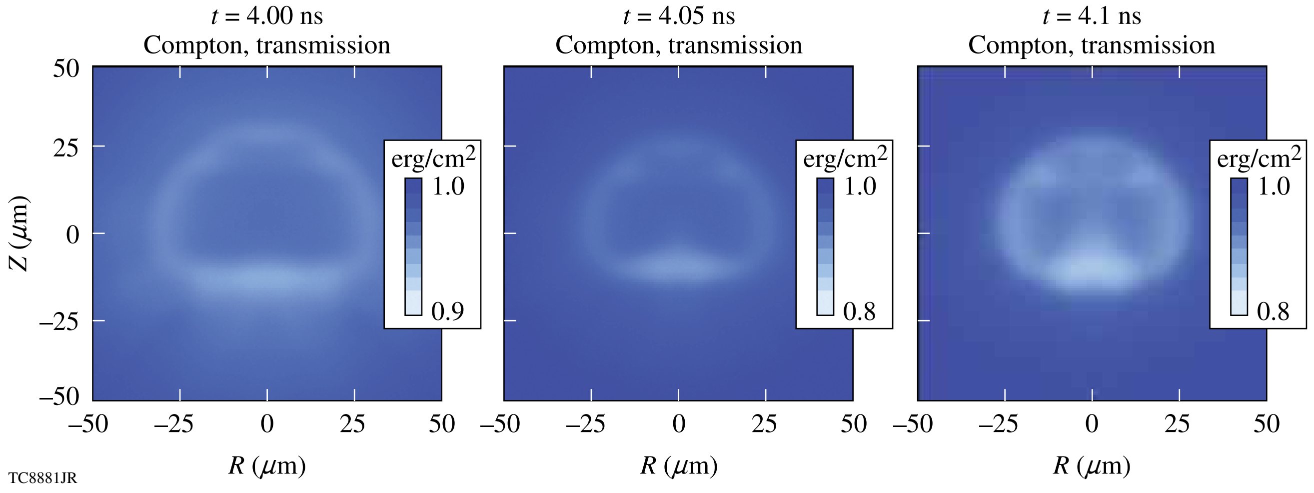

Figure 123.30
The three *DRACO*/Spect3D-simulated radiographs of shot 47206 in Fig. 123.29 have been obtained at the same times and spatial resolutions but with a backlighter energy of 57 keV, where Compton scattering forms the image. The time resolution is 10 ps, the pulse width claimed for recent Compton radiograph experiments with warm CH shells. The Compton radiographs appear almost identical to the FF radiographs, except for their very weak transmission signal.

a backlighter energy of 57 keV, where Compton scattering forms the image. The time resolution is 10 ps, the pulse width claimed for recent Compton radiograph experiments with warm CH shells.[9] The Compton radiographs appear almost identical to the FF radiographs, except for their very weak transmission signal. The contour scales are linear and cover only the range of transmission needed to bring out the image, while the FF radiographic images in Fig. 123.29 require logarithmic scales covering up to three decades to span their full dynamic range. The backlighter photon energy of 57 keV corresponds to the inner-shell K_α decay transition of tantalum. Since this simulation was done, higher energy sources have been considered, including bremsstrahlung up to 100 keV (Ref. 8), but the result of this simulation would change negligibly if this were taken into account, owing to the weak energy dependence of the Klein–Nishina cross section.

A *LILAC*/Spect3D simulation of a sequence of Compton radiographs has been obtained for the 120 ps leading up to the time of peak compression of a more-recent cryogenic implosion, shot 55723. The simulated peak areal density was 370 mg/cm^2, and the measured value was 300 mg/cm^2 (Ref. 3). The simulated shell areal density and neutron emission rate are plotted as functions of time in Fig. 123.31(a). The simulated radiographs are circularly symmetric because the *LILAC* simulation is spherically symmetric, so the simulated radiographs are represented as radial transmission profiles in Fig. 123.31(b). The transmission profile curves are color keyed to a legend giving the image times and also to time markers in (a). This shows that the imaging device must be sensitive to a 15% attenuation signal. A much greater sensitivity will be required for quantitative radiography at earlier times. Sensitivity to less than 4% attenuation will be needed to make measurements 120 ps before peak compression. This series of radiographs shows that both the radial convergence and the transmission are measurable indicators of compression. The core shadow shrinks and sharpens with the approach to peak compression, but the opaque limb of the image converges by only 10 μm over the 120 ps shown, making this motion difficult to measure, given the 10-μm image resolution imposed by the size of the point backlighter. These radiographs were simulated without allowance for temporal or spatial resolution.

Analysis of Free-Free Radiographs

The FF radiographs obtained thus far have been analyzed as if they were shadows of spherically symmetric objects. The formation and analysis of the radiograph of a spherically symmetric object are illustrated schematically in Fig. 123.22 for the case of a hollow spherical shell. Generally, the radial opacity profile $\kappa(r)$ of a hollow spherical shell forms a circularly symmetric intensity distribution $I(x)$, which appears as a characteristically limb-darkened shadow, relative to a uniform backlighter intensity I_{BL}. The optical thickness $\tau(x)$ of a spherically symmetric object is the Abel transform of the opacity profile

$$\tau(x)=\int\kappa\left[r(s)\right]\mathrm{d}s, \tag{2}$$

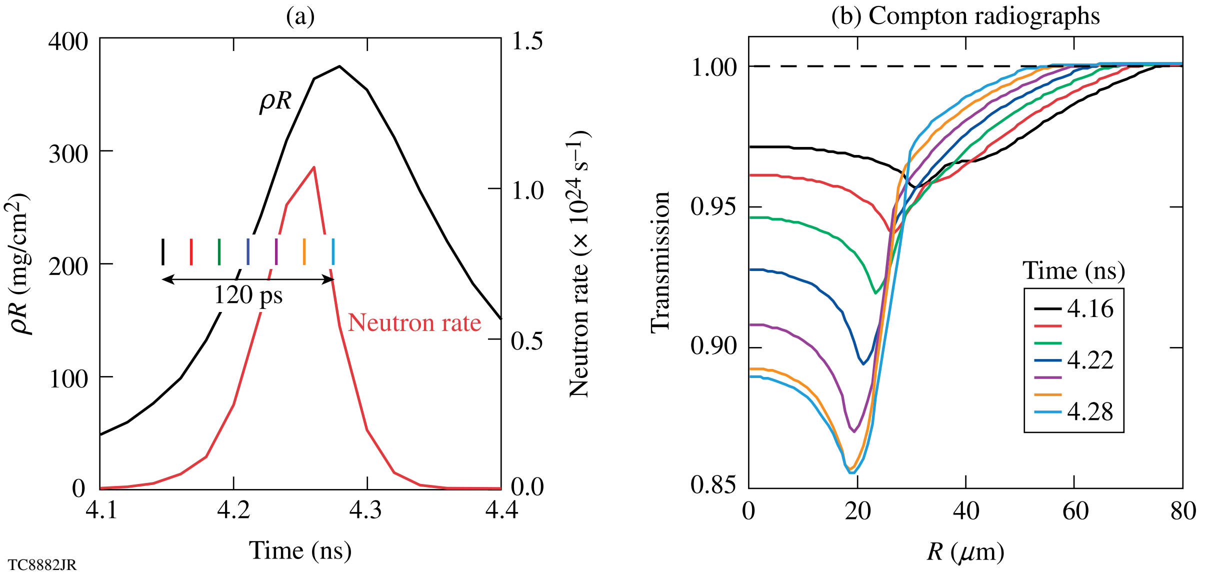

Figure 123.31
A 1-D *LILAC*/Spect3D simulation of a sequence of Compton radiographs has been obtained over the 120 ps leading up to the time of peak compression of shot 55723, which recently attained an areal density of 300 mg/cm^2. The shell areal density and neutron emission rate are plotted in (a) as functions of time. The radiographs are represented in (b) as radial transmission profiles, color-keyed to the time labels in the legend and to time markers in (a). The backlighter photon energy was chosen to be 57 keV. Spatial and temporal resolutions were not taken into account.

where each point on the backlighter ray path s is identified with its distance r from the center of the object. The inverse Abel transform of $\tau(x)$

$$\kappa(r) = -\frac{1}{\pi}\int_r^\infty \frac{\mathrm{d}\tau(x)}{\mathrm{d}x}\frac{\mathrm{d}x}{\sqrt{x^2-r^2}} \tag{3}$$

recovers the spherical opacity profile from the shadow. Limb darkening is the tendency for the radiographic shadow of a uniformly absorbing shell to have a sharp minimum of intensity at a radius equal to the inner radius of the absorbing shell because of the strong peak in $\tau(x)$ at that radius. Obtaining the opacity at a given radius r by Abel inversion requires information from the radiograph only for $x > r$. If, for example, there is an emitting core within a radius r_0, Abel inversion of the radiograph still gives the opacity distribution for $r > r_0$, as long as the shadow is visible for all $x > r_0$. The radial optical thickness can be obtained by evaluating $\int_{r_0}^\infty \kappa(r)\mathrm{d}r$ using Eq. (3) and performing the radial integration analytically to derive a new expression,

$$\int_{r_0}^\infty \kappa(r)\mathrm{d}r = \frac{r_0}{\pi}\int_{r_0}^\infty \frac{\tau(x)}{x\sqrt{x^2-r_0^2}}\mathrm{d}x, \tag{4}$$

which is easier to apply than Eq. (3) if the radial integral is all that is wanted.

A preliminary estimate of the areal density of the imploding target in shot 54395 obtained from a lineout of its radiograph is shown in Fig. 123.32, which illustrates the basic steps of the radiographic analysis. The imploding shell is seen as a crisp shadow near the center of the elliptical backlighter emission spot in (a). The transmission/emission profile is first isolated from this nonuniform backlighter intensity distribution in a highly approximate fashion shown in (b) by fitting an inverted parabola to reconstruct the symmetric rounded top of the backlighter intensity distribution from the portion of the backlighter that is exposed. Emission from the core and from a thin unablated remnant of the original CD shell can be seen peaking above the backlighter intensity in (b). The FF opacity of deuterium at the Al K-shell line energies and a uniform shell temperature estimate of 25 eV from a *LILAC* simulation gives a $\rho^2R \approx 0.097$ g^2/cm^5 for the absorbing shell based on the measured transmission profile and Eq. (4). Assuming that the shell density is uniform, we obtain an areal density of $\rho R \approx 33$ mg/cm^2 within a shell thickness of 110 μm centered at a mean radius of about 140 μm. This areal-density value is consistent with the imploded mass from the *LILAC* simulation of this implosion confined within the shadow radius. Assuming a temperature based on a simulation introduces a weak model dependence into this estimate. The unablated shell mass can be used instead of the shell temperature as a simulation-based parameter.[7] This may be a better choice since, unlike the shell

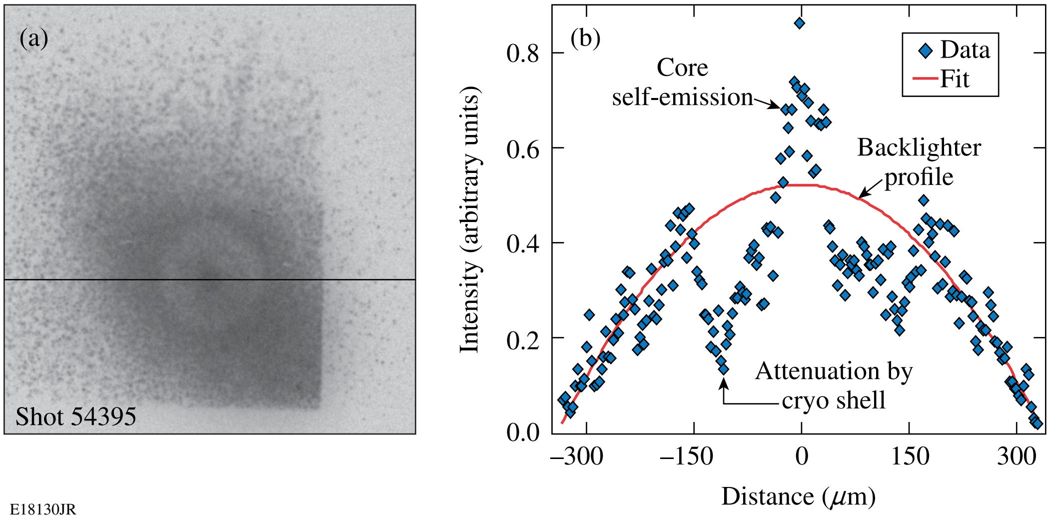

Figure 123.32
A preliminary estimate of the target areal density obtained from a radiograph lineout of shot 54395 illustrates the basic steps of radiograph analysis. The attenuation contribution to the radiograph in (a) is obtained by fitting an inverted parabola model to the backlighter intensity profile shown in (b), where it is not obscured by the imploding shell, and then using this fitted backlighter model profile to infer the backlighter intensity behind the imploding shell. Emission from the core and from a thin unablated remnant of the original CD shell can be seen peaking above the backlighter intensity in (b). The FF opacity of deuterium and a shell-temperature estimate of 25 eV from a *LILAC* simulation give a $\rho^2R \approx 0.097$ g^2/cm^5 value within the absorbing shell. Assuming that the shell density is uniform, $\rho R \approx 33$ mg/cm^2 can be inferred, which is consistent with the imploded mass from the *LILAC* simulation of this implosion.

temperature, it is nearly constant throughout the approach to peak compression, and it allows one to treat the opacity simply as ρ^2 times a constant determined by the imploded mass value. The flat transmission level within the shell's shadow and the crisp outer boundary defined by the self-emission help to define the shell boundaries, but the extra self-emission at this late time, after the laser pulse has turned off, implies an unablated residue of the original CD shell. Simulation of this implosion verifies that shells must be slightly thinner than in this example to avoid an unablated shell remnant. As has been discussed above, even a trace of residual CD can add significantly to the opacity of the shell. Clearly, this compromises our ability to analyze this imploding shell reliably in terms of the FF opacity of pure D_2.

These areal-density and shell-radius estimates are consistent with a *LILAC* simulation of this implosion roughly 300 ps in advance of peak compression, as can be seen in Fig. 123.33. The time uncertainty indicated by the error bars corresponds to the 80-ps gating time of the x-ray framing camera. These estimates are uncertain due to the small amount of radiographic data sampled by the single lineout and the resulting difficulty in identifying the limits of the shell. These results are sensitive to the fitting model of the backlighter intensity profile.

The radiograph of shot 54395 shown in Fig. 123.32(a) is shown again in Fig. 123.34(b). Another view of the same implosion from another pinhole on the framing camera, approximately 40 ps earlier, is shown in Fig. 123.34(a). The separation of the pinholes on the framing camera creates a parallax effect that changes the position of the imploding target relative to the backlighter spot. The radiograph in (a)

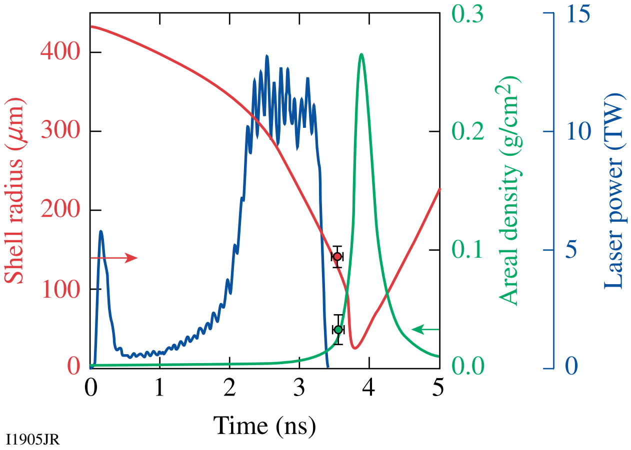

Figure 123.33
The areal density and shell diameter inferred from the preliminary analysis of the first radiograph of shot 54395 are consistent with the *LILAC* simulation of this implosion at a time well before peak compression. Further simulation and analysis of the radiograph indicate that complicating effects of a trace remnant of the original CD shell lends a large uncertainty to the inferred ρR value.

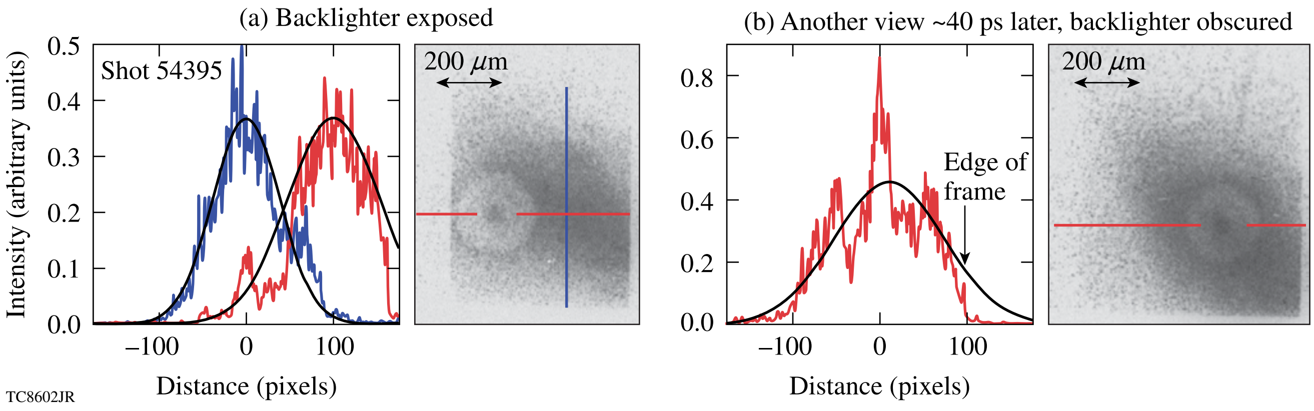

Figure 123.34
Two framing camera views of the same imploding shell, shot 54395, taken at nearly the same time are shown in (a) and (b). Parallax caused by the separation of the pinholes on the framing camera creates images with different target-backlighter orientations. These radiographs are flat fielded with an elliptical Gaussian backlighter distribution model. The superposition of lineouts of the fitted backlighter profile and the radiograph in (a) shows that the elliptical Gaussian profile fits the backlighter profile well. The color of each lineout matches that of the line on the radiograph, indicating the row or column of data represented by the lineout. The good fit of the model distribution to the two orthogonal lineouts in (a) indicates that the attenuation of the center of the backlighter by the imploding target seen in the radiograph in (b) is probably being isolated properly with this model.

shows the center of the backlighter spot exposed, while the radiograph in (b) shows the target well-centered over the backlighter spot, providing a strong absorption signal over the entire target. These radiographs are flat fielded, assuming that the backlighter has an elliptical Gaussian distribution. The plots show lineouts of the radiographs superimposed on the same lineout of the fitted backlighter model. Each lineout is taken along the row or column of data indicated on the radiographs by the line with the matching color. Plot (a) shows that a good fit is obtained over nearly the entire spot, which indicates that the backlighter is being represented properly when this fitting model is applied to the radiograph in (b), where the center of the backlighter distribution is obscured. After the radiograph is flat fielded with the fitted backlighter distribution, the transmission image of the target remains, which is then circularly averaged and Abel inverted to obtain the radial opacity profile of the imploded shell.

The radiograph of shot 54395 in Fig. 123.32(a) has been analyzed using an elliptical Gaussian intensity model fit to the exposed portion of the backlighter spot. The resulting transmission distribution is circularly averaged about the center of the shell shadow and plotted as the blue curve in both frames of Fig. 123.35. The inverse Abel transform given by Eq. (3) is applied to this transmission profile, obtaining a radial opacity profile. This opacity profile is the ρ^2 profile, the density scaling of FF opacity, to within a constant factor that is determined by the total unablated shell mass 34.8 μg obtained from a *LILAC* simulation. The resulting density profile is plotted in red in both frames of Fig. 123.35. Radial transmission profiles were obtained from a *LILAC*/Spect3D simulation at three times covering a 200-ps range centered at the time of the measurement indicated in Fig. 123.33. These are plotted in Fig. 123.35(a), where the measured radial transmission profile is emphasized as a heavy blue curve for easier comparison. The simulated mass density profiles at these three times are plotted in Fig. 123.35(b) along with the measured mass-density profile, plotted in this frame as a heavy red curve. The mass-density distribution is strongly peaked toward the outside of the shell, resulting in an areal density ρR = 19 mg/cm^2, not quite consistent with the preliminary estimate shown in Fig. 123.33. Assuming a 25-eV shell temperature, which is applicable to this time interval, an analysis based on the FF opacity of pure D_2 gives a much higher value of ρR = 47 mg/cm^2, suggesting that the shell is more opaque than a simple understanding of D_2 opacity would lead one to expect.

The simulated and measured transmission profiles in Fig. 123.35 both show transmission factors greater than unity at some radii, which indicates self-emission contributions from the core and from near the outer radius of the shell. The absolute backlighter intensity was not available for the radiographic simulation, so the simulation uniform backlighter intensity value was chosen to have roughly the observed strength of the backlighter relative to the self-emission at the time when the rapidly rising core self-emission and the outer-shell self-emission are comparably intense. The result in Fig. 123.35 is that the exterior self-emissions compare well, while the

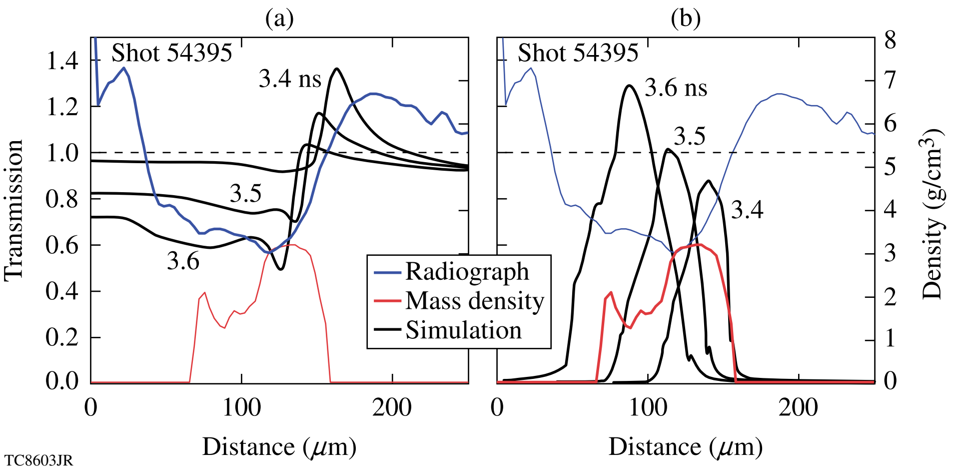

Figure 123.35
The simulation of shot 54395 by *LILAC* shows that a trace of the original CD shell remains unablated. The Spect3D simulated radiographs take this into account and show some resemblance to the measured radiograph between 3.5 and 3.6 ns. The central self-emission is underpredicted at this time, relative to the exterior self-emission, but the amount of unablated CD is known well enough for the simulated and measured exterior self-emissions to match reasonably well. Plots (a) and (b) both show the circularly averaged radial transmission profile and the mass-density profile that is recovered from it by Abel inversion. In (a), the transmission profile (blue) is emphasized and compared with simulated transmission profiles; in (b), the inferred mass-density profile is emphasized (red) and compared with the corresponding simulated mass-density profiles. The inferred density profiles are normalized to the simulated imploded mass. The mass-density profile inferred from analyzing the radiograph in terms of the opacity of D_2 is compromised by the unablated CD, even though it is a small remnant of minimal hydrodynamic importance. The dashed line indicates unit transmission.

simulated core self-emission has not grown to the measured level. It is probably more reliable to match the exterior self-emission since the source is the residual and unablated shell CD, which is predicted to be present in the 1-D simulation, while the strength of the measured shell absorption suggests that shell CD may have mixed into the center of the implosion, which would increase the core self-emission relative to the 1-D prediction by an uncertain factor. The unablated CD remnant is indicated in the simulated mass-density profiles, and its presence accounts for the sharp limb-darkened feature on the simulated transmission profile, which is particularly distinct at the later two times. The generally flat appearance of the shadow in the radiographs in Figs. 123.32(a), 123.34(a), and 123.34(b) suggests that the radial opacity profile is distinctly weighted toward the exterior, which is borne out in the more thorough analysis summarized in Fig. 123.35. The presence of unablated CD compromises the analysis of the radiograph in terms of the opacity of pure D_2, even if the amount of CD involved is of minor hydrodynamic significance. In another shot, a slight reduction in the initial CD thickness produces an imploded shell where the CD is predicted to be completely ablated away, providing a case that is potentially much better suited for this kind of analysis.

This analysis of the radiograph of shot 54395 has been repeated for shot 55133 and is shown in Fig. 123.36. The polymer shell of this target was 9.6 μm thick, initially, which was sufficiently reduced from the 10.1-μm shell thickness of shot 54395 that no polymer remains in the unablated shell in the *LILAC* simulation. As expected, the radiograph, included in Fig. 123.36 as an inset, shows no apparent self-emission at its outer edge, indicating that there is no residual polymer. Plots (a) and (b) both show the same circularly averaged radial transmission profile and the mass-density profile that was recovered from it by Abel inversion. The inferred density profile, normalized to the simulated imploded mass of 33.5 μg, has an areal density of 20 mg/cm^2, much lower than the value based on the opacity, 56 g/cm^2. In this figure, the simulated density profiles were time averaged over the 80-ps time gate of the framing camera.

The inferred mass-density profile is flatter and broader than any of the time-averaged simulated profiles. Consistent with this, the measured radiographic transmission profile is broader than the simulated radiographs at any time. Since the measured radiograph shows no sign of self-emission other than from the core, the simulated radiographs were calculated without self-emission to obtain a pure transmission signal. Consequently, the simulated and measured radiographs cannot be compared within the emitting core radius. This does not affect the inferred density profile outside the emitting core. The simulated and measured radiographs and density profiles bear

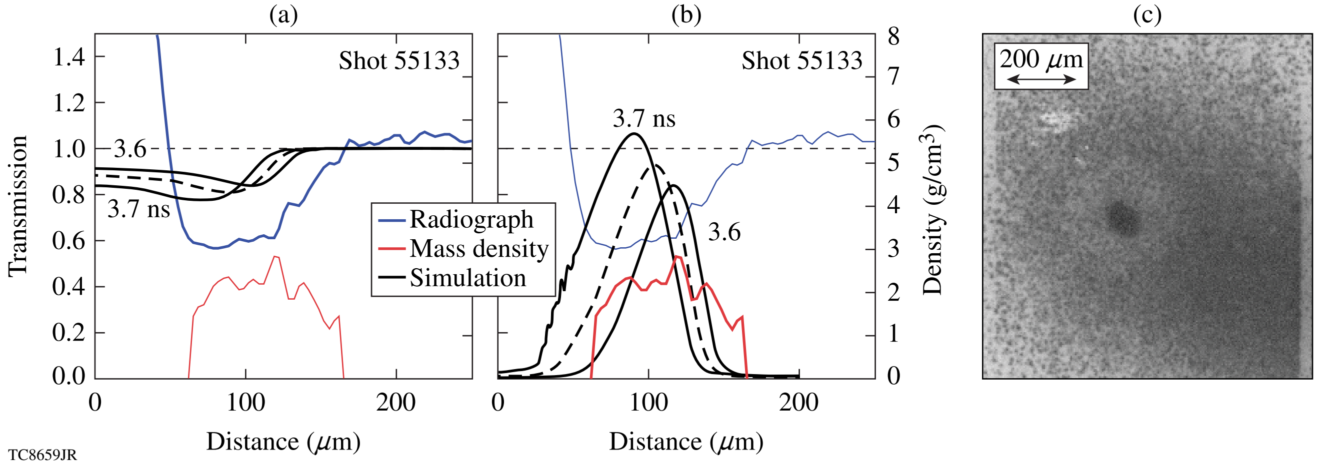

Figure 123.36
The analysis of the radiograph of shot 54395 illustrated in Fig. 123.35 is repeated here for a radiograph of shot 55133, shown in (c). This polymer shell is 9.6 μm thick, less than 10.1 μm for shot 54395. As a result, all of the polymer is expected to be ablated away, and no self-emission or absorption from unablated polymer is either expected or seen. The mass-density profile (red curve) in (b) that has been inferred from the transmission profile in (a) matches the position of the simulated shell most closely at 3.6 ns. The plotted simulated density profiles have been averaged over the 80-ps time gate of the framing camera. The areal density from the inferred mass distribution, normalized to the simulated imploded mass of 33.5 μg, is 20 mg/cm^2, much lower than the value based on the opacity, 56 mg/cm^2. The observed attenuation at this time is significantly greater than expected, as if an excess opacity were distributed uniformly over the shell.

a closer qualitative resemblance in this case than in the case of shot 45395, primarily because there is no localized external self-emission, but the measured radiographic attenuation is still greater than expected.

This unaccounted absorption remains under investigation. Small-scale mix of the shell polymer into the D_2 shell is a possibility, although an amount of carbon sufficient to diminish the transmission should be visible as self-emission at the outer surface of the shell, still warm from the ablation phase of the implosion. The D_2 opacity model must be examined. Additional BF opacity could add significantly to the opacity if the D ions are not as completely stripped by continuum lowering as the model indicates.[19]

Conclusions

Radiography of cryogenic implosions with OMEGA EP–driven backlighting is being developed on OMEGA. Analysis of the first OMEGA/OMEGA EP FF radiographs has provided useful measurements at times well in advance of peak compression. Simulated radiographs based on a multidimensional cryogenic implosion demonstrate that FF radiography at peak compression is feasible with the demonstrated backlighter intensity. Compton radiography with hard x-ray point backlighters, an alternative to radiography with soft area backlighters, has been demonstrated on OMEGA with CH implosions and is also under development for cryogenic implosion imaging on OMEGA. There is a balance of advantages between FF and Compton radiography. Compton radiographs, with simpler backlighter attenuation physics and lower background from self-emission, are easier to analyze. Simulated Compton radiographs show measurable contrast that is interpreted with simple attenuation physics with little dependence on the backlight spectrum or the target material. The strong material dependence of FF opacity can compromise the soft radiograph of a cryo shell, even if only a trace of polymer shell material mixes into the imploded ice. While the very weak material dependence of Compton scattering makes radiography of the ice shell possible in the presence of hydrodynamically irrelevant contaminants, the stronger material sensitivity of FF radiography could be useful for detecting significant contamination or mix. Not only is the radiograph contrast much stronger in FF radiography, as compared with the marginally detectable contrast in Compton radiography, but the contrast can be optimized for a particular stage in the compression history by changing the backlighter material, while in Compton radiography almost nothing can be done to improve or adjust the contrast.

With either method, backlighter sources driven by OMEGA EP will provide useful images of cryogenic shells imploded on OMEGA. The images obtained from the radiography of cryogenic implosions will be crucial for demonstrating the continuing success of cryogenic implosion campaigns by supplementing the data currently obtained. The preliminary results presented here show similarities between the simulated implosion performance and radiography well in advance of peak compression. These results are valuable and encouraging in planning for future measurements that will be extended to the final phases of the implosion.

ACKNOWLEDGMENT

This work was supported by the U.S. Department of Energy Office (DOE) of Inertial Confinement Fusion under Cooperative Agreement No. DE-FC52-08NA28302, the University of Rochester, and the New York State Energy Research and Development Authority. The support of DOE does not constitute an endorsement by DOE of the views expressed in this article.

REFERENCES

1. T. R. Boehly, D. L. Brown, R. S. Craxton, R. L. Keck, J. P. Knauer, J. H. Kelly, T. J. Kessler, S. A. Kumpan, S. J. Loucks, S. A. Letzring, F. J. Marshall, R. L. McCrory, S. F. B. Morse, W. Seka, J. M. Soures, and C. P. Verdon, Opt. Commun. **133**, 495 (1997).
2. L. J. Waxer, D. N. Maywar, J. H. Kelly, T. J. Kessler, B. E. Kruschwitz, S. J. Loucks, R. L. McCrory, D. D. Meyerhofer, S. F. B. Morse, C. Stoeckl, and J. D. Zuegel, Opt. Photonics News **16**, 30 (2005).
3. V. N. Goncharov, T. C. Sangster, T. R. Boehly, S. X. Hu, I. V. Igumenshchev, F. J. Marshall, R. L. McCrory, D. D. Meyerhofer, P. B. Radha, W. Seka, S. Skupsky, C. Stoeckl, D. T. Casey, J. A. Frenje, and R. D. Petrasso, Phys. Rev. Lett. **104**, 165001 (2010); T. C. Sangster, V. N. Goncharov, R. Betti, T. R. Boehly, D. T. Casey, T. J. B. Collins, R. S. Craxton, J. A. Delettrez, D. H. Edgell, R. Epstein, K. A. Fletcher, J. A. Frenje, V. Yu. Glebov, D. R. Harding, S. X. Hu, I. V. Igumenshchev, J. P. Knauer, S. J. Loucks, C. K. Li, J. A. Marozas, F. J. Marshall, R. L. McCrory, P. W. McKenty, D. D. Meyerhofer, P. M. Nilson, S. P. Padalino, R. D. Petrasso, P. B. Radha, S. P. Regan, F. H. Seguin, W. Seka, R. W. Short, D. Shvarts, S. Skupsky, V. A. Smalyuk, J. M. Soures, C. Stoeckl, W. Theobald, and B. Yaakobi, Phys. Plasmas **17**, 056312 (2010).
4. C. D. Zhou and R. Betti, Phys. Plasmas **14**, 072703 (2007).
5. E. I. Moses, J. Phys., Conf. Ser. **112**, 012003 (2008).
6. R. Epstein, V. A. Smalyuk, F. J. Marshall, J. Delettrez, V. N. Goncharov, P. W. McKenty, D. D. Meyerhofer, P. B. Radha, S. P. Regan, T. C. Sangster, and W. Theobald, Bull. Am. Phys. Soc. **54**, 306 (2009).
7. F. J. Marshall, P. W. McKenty, J. A. Delettrez, R. Epstein, J. P. Knauer, V. A. Smalyuk, J. A. Frenje, C. K. Li, R. D. Petrasso, F. H. Séguin, and R. C. Mancini, Phys. Rev. Lett. **102**, 185004 (2009).
8. R. Tommasini *et al.*, Rev. Sci. Instrum. **79**, 10E901 (2008).
9. *LLE Review Quarterly Report* **120**, 239, Laboratory for Laser Energetics, University of Rochester, Rochester, NY, LLE Document No. DOE/NA/28302-910 (2009).
10. D. K. Bradley *et al.*, Rev. Sci. Instrum. **66**, 716 (1995).
11. S. Regan (Laboratory for Laser Energetics) and R. Tommasini (Lawrence Livermore National Laboratory), private communication (2009).
12. S. Chandrasekhar, *Plasma Physics* (University of Chicago Press, Chicago, 1960).
13. R. N. Bracewell, *The Fourier Transform and Its Applications*, 3rd ed. (McGraw-Hill, Boston, 2000).
14. E. Sergrè, *Nuclei and Particles: An Introduction to Nuclear and Subnuclear Physics* (W. A. Benjamin, New York, 1965).
15. J. Castor, *Radiation Hydrodynamics* (Cambridge University Press, Cambridge, England, 2004), pp. 291–293.
16. J. D. Lindl, Phys. Plasmas **2**, 3933 (1995).
17. J. Delettrez, R. Epstein, M. C. Richardson, P. A. Jaanimagi, and B. L. Henke, Phys. Rev. A **36**, 3926 (1987).
18. P. B. Radha, V. N. Goncharov, T. J. B. Collins, J. A. Delettrez, Y. Elbaz, V. Yu. Glebov, R. L. Keck, D. E. Keller, J. P. Knauer, J. A. Marozas, F. J. Marshall, P. W. McKenty, D. D. Meyerhofer, S. P. Regan, T. C. Sangster, D. Shvarts, S. Skupsky, Y. Srebro, R. P. J. Town, and C. Stoeckl, Phys. Plasmas **12**, 032702 (2005).
19. J. J. MacFarlane *et al.*, High Energy Density Phys. **3**, 181 (2006).
20. T. C. Sangster, V. N. Goncharov, P. B. Radha, V. A. Smalyuk, R. Betti, R. S. Craxton, J. A. Delettrez, D. H. Edgell, V. Yu. Glebov, D. R. Harding, D. Jacobs-Perkins, J. P. Knauer, F. J. Marshall, R. L. McCrory, P. W. McKenty, D. D. Meyerhofer, S. P. Regan, W. Seka, R. W. Short, S. Skupsky, J. M. Soures, C. Stoeckl, B. Yaakobi, D. Shvarts, J. A. Frenje, C. K. Li, R. D. Petrasso, and F. H. Séguin, Phys. Rev. Lett. **100**, 185006 (2008).
21. W. Theobald, C. Stoeckl, P. A. Jaanimagi, P. M. Nilson, M. Storm, D. D. Meyerhofer, T. C. Sangster, D. Hey, A. J. MacKinnon, H.-S. Park, P. K. Patel, R. Shephard, R. A. Snavely, M. H. Key, J. A. King, B. Zhang, R. B. Stephens, K. U. Akli, K. Highbarger, R. L. Daskalova, L. Van Woerkom, R. R. Freeman, J. S. Green, G. Gregori, K. Lancaster, and P. A. Norreys, Rev. Sci. Instrum. **80**, 083501 (2009).

A Gated Liquid-Scintillator–Based Neutron Detector for Fast-Ignitor Experiments and Down-Scattered Neutron Measurements

Introduction

Neutron detectors in inertial confinement fusion experiments are predominantly used to measure the neutron yield[1] and ion temperature[2] of the primary fusion reaction. These experiments produce nearly monoenergetic neutron spectra with energies of ~2.45 MeV for deuterium–deuterium (D–D) reactions and 14.1 MeV for deuterium–tritium (DT)–filled targets. The neutron spectra are broadened only slightly by the temperature of the core plasma,[2] which is of the order of a few keV. Neutron detectors are also utilized to detect secondary DT neutrons from targets filled with pure deuterium to infer the areal density of the fuel.[3] The secondary DT neutrons show a broad spectrum that depends on the fuel areal density, typically from 10 to 18 MeV, with a yield of the order of 10^{-3} of the primary neutrons. Since these secondary DT neutrons are faster than the primary DD neutrons, they can be easily detected with a time-resolved detector at a sufficient distance from the target to allow for neutron time-of-flight dispersion, which is of the order of ~25 ns/m. Even though the large background from the primary neutrons generally saturates the detector and recording system, this does not significantly affect the secondary neutron measurements because the secondary neutrons are recorded well before the background arrives. Recently, two new applications for neutron detectors have been proposed: (1) fast-ignition (FI) experiments with cone-in-shell targets[4] and (2) down-scattered neutron measurements in inertial fusion experiments,[5] which are much more challenging since they require the measurement of a small signal after a large background. In FI experiments the neutron spectrum of interest is quasi-monoenergetic, generally at ~2.45 MeV from D–D reactions. The background consists of hard x rays from the interaction of the high-energy short-pulse laser with the gold cones with an apparent spectral temperature of the order of ~1 MeV. The temporal dispersion between signal and background is high (~40 ns/m), but the background can easily be 10^5 times higher than the signal. For the down-scattered neutron measurements, the background is the primary DT neutrons and the signal is the neutrons with energies below 12 MeV, typically 6 to 10 MeV. The signal-to-background ratio depends on the areal density of the target and is of the order of 10^{-2} for full-scale ignition targets. The temporal time-of-flight dispersion is small, approximately 4 ns/m for 10-MeV neutrons, compared to the primary 14.1-MeV DT neutrons. This article describes a current-mode neutron detector developed at LLE using a fast oxygen-enriched liquid scintillator coupled to a gated microchannel plate photomultiplier for FI and down-scattered neutron measurements.

X-Ray Shielding

While shielding cannot be used for down-scattered neutron measurements to separate signal from background since there is no significant attenuation difference between 14.1-MeV and 6- to 12-MeV neutrons in any material, x-ray shielding has been used successfully to measure neutrons in high-energy short-pulse laser experiments at ~500-J laser energy and 1-ps pulse duration.[6] The detector described in Ref. 6 [an 18-cm-diam, 10-cm-thick Pilot B[7] scintillator, coupled to a conventional XP2020[8] photomultiplier tube (PMT)] was set up 2 m from the target for integrated FI experiments on the OMEGA Laser System.[9] Lead shielding with 15-cm thickness toward the target and 5 cm in all other directions was used to attenuate the hard x-ray background [see Fig. 123.37(a)]. The expected neutron yield from the FI experiments are of the order of 10^7, which would produce a signal of ~1 V in the PMT. Figure 123.37(b) shows an example from a neutron-producing shot with a yield of 1.1×10^7 without the short-pulse laser firing. In an integrated FI experiment with a short-pulse laser energy of 1 kJ at 10 ps, the PMT is heavily saturated and no neutron signal is visible at all [Fig. 123.37(c)]. An additional factor of 1000 of x-ray attenuation is a rough estimate of what would be required to avoid saturation. The attenuation coefficients for Pb at photon energies of 2 to 10 MeV can be obtained from the NIST, XCOM[10] database to be ~4 to 5×10^{-2} cm^2/g, which translates into a 1/*e* attenuation length of ~2 cm. Therefore an additional ~15 cm of Pb shielding would be required to avoid saturation. The total neutron-scattering cross section at 2.45 MeV is approximately 7 barn for Pb, according to the LBL, ENDF[11] database, which translates into a 1/*e* attenuation length of ~4 cm. Consequently, the neutron signal would also be attenuated by approximately

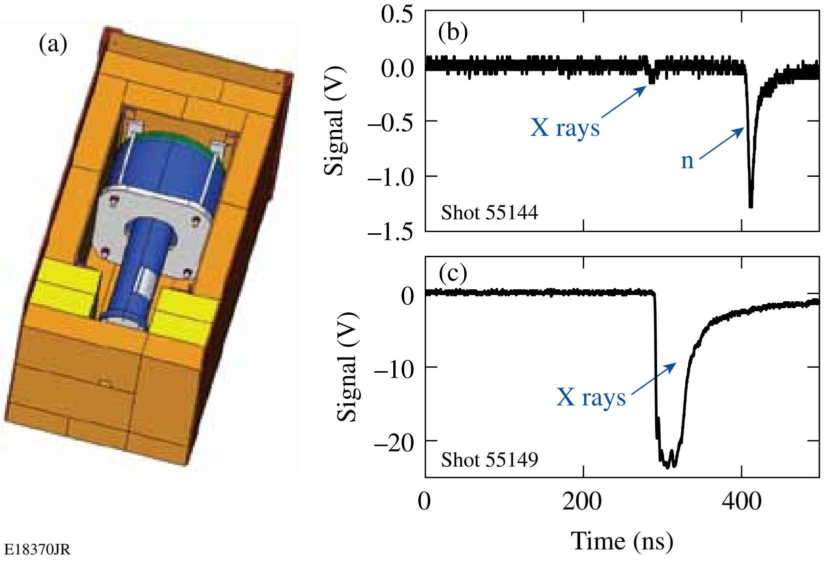

Figure 123.37
(a) CAD model of the detector shielding. (b) Neutron signal from a shot with a yield of 1.1 × 10^7. (c) X-ray background from a 1-kJ, 10-ps short pulse interacting with a fast-ignition target.

a factor of 50 and significantly broadened in time because of multiple scattering in the Pb shielding, making it almost impossible to detect.

Photomultiplier Gating

Another method to suppress the background signal, which works for both the FI experiments and the down-scattered neutron measurements, is to gate the PMT, rendering it inactive when the background signal is present. A PMT can be gated by applying a short positive pulse of the order of 200 V to the photocathode, which extracts the photoelectrons from the photocathode and prevents them from reaching the microchannel plate (see Fig. 123.38). A gated PMT240 from PHOTEK[12] was used in the NIF neutron time-of-flight (nTOF) detector, as described in Ref. 13, for FI experiments. The PMT was operated at a gain of 10^6 coupled to a 40-mm-diam, 20-mm-thick BC422[14] plastic scintillator shielded with 25 mm of Pb. The detector was placed 5.2 m from the target. The gating pulse was set up to eliminate the hard x-ray pulse from the short-pulse interaction, which is recorded at ~350 ns (see Fig. 123.39). Up to an energy of ~500 J, the PMT gating reduces the pulse significantly, but at ~800 J of short-pulse energy the gating ceases to be effective and the PMT is saturated.

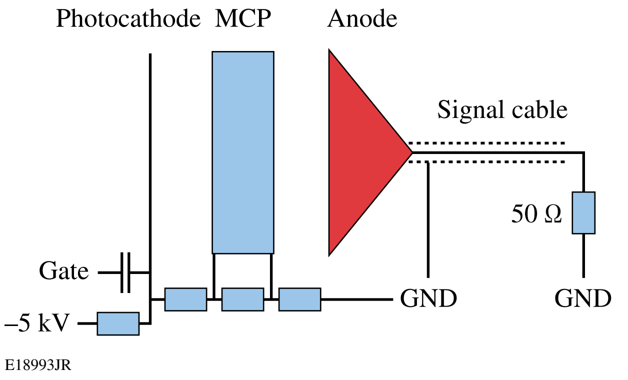

Figure 123.38
Simplified electrical schematic of the photomultiplier gating circuit. A resistive divider sets up the voltages between the photocathode, microchannel plate (MCP), and anode. A positive pulse at the gate input extracts the photoelectrons, disabling the photomultiplier tube (PMT).

By removing the scintillator, it was verified that the background signal is produced predominantly by interactions with the microchannel plate (MCP). Since the MCP voltage is almost unchanged by the gate pulse, electrons generated inside the MCP will be amplified and a signal will be recorded, even if the gate voltage is applied. To avoid saturation from direct interaction with the MCP, a neutron detector was set up below the 60-cm-thick concrete floor below the target chamber at 12.4 m from the target [see Fig. 123.40(a)]. A 20-cm-diam hole in the floor provided an unshielded line of sight from the target to the detector. The gated PMT240 was mounted ~20 cm from the scintillator outside the direct line of sight through the hole. To compensate for the larger distance to target and the reduced light-collection efficiency, the scintillator size was increased to 18-cm diameter × 10-cm thickness.

A 2.5-cm-thick lead x-ray shield covering the hole in the floor eliminates the x-ray background with energies <1 MeV. In this configuration the PMT gating works well and the background is reduced to a very low level, as seen in Fig. 123.40(b). Unfortunately the light output from the plastic scintillator has a significant component with a long decay constant, which produces a strong background once the PMT gate ends. This

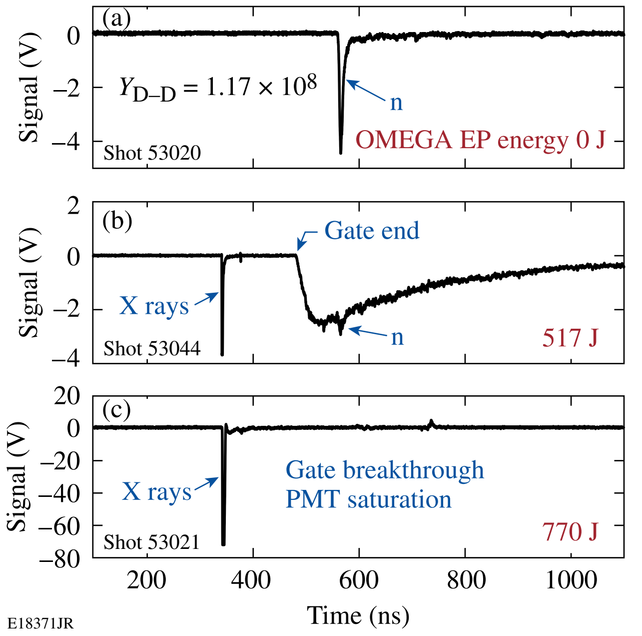

Figure 123.39
Signal from gated PMT in NIF nTOF detector: (a) no short pulse, (b) short-pulse energy of 517 J, and (c) short-pulse energy of 770 J.

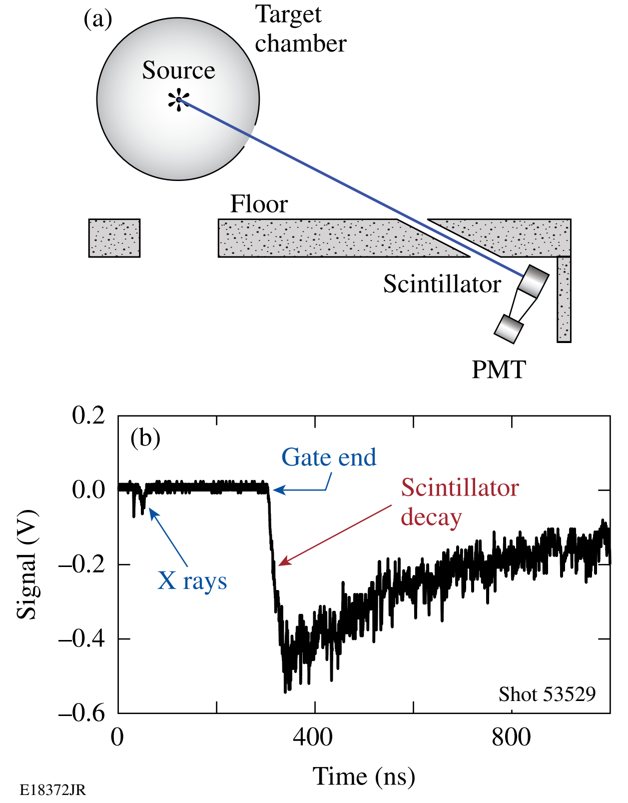

Figure 123.40
(a) Setup used to shield the PMT from direct hard x-ray irradiation; (b) signal from 1-kJ fast-ignition shot.

scintillator afterglow completely masks any neutron signal from D–D fusion reactions, which is expected to appear at ~550 ns, given the time-of-flight distance.

Oxygen-Enriched Liquid Scintillator

To avoid background from the scintillator decay, a scintillator material with a significantly reduced long-decay component is required. Recently a low-afterglow liquid scintillator described in the literature showed a >100× decreased light output for times >100 ns after the primary event.[15] This liquid scintillator is based on a mixture of two dyes, PPO and bis-MSB, dissolved in xylene and enriched with molecular O_2. A neutron detector using this scintillator material was set up using the line of sight below the concrete floor shown in Fig. 123.40. It consists of a 3-L volume of oxygen-enriched liquid scintillator coupled to a gated PMT240 (see Fig. 123.41). A small air bubble allows for thermal expansion of the liquid without a significant pressure increase. The PMT is placed outside the direct line of sight to the target to avoid direct x-ray interactions with the MCP [see (Fig. 123.40)]. Data from integrated FI experiments with 1 kJ of short-pulse energy show a dramatically reduced scintillator decay tail and a very clear D–D neutron signal at the expected time [see Fig. 123.42(a)]. A very similar detector with a slightly smaller scintillator volume of ~1 L was fielded on high-areal-density cryogenic D–T implosions,[16] for down-scattered neutron measurements. The gating of the D–T primary peak works quite well, and the 2.45-MeV D–D fusion neutron peak is very well resolved [see Fig. 123.42(b)]. Unfortunately, a large background can still be seen in the signal after the gate turns off and the PMT becomes active. This background is predominantly caused by scattered primary DT neutrons that enter the room under the target area through

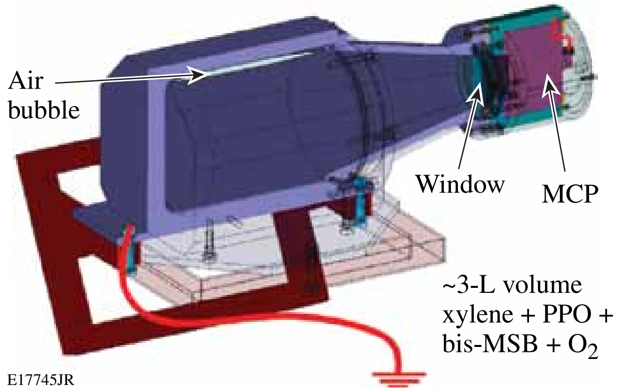

Figure 123.41
Drawing of the liquid scintillator detector.

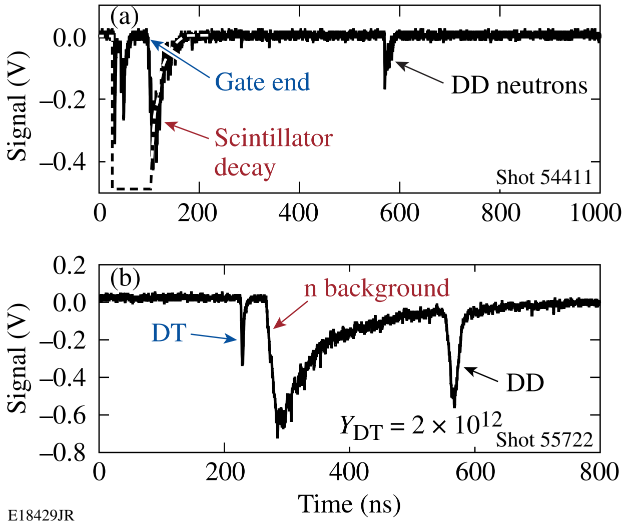

Figure 123.42
Signals recorded from the oxygen-enriched scintillator detector: (a) from FI experiments with 1 kJ of short-pulse energy and (b) high-areal-density cryogenic implosions.

a large hole under the target chamber and reach the detector through a large number of different pathways at different times. This was verified by blocking the direct line of sight to the target, resulting in a very similar background signal, without either the primary D–T or D–D peak.

Summary and Conclusions

The detection of a small neutron signal after a very large background of hard x rays from short-pulse-laser–target interactions in a FI experiment or neutrons of higher energy in down-scattered neutron measurements is a very challenging task. Only the proper combination of sophisticated shielding, gating of a fast MCP-PMT, and a low-afterglow scintillator made it possible to record the D–D thermal neutron peak in integrated FI experiments at 1 kJ of short-pulse energy. In experiments with high-areal-density cryogenic DT targets, it was possible to clearly observe the D–D neutron peak, but the smaller down-scattered neutron signal is still masked by scattered primary neutrons that reach the detector because of insufficient neutron shielding. An improved neutron shielding for down-scattered neutron measurements on OMEGA is currently being designed and will be fielded in the near future.

ACKNOWLEDGMENT

This work was supported by the U.S. Department of Energy Office of Inertial Confinement Fusion under Cooperative Agreement No. DE-FC52-08NA28302, the University of Rochester, and the New York State Energy Research and Development Authority. The support of DOE does not constitute an endorsement by DOE of the views expressed in this article.

REFERENCES

1. M. D. Cable and M. B. Nelson, Rev. Sci. Instrum. **59**, 1738 (1988).
2. T. J. Murphy, R. E. Chrien, and K. A. Klare, Rev. Sci. Instrum. **68**, 610 (1997).
3. V. Yu. Glebov, D. D. Meyerhofer, C. Stoeckl, and J. D. Zuegel, Rev. Sci. Instrum. **72**, 824 (2001).
4. R. Kodama *et al.*, Nature **418**, 933 (2002).
5. V. Yu. Glebov, D. D. Meyerhofer, T. C. Sangster, C. Stoeckl, S. Roberts, C. A. Barrera, J. R. Celeste, C. J. Cerjan, L. S. Dauffy, D. C. Eder, R. L. Griffith, S. W. Haan, B. A. Hammel, S. P. Hatchett, N. Izumi, J. R. Kimbrough, J. A. Koch, O. L. Landen, R. A. Lerche, B. J. MacGowan, M. J. Moran, E. W. Ng, T. W. Phillips, P. M. Song, R. Tommasini, B. K. Young, S. E. Caldwell, G. P. Grim, S. C. Evans, J. M. Mack, T. Sedillo, M. D. Wilke, D. C. Wilson, C. S. Young, D. Casey, J. A. Frenje, C. K. Li, R. D. Petrasso, F. H. Séguin, J. L. Bourgade, L. Disdier, M. Houry, I. Lantuejoul, O. Landoas, G. A. Chandler, G. W. Cooper, R. J. Lepeer, R. E. Olson, C. L. Ruiz, M. A. Sweeney, S. P. Padalino, C. Horsfield, and B. A. Davis, Rev. Sci. Instrum. **77**, 10E715 (2006).
6. C. Stoeckl, V. Yu. Glebov, P. A. Jaanimagi, D. D. Meyerhofer, T. C. Sangster, M. Storm, S. Sublett, W. Theobald, M. H. Key, A. J. MacKinnon, P. Patel, P. A. Norreys, and D. Neely, Rev. Sci. Instrum. **77**, 10F506 (2006).
7. Nuclear Enterprises Ltd., Edinburgh, Midlothian EH11 4BY, United Kingdom.
8. Koninklijke Philips Electronics N.V., 1070 Amsterdam, The Netherlands.
9. C. Stoeckl, J. A. Delettrez, J. H. Kelly, T. J. Kessler, B. E. Kruschwitz, S. J. Loucks, R. L. McCrory, D. D. Meyerhofer, D. N. Maywar, S. F. B. Morse, J. Myatt, A. L. Rigatti, L. J. Waxer, J. D. Zuegel, and R. B. Stephens, Fusion Sci. Technol. **49**, 367 (2006).
10. Physics Laboratory, National Institute of Standards and Technology (NIST), http://www.nist.gov/physlab/index.cfm.
11. Experimental Nuclear Reaction Data (EXFOR/CSISRS), http://www.nndc.bnl.gov/exfor/.
12. Photek Ltd., St. Leonards-on-Sea, East Sussex, TN38 9NS, United Kingdom.
13. Z. A. Ali, V. Yu. Glebov, M. Cruz, T. Duffy, C. Stoeckl, S. Roberts, T. C. Sangster, R. Tommasini, A. Throop, M. Moran, L. Dauffy, and C. Horsefield, Rev. Sci. Instrum. **79**, 10E527 (2008).
14. Saint-Gobain Cristaux & Detecteurs, 38910 Gieres, France.
15. R. Lauck *et al.*, IEEE Trans. Nucl. Sci. **56**, 989 (2009).
16. V. N. Goncharov, T. C. Sangster, T. R. Boehly, S. X. Hu, I. V. Igumenshchev, F. J. Marshall, R. L. McCrory, D. D. Meyerhofer, P. B. Radha, W. Seka, S. Skupsky, C. Stoeckl, D. T. Casey, J. A. Frenje, and R. D. Petrasso, Phys. Rev. Lett. **104**, 165001 (2010).

On-Chip Double Emulsion Droplet Assembly for Laser-Target Fabrication

Introduction

Inertial confinement fusion (ICF) experiments use spherical organic polymer shells as mandrels for cryogenic foam targets. The targets are typically fabricated by polymerizing double-emulsion (DE) shells and then voiding the inner fluids.[1,2] In this process, special care must be taken to ensure DE droplet uniformity because fusion experiments impose rigid requirements on the sphericity and wall thickness uniformity of foam targets.

Up to the present, the formation of uniform DE droplets has relied mainly on the controlled merging of two immiscible fluids.[1–5] DE droplets for target fabrication are currently prepared using a triple-orifice droplet generator.[1] This method generates remarkably monodisperse emulsions with good uniformity. The DE droplet size, however, is constrained by the device dimensions, and the microfluidic devices need to be recalibrated and tuned to the correct dimensions each time they are used. In this article, we propose a DE assembly line based on a "lab-on-a-chip" droplet generator, where individual water and oil droplets generated from an on-chip dispensing system are combined directly to form DE's. As a droplet-based microfluidic system, this scheme has the advantages of reconfigurability, flexibility, and scalability.

Background

Because the formation of DE droplets in air requires combining at least one aqueous (water) and one non-aqueous (oil) liquid droplet, we use electrowetting-on-dielectric (EWOD) and dielectrophoresis (DEP) simultaneously to dispense and transport water and oil droplets, respectively. Because all actuation is electrical, we can program each step and, in this way, obtain maximum operational flexibility.

1. Electrowetting-on-Dielectric (EWOD)

The electrowetting effect describes the observable influence of an electric field on both bulk liquid motions and the contact angle. The motive force is due to the response of the free electric surface charge to the electric field.[6,7] In an EWOD-based microfluidic device as shown in Fig. 123.43, droplets are sandwiched between parallel plates and manipulated by applying voltages to a series of adjacent electrodes on the bottom. A wide variety of fundamental fluid operations have been realized using EWOD. These operations include droplet transport,[8] dispensing,[9–11] separation,[9,11] coalescence,[9] dilution,[12] and others.

2. Dielectrophoresis (DEP)

The dielectrophoretic (or DEP) force is the force exerted on dielectrics when subjected to a nonuniform electric field.[13,14] As another extensively studied mechanism for droplet manipulation, DEP is useful for manipulating insulating, polarizable media. For example, decane cannot be moved by EWOD[15] but can be moved by DEP.[16]

EWOD and DEP are two observable effects of liquid under electrostatic fields, both of which are electromechanical in nature. Jones[7] first clarified the frequency-dependent relationship between these two mechanisms. For a liquid with finite electrical conductivity and dielectric constant, there exists a critical frequency that separates conductive (EWOD) and dielectric (DEP) behavior.[7,17,18] In the high-frequency limit, the liquid behaves as an insulator so that the electric field penetrates it. As a result, the observable electromechanical response of the liquid is virtually identical to liquid DEP.

3. General Microfluidic Platform Based on EWOD and DEP

The combination of droplet-based EWOD and DEP microfluidics makes it possible to manipulate both conductive and insulating droplets on the same chip. Conceptually, such a combination of EWOD and DEP may be visualized with the parallel-plate scheme shown in Fig. 123.43. The device consists of two parallel glass plates: a bottom plate that consists of a patterned array of individually addressable electrodes, and a top plate that is a continuous ground electrode. Usually the bottom plate is coated with a dielectric layer, and both the top and bottom surfaces are covered with a thin hydrophobic film to decrease the surface wettability.

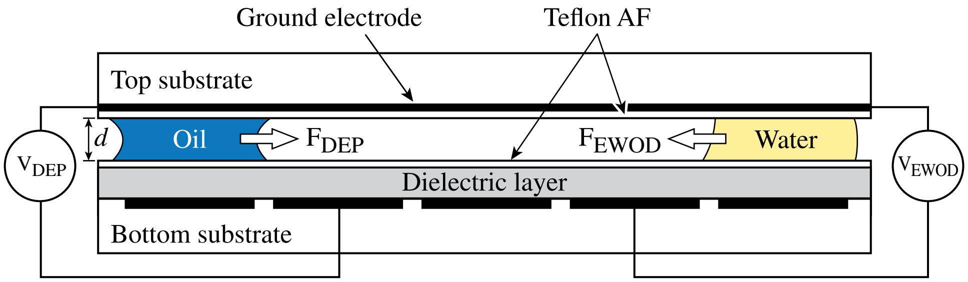

E18697JR

Figure 123.43
Cross section of a parallel-plate device containing a dielectric layer on the bottom plate to manipulate oil and water droplets by DEP and EWOD, respectively.

Microfabrication and Experiments

The basic features of the droplet-based microfluidic system are illustrated in a cross-sectional view in Fig. 123.43. The bottom glass substrate is evaporatively coated with 100 nm of aluminum and then photolithographically patterned into a two-dimensional electrode array. The structure is then spin coated with 0.5 μm of spin-on-glass (SOG) (Futurrex IC1-200) as the dielectric layer and 1 μm of amorphous fluoropolymer (DuPont Teflon-AF) as a hydrophobic coating. The top plate is a glass plate with a transparent indium tin oxide layer as a ground electrode covered by 1 μm of Teflon-AF as a hydrophobic coating.

The top substrate is positioned above the bottom substrate by appropriate spacers. Voltages applied to individual electrodes are controlled by a LabView-based controller. It is important to recognize that different voltages are applied for EWOD actuation and DEP actuation. For EWOD actuation, dc or low-frequency ac voltage, typically <100 V, is employed. For oil DEP actuation, dc or ac voltage (50 to 100K Hz) is used, but usually >250 V.

Droplet-Dispensing Reproducibility

In a typical dispensing operation, a liquid finger is drawn from a large reservoir droplet. Liquid pinch-off occurs by activating the electrode at the front end of the liquid finger and the reservoir electrode and deactivating the electrodes in between (the cutting electrode) until the liquid front is separated from the liquid bulk. Successful pinch-off requires an application of electrode voltages above some threshold value.[6] The sequence of steps of droplet dispensing is shown in Fig. 123.44. EWOD-based water droplet dispensing has been widely studied,[9–11] but dielectric-droplet (oil) dispensing has not received much attention. Here we demonstrate repeatable dielectric droplet dispensing on a microfluidic chip as shown in Fig. 123.44. Because of the difference in the electric-actuation mechanism, oil-droplet manipulation by DEP requires much higher voltages than EWOD dispensing of aqueous droplets.

Dispensing reproducibility is of paramount importance in laser-target fabrication because the uniformity of subsequently formed DE droplets is largely determined by the initial liquid volume control. The requirements for double emulsion droplet uniformity are described in **Appendix A** (p. 156). It has been observed that the final extracted drop volume is usually somewhat larger than the volume subtended by a square electrode (volume = a^2d, where a is the length of a square electrode in the electrode array and d is the spacing between bottom and top substrates).[11] The reason is that a liquid tail formed after separation adds some additional liquid to the already-formed

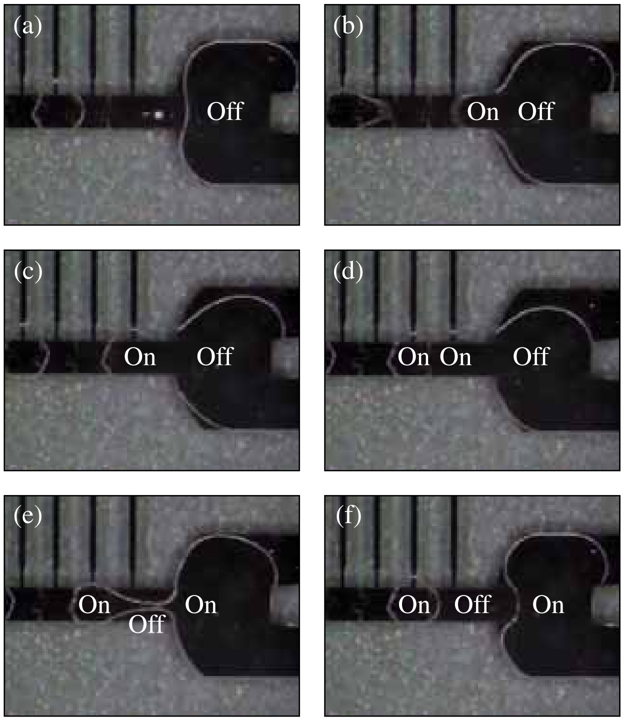

E19065JR

Figure 123.44
Top view of an on-chip dispenser showing the sequence of a silicone oil droplet being formed. (a) The reservoir and an already-formed droplet; (b)–(d) the liquid finger is formed, and, meanwhile, the first droplet is delivered away; (e) the pinch-off occurs; (f) a new droplet is formed.

droplet. It is this volume that produces variability in the dispensing operation. In this research we investigated the effects of applied voltage and electrode shape on droplet volume control for an on-chip dispensing system because they both impact the tail volume directly.

1. Effect of Applied Voltage on Droplet Volume Variations

We investigated the dependence of dispensed water drop volume on the actuation voltage in a structure with 1-mm-sq electrodes. The droplet volume becomes sensitive when the applied voltage is close to the minimum required value for pinch-off. For example, when applied voltage decreased from 62.5 V to the minimum pinch-off voltage of 55.0 V, the droplet volume dropped by almost 30% as shown in Fig. 123.45. The same result is observed with both square and circular dispensing electrodes. The voltage effect is a result of the effect on the tail shapes during pinch-off. As shown in Fig. 123.46, a smaller tail is observed at lower voltage, and the pinch-off position also moves closer to the individual droplet. The shape of the tail changes because the liquid finger necking depends on the electrowetting force, which is directly related to applied voltage.[6]

Figures 123.46(c) and 123.46(e) show that with square electrodes, a smaller area of the dispensing electrode is filled by liquid during pinch-off at lower voltage. This smaller finger front may also contribute to reduced dispensed-droplet volume. No obvious change in the finger front is observed for circular electrode structures, as shown in Figs. 123.46(g) and 123.46(i), but the droplet volume remains very sensitive to voltage change. In general, the tail volume plays the most important role in determining variation in droplet volume.

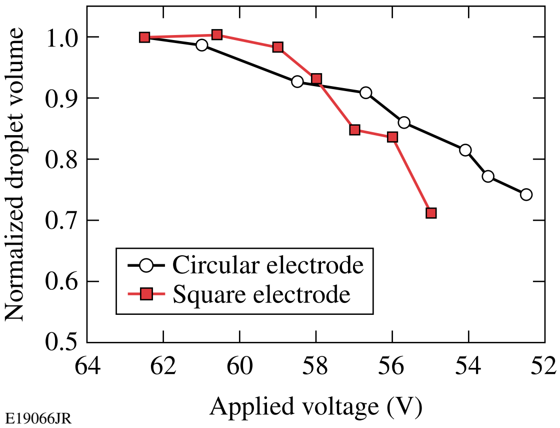

Figure 123.45
The normalized volume variation of a series of droplets generated by different applied voltages. All tests were done with DI water. The gap between the top and bottom substrates was 85 μm, and the voltage applied was 100 Hz ac.

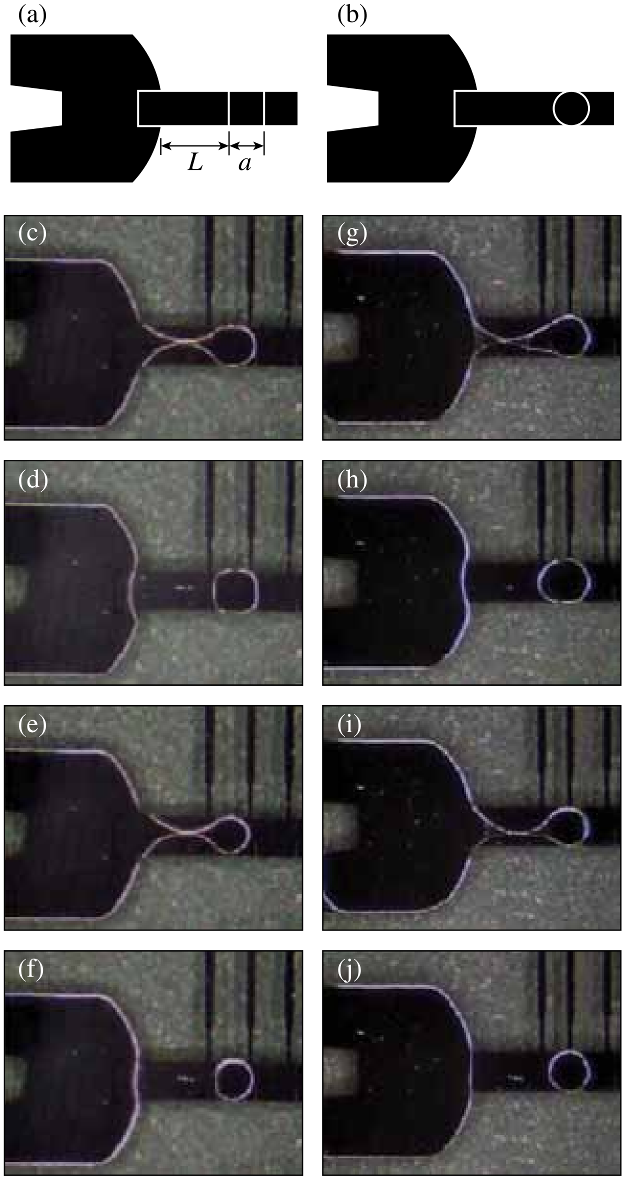

Figure 123.46
The effect of applied voltage on droplet volume variation. [(a),(b)] Square and circular dispensing electrodes used for the dispensing experiments. The square electrode is 1 mm × 1 mm and the diameter of the circular electrode is 1 mm. The length of the cutting electrode is 2 mm. [(c),(d)] Pinch-off and the formed droplet on the square electrode by applying 62.5-V_{rms}, 100-Hz ac voltage; [(e),(f)] pinch-off and the formed droplet on the square electrode by applying 55-V_{rms}, 100-Hz ac voltage; [(g),(h)] pinch-off and the formed droplet on the circular electrode by applying 62.5-V_{rms}, 100-Hz ac voltage; [(i),(j)] pinch-off and the formed droplet on the circular electrode by applying 52.5-V_{rms}, 100-Hz ac voltage. In all cases, the gap between top and bottom substrates is 85 μm.

2. Effect of Cutting Electrode on Droplet Volume and Reproducibility

We tested electrode structures with different cutting electrode length (*L*) to investigate its effect on droplet volume and reproducibility. As shown in Fig. 123.47, the dispensed droplet volume increases directly with *L*. Droplets with an average volume of 103 nL and 183 nL were dispensed on a 1-mm × 1-mm-sq electrode using cutting electrodes of lengths $L = 2$ mm and 3 mm, respectively. These droplet volumes are greater than the volume subtended by one electrode (85 nL). The increase in droplet volume is due to the larger tail formed on longer cutting electrodes during pinch-off. Similar behavior is also observed on 2-mm × 2-mm-sq electrodes.

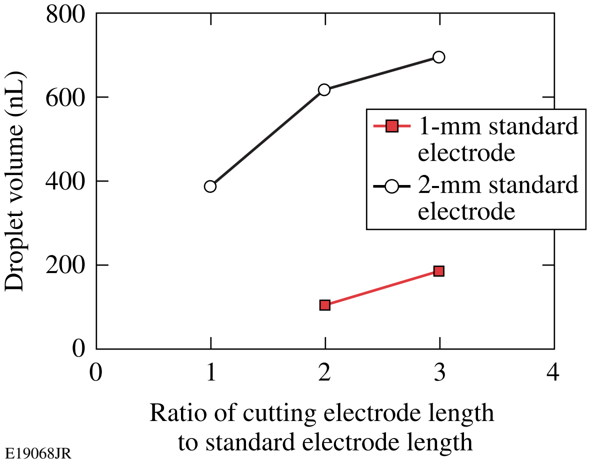

Figure 123.47
Average droplet volume versus cutting electrode length. All tests were performed with DI water. The gap between top and bottom substrates was 85 μm, and 90-V_{rms}, 100-Hz ac voltage was applied.

Droplet volume reproducibility suffers as *L* is increased. As indicated in Fig. 123.48 and Table 123.V, the coefficient of variation (CV = standard deviation/mean) increases significantly when the ratio of the cutting electrode length to standard electrode length (*L*/*a*) approaches $L/a = 3$. The reason for this behavior is the reduced influence of the cutting electrode on the radius of curvature in the pinch-off region. In fact, the pinch-off position becomes indeterminate for sufficiently large *L*/*a*. Large droplet volume variation (CV = 40%) is observed when $L/a = 3$ on a 2-mm × 2-mm electrode because of the instability of the pinch-off position (see Fig. 123.49).

The best reproducibility (CV = 3.0%) is achieved for a cutting electrode of the same length as that of the standard electrodes. This reproducibility is adequate for laser target fabrication (see **Appendix A**, p. 156, for detailed discussion).

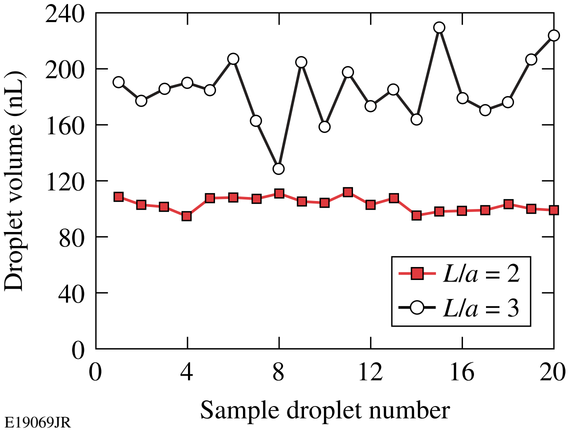

Figure 123.48
Droplet volume variation for two lengths of the cutting electrode. All tests were performed with DI water on 1-mm × 1-mm dispensing electrodes. The gap between the top and bottom substrates was 85 μm, and 90-V_{rms}, 100-Hz ac voltage was applied.

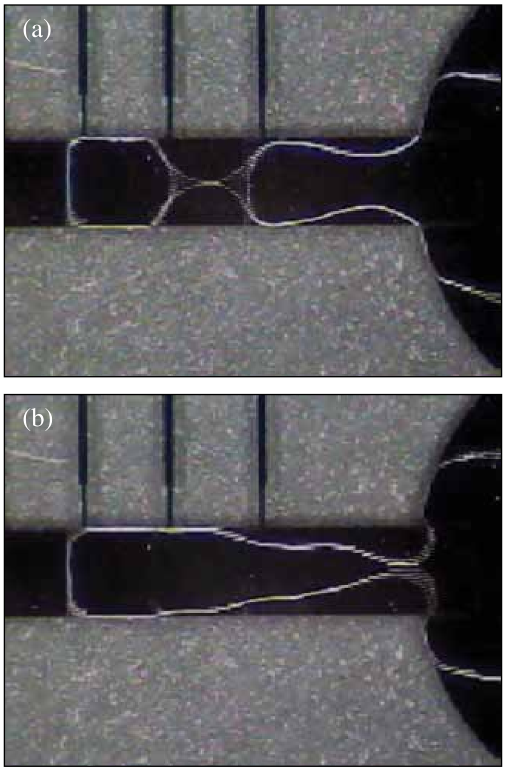

Figure 123.49
Instability of the pinch-off position for a droplet dispensing on a 2-mm standard electrode and a 6-mm cutting electrode. The gap between the top and bottom substrates was 85 μm, and 90-V_{rms}, 100-Hz ac voltage was applied.

Table 123.V: Effect of cutting electrode length on volume reproducibility (CV) for droplets dispensed on 1-mm and 2-mm dispensing electrodes and an 85-μm channel gap. In all cases, the voltage applied was 90 V_{rms}, 100 Hz ac.

Electrode size	*L*/*a* = 1	*L*/*a* = 2	*L*/*a* = 3
1 mm × 1 mm	—	4.7%	12.7%
2 mm × 2 mm	3.0%	5.3%	40%

On-Chip Double Emulsion Formation

1. Gibbs Free Energy Model

When two immiscible droplets are brought together, a DE droplet forms spontaneously if the Gibbs free energy is reduced by the emulsification process. The Gibbs surface energy change between initial and final states of a DE formation process is

$$\Delta \mathrm{G} = \mathrm{G}_{\mathrm{DE}} - \left(\mathrm{G}_{\mathrm{water}} + \mathrm{G}_{\mathrm{oil}}\right), \tag{1}$$

where G_{DE} is the total Gibbs interfacial energy of a DE droplet and $\mathrm{G}_{\mathrm{water}}$ and $\mathrm{G}_{\mathrm{oil}}$ are Gibbs surface energies of the individual water and oil droplets forming that DE droplet. The Gibbs energy change ΔG is a convenient criterion for testing the likelihood of DE formation. A negative ΔG means the DE formation is favored. In the following, we develop a simple model to calculate the Gibbs surface energy changes associated with double emulsion formation.

The Gibbs surface energy is a sum of the product of interfacial tensions and corresponding surface areas. The surface shape of a droplet sandwiched between parallel plates is strongly affected by the contact angle against the substrate and the spacing between top and bottom substrates. For the geometry model shown in Fig. 123.50, the droplet volume is

$$\begin{aligned} V &= 2\int_0^h \pi x^2 \mathrm{d}z \\ &= 2\pi\left[\left(x_0^2 + R^2\right)h - \frac{1}{3}h^3 + 2x_0R^2\left(\frac{1}{2}\theta_0 + \frac{1}{4}\sin 2\theta_0\right)\right], \end{aligned} \tag{2}$$

where the spacing between substrates is 2 *h*, $\theta_0 = \theta - \pi/2$, θ is the contact angle on a hydrophobic surface ($\theta > 90°$), and $R = -h/\cos\theta$.

The lateral surface area and base areas are then

$$\begin{aligned} S_L &= 2\int_0^{\theta_0} 2\pi\left(x_0 + R\cos\theta'\right)R\,\mathrm{d}\theta' \\ &= 4\pi R\left(x_0\theta_0 + R\sin\theta_0\right), \end{aligned} \tag{3}$$

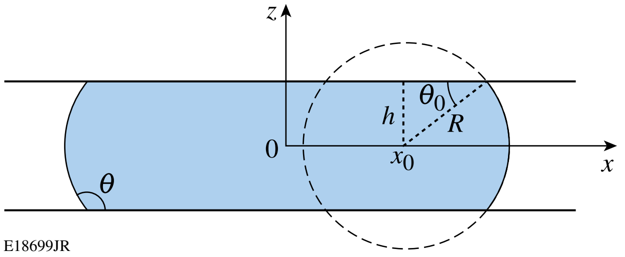

Figure 123.50
Droplet geometry when sandwiched between parallel plates.

$$S_B = 2\pi\left(x_0 + R\cos\theta_0\right)^2. \tag{4}$$

When $\theta < 90°$, droplet volume and droplet surfaces can be derived as

$$V = 2\pi\left[\left(x_0^2 + R^2\right)h - \frac{1}{3}h^3 - 2x_0R^2\left(\frac{1}{2}\theta_0 + \frac{1}{4}\sin 2\theta_0\right)\right], \tag{5}$$

$$\begin{aligned} S_L &= 2\int_0^{\theta_0} 2\pi\left(x_0 - R\cos\theta'\right)R\,\mathrm{d}\theta' \\ &= 4\pi R\left(x_0\theta_0 - R\sin\theta_0\right), \end{aligned} \tag{6}$$

$$S_B = 2\pi\left(x_0 - R\cos\theta_0\right)^2, \tag{7}$$

where $\theta_0 = \pi/2 - \theta$ and $R = h/\cos\theta$.

Several studies[19,20] have reported that, for a water-in-oil DE droplet in the parallel-plate structure, the oil becomes entrapped underneath the inner water droplet as illustrated in Fig. 123.51(b). We analyzed the Gibbs surface energy change for both cases of the water droplet resting on the Teflon surface and the water droplet on a thin layer of oil. Using Eqs. (2)–(7) and the interfacial tension data shown in Table 123.VI, we calculate ΔG for water-in-silicone oil (20 cst) DE for the configurations of Figs. 123.51(a) and 123.51(b). ΔG per unit total liquid volume is expressed as the ratio of the volume of water to the total volume of water and oil in the DE. Both configurations give ΔG < 0, but the configuration with the oil entrapped underneath the water system is energetically favored.

As noted above, a water droplet and an oil droplet usually combine to form a water-in-oil DE because water has a higher surface tension than most oils, but we can reverse this tendency if we add surfactant Silwet L-77 to the water. The interfacial tension for Silwet-treated water (at the surfactant concentration of 0.0625 wt%, listed in Table 123.VI) is greater than silicone oil, but lower than mineral oil. Therefore it is not effective to choose silicone oil for oil-in-water DE's. Instead, we chose mineral oil and then calculated ΔG for water treated with mineral oil–in–Silwet as a function of the volume ratio of mineral oil.

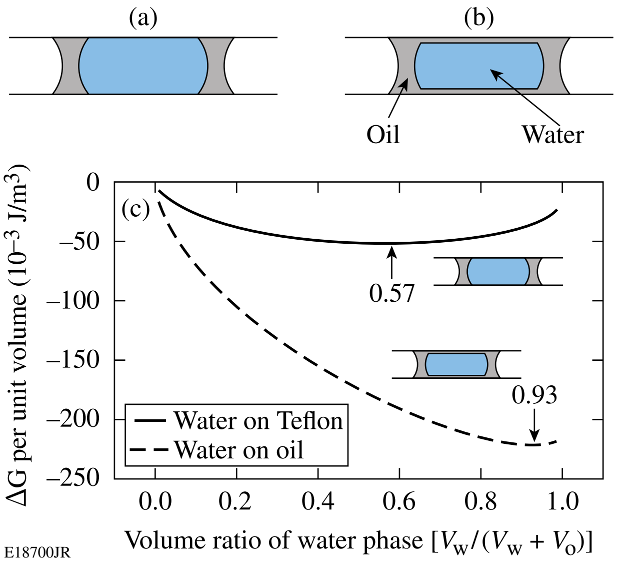

Figure 123.51
Water-in-silicone oil (20 cst) DE droplet in the parallel-plate structure: (a) the inner water droplet rests on the Teflon surface; (b) the inner water droplet rests on a thin layer of oil; (c) ΔG of DE formation for both cases (a) and (b).

Table 123.VI: Interfacial tension data at room temperature (mN/m).

Interface	Interfacial tension
Water/air	74
Silicone oil (20 cst)/air	20.6
Mineral oil/air	28.1
Silicone oil (20 cst)/water	35
Mineral oil/water	49
Water/Teflon^{TM}	49
Silicone oil (20 cst)/Teflon^{TM}	5.6
Mineral oil/Teflon^{TM}	10.25
Teflon^{TM}/air	18
$W_{S-t}/$air	24.7
Mineral oil/W_{S-t}	4.5
$W_{S-t}/$Teflon^{TM}	2.46

W_{S-t}: Silwet-treated water (0.0625 wt%)

As shown in Fig. 123.52, the requirement for DE formation, ΔG < 0, is met. Similar to water-in-oil DE's, one might also wonder whether a thin layer of water could be entrapped underneath the oil droplet. To test for this possibility, we calculated ΔG for both this case and the case of oil resting directly on Teflon surface. Figure 123.52 shows that the energy is minimized when the inner oil droplet is separated from the Teflon surface by a layer of water. We have some evidence for this configuration but further experimental verification is needed.

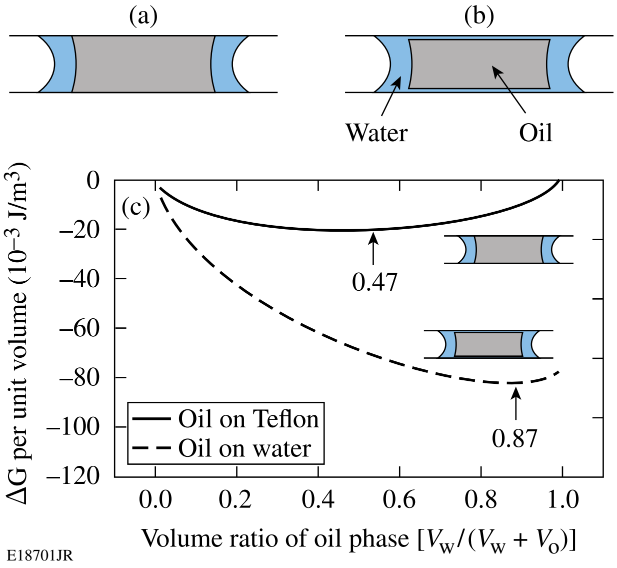

Figure 123.52
Mineral oil–in–Silwet-treated-water DE formation in parallel plates; (a) the inner oil droplet rests on the Teflon surface; (b) the inner oil droplet rests on a thin layer of water; (c) ΔG of DE formation for both cases (a) and (b).

2. Experiments for Water-in-Oil DE Formation

We tested the electric-field–actuated formation of water–in–silicone oil DE as shown in Fig. 123.53. Two silicone oil droplets were first dispensed from the left reservoir through DEP by applying 330-V_{rms}, 100-Hz ac voltage on the lower array of electrodes. Then, two DI water droplets were dispensed from the right reservoir through EWOD actuation by application of 85-V_{rms}, 100-Hz ac voltage on the upper array of electrodes. With the same EWOD actuation voltages, the water droplets were then transported toward the oil droplets as shown in Figs. 123.53(c) and 123.53(d). After the water droplets touched the oil droplets, they were engulfed by the oil droplets to form DE droplets [see Fig. 123.53(e)]. Furthermore, the water droplets were able to pull the whole merged water-in-oil DE droplets by low-voltage EWOD transport [Fig. 123.53(f)].

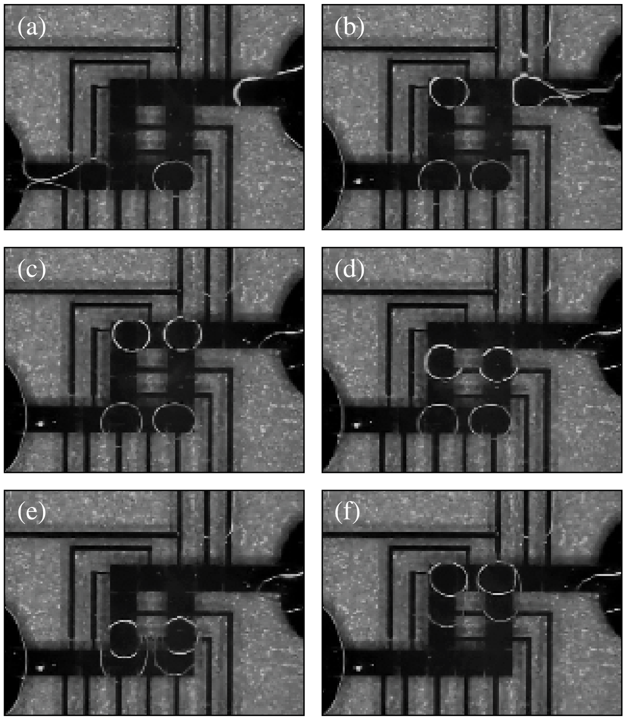

E18616JR

Figure 123.53
The formation of water-in-silicone oil DE droplets. (a) Two silicone oil droplets are dispensed through DEP actuation by applying 330-V_{rms}, 100-Hz ac voltage; (b) two DI water droplets are dispensed by EWOD actuation by applying 85-V_{rms}, 100-Hz ac voltage; [(c)–(e)] the water droplets are delivered and combined with oil droplets to form DE droplets; (f) the water droplets drag merged water-in-oil DE droplets by EWOD actuation.

3. Experiments for Oil-in-Water DE Formation.

We performed dispensing experiments with Silwet-treated water solutions of five wide ranging concentrations: 0.00625, 0.0125, 0.025, 0.0625, and 0.125 wt%. Only the 0.00625-wt% Silwet solution could be dispensed smoothly. All the others formed a remarkably persistent "tether" during the pinch-off process. As shown in Fig. 123.54(a), the thin liquid tether is formed between the reservoir and the droplet, preventing its separation. A full understanding of the tether formation is still lacking, but similar experiments in oil media show that surfactant-treated water can be successfully dispensed without tether formation.[10,11]

One way to break the tether is to use a second liquid finger to disturb it; this mechanism is shown in Fig. 123.54. The secondary liquid used was pure DI water. When the pure-water finger touches the tether, the Silwet solution in the contact area is diluted locally and the tether breaks because of the increased surface tension. The entire tether disintegrates into many satellite droplets because of hydrodynamic instability [see Fig. 123.54(d)].

This method does not work when the Silwet concentration exceeds 0.125 wt%, in which case the second water finger seems to mix with the tether instead of breaking it. Apparently the local dilution is not sufficient to increase the surface tension when the Silwet concentration is far above critical micelle concentration. Another problem with the tether formed during dispensing is that

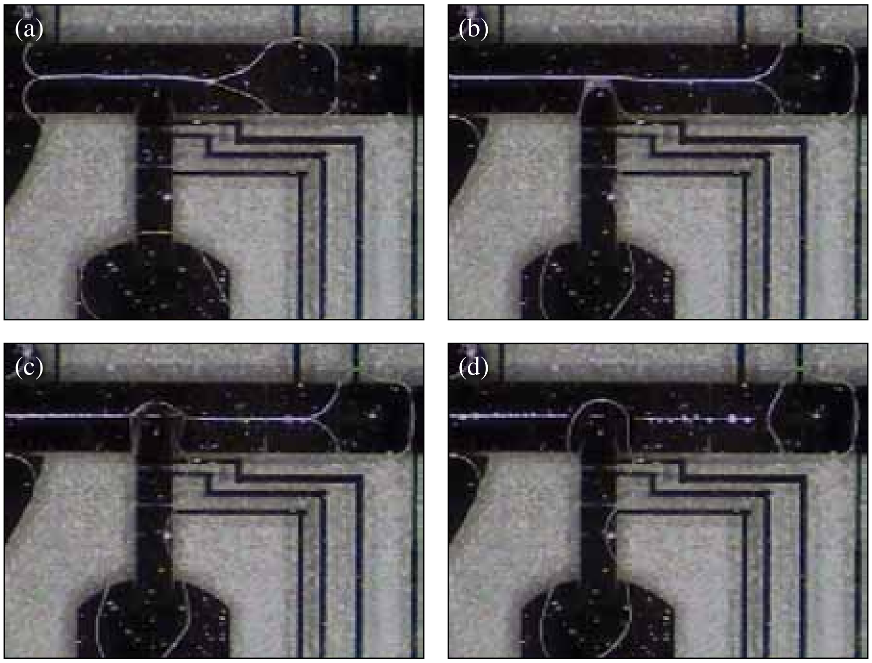

E18703JR

Figure 123.54
Breaking the tether with a second water liquid finger. (a) The second liquid (DI water) in a reservoir; (b) the second liquid finger approaches the "tether"; (c) the tether breaks inside the second liquid finger; (d) the entire tether disintegrates into many satellite droplets.

the electrode shape loses some of its influence in defining the pinch-off curvature, resulting in a poor volume reproducibility.

4. Other Possible Solutions to the Tether Problem

A second method to avoid the tether is by taking advantage of the pH effect on spreading of Silwet solutions. Radulovic[21] found that the wetting ability of Silwet solutions is drastically reduced with the addition of acetic acid, possibly because of the polarization of the trisiloxane head. We also found in experiments that the Silwet surfactant could be strongly affected by the addition of other acids (such as HCl) or bases (such as KOH), and the change in wetting ability by the pH effect is reversible by neutralization. In our work, we have demonstrated that the addition of acid to Silwet-treated water can prevent the tether formation. Then, the dispensed droplet is neutralized by mixing with another base droplet. In this way, the required low surface tension is recovered. The droplet now containing some salts can be used for oil-in-water DE's. The problem with this method is that the reversal process using a base solution takes a long time, typically more than an hour. This waiting time would be a major disadvantage for mass production of DE droplets. Also, evaporation of water during such a long period must be prevented.

A third approach would be to add the surfactant to the oil to avoid tether formation. We have found that Silwet has little influence on the wetting property of oils and Silwet-doped oil can be dispensed smoothly. When a pure water droplet and a Silwet-doped oil droplet are placed together, an oil-in-water DE droplet is formed because Silwet tends to stay in water phase. Unfortunately, the DE droplet formation takes some time because the Silwet diffuses gradually across the interface from the oil phase into the water phase. Using 0.125% (v/v) Silwet–added mineral oil and DI water droplets, the process takes several minutes. When a 0.5% (v/v) Silwet–modified mineral oil drop is used, the diffusion time is reduced to about 10 s.

Conclusion

In this article, we have demonstrated that aqueous and non-aqueous liquid droplets can be dispensed from reservoirs on a microfluidic chip and the dispensed droplets can then be combined to form oil-in-water-in-air (O/W/A) or water-in-oil-in-air (W/O/A) DE droplets. In the dispensing process, droplet volume reproducibility has been tested over a range of operational parameters, including applied voltage and the length of the cutting electrode. We find that drop volume variability is caused mainly by variability in the tail volume during pinch-off. When the length of the cutting electrode is increased, volume reproducibility is degraded because longer cutting electrodes reduce the influence of the electrode structure on the radius of curvature in the pinch-off region.

The Gibbs free energy change can be used to test the ability to form stable DE droplets. The result indicates that (1) water-in-oil DE droplets form through spontaneous emulsification and (2) oil-in-water DE droplets can also be formed by the addition of surfactant and the proper selection of oil. Experimental results show the formation of water-in-oil DE droplets. Using simultaneous DEP and EWOD actuation on a microfluidic chip, dielectric (oil) and conductive (water) droplets have been dispensed, and merged, and the transport of the merged water-in-oil DE droplet has been demonstrated.

The formation of water DE droplets treated with mineral oil–in–Silwet has been demonstrated. We find that a tether is formed during the dispensing of Silwet-treated water. Although the tether can be broken by the disturbance of a second liquid finger, it interferes with the dispensing operation and degrades dispensing reproducibility. Other methods to avoid the tether include taking advantage of the pH effect on Silwet solutions and adding the surfactant to the oil phase. Further effort to develop a more reliable formation method for oil-in-water DE is needed; for example, a surfactant more sensitive to pH might react more quickly so that its recovery of wetting ability (the contact angle reversal) would take much less time. Alternatively, low-surface-tension water could be dispensed in an oil medium without forming a tether. These schemes will be tested for oil-in-water DE formation.

ACKNOWLEDGMENT

This work was supported by the U.S. Department of Energy Office of Inertial Confinement Fusion under Cooperative Agreement No. DE-FC52-08NA28302, the University of Rochester, and the New York State Energy Research and Development Authority. The support of DOE does not constitute an endorsement by DOE of the views expressed in this article.

Appendix A: Requirements on DE Droplet Uniformity for Laser-Target Fabrication

The foam shell structure of a concentric laser target is shown in Fig. 123.55. V_1 and V_2 are the volumes of the inner oil phase and the outer water phase, respectively:

$$V_1 = \frac{4\pi}{3} R_1^3 \text{ and } V_1 + V_2 = \frac{4\pi}{3} R_2^3.$$

The shell thickness is $d = R_2 – R_1$; therefore, d can be written

$$d = \frac{\left(\frac{3}{\pi}\right)^{1/3} \cdot \left(V_1 + V_2\right)^{1/3}}{2^{2/3}} - \frac{\left(\frac{3}{\pi}\right)^{1/3} \cdot V_1^{1/3}}{2^{2/3}}. \qquad \text{(A1)}$$

By taking partial derivatives of Eq. (A1), we obtain an expression for the uncertainty of d in terms of the uncertainties of V_1 and V_2

$$\Delta d = \left| \Delta V_1 \cdot \left[\frac{1}{6^{2/3} \pi^{1/3} \left(V_1 + V_2\right)^{2/3}} - \frac{1}{6^{2/3} \pi^{1/3} V_1^{2/3}} \right] \right| + \left| \Delta V_2 \cdot \frac{1}{6^{2/3} \pi^{1/3} \left(V_1 + V_2\right)^{2/3}} \right|. \qquad \text{(A2)}$$

The specified dimensions of an inertial fusion energy (IFE) target are $2R_2 = 4 \pm 0.2$ mm, $d = 289 \pm 20$ μm. By substituting these values into Eq. (A2), we can determine wall-thickness variation ($\Delta d/d$) in terms of water and oil volume variations ($\Delta V/V$) (refer to Fig. 123.56). Different wall thickness variations ($\Delta d/d$) are represented by a set of straight lines in the $\left(\Delta V_1/V_1\right)$ versus $\left(\Delta V_2/V_2\right)$ chart. These lines have the same slope, and small ($\Delta d/d$) lines are closer to the original point. The shaded area indicates where the requirement on wall thickness variation is satisfied, i.e., $\Delta d/d < 20/289 = 6.92\%$. For example, if the oil volume variation $\left(\Delta V_1/V_1\right)$ is 5% and the water volume variation $\left(\Delta V_2/V_2\right)$ is 4%, the corresponding point indicated by a star in Fig. 123.56 is located within the shaded area, which means the wall thickness condition meets the requirement.

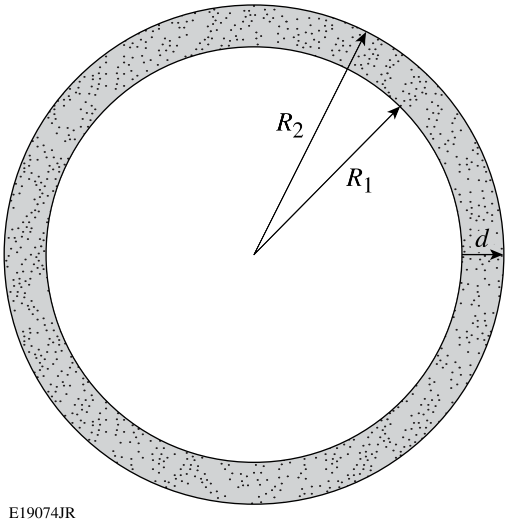

Figure 123.55
The foam shell structure of a concentric laser target.

The red line in Fig. 123.56 represents where the changes of water- and oil-phase absolute volumes are the same, and the blue line represents where the relative volume variations of water and oil phases are the same. Under the condition of identical relative volume variations, $\left|\Delta V_1/V_1\right| = \left|\Delta V_2/V_2\right|$ must be smaller than 4.97% to meet the laser target requirement.

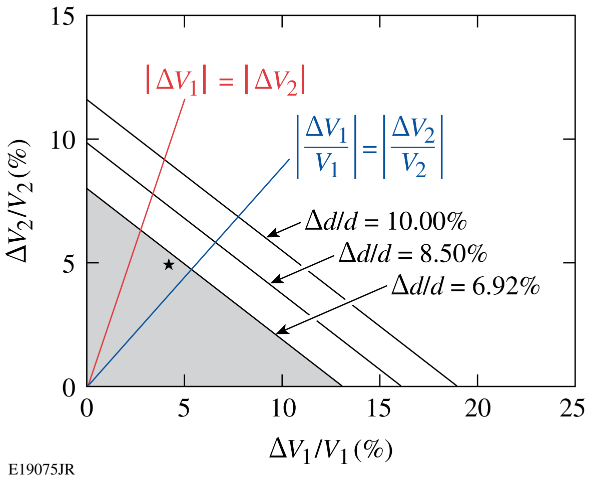

Figure 123.56
Sensitivity analysis of shell wall thickness for an IFE target.

REFERENCES

1. S. M. Lambert *et al.*, J. Appl. Polym. Sci. **65**, 2111 (1997).
2. R. Paguio *et al.*, in *Assembly at the Nanoscale—Toward Functional Nanostructured Materials*, edited by C. S. Ozkan *et al.*, Mat. Res. Soc. Symp. Proc. Vol. 901E (Materials Research Society, Warrendale, PA, 2006), Paper 0901-Ra05-23-Rb05-23.
3. N. Pannacci *et al.*, Phys. Rev. Lett. **101**, 164502 (2008).
4. A. S. Utada *et al.*, Science **308**, 537 (2005).
5. S. Okushima *et al.*, Langmuir **20**, 9905 (2004).
6. R. B. Fair, Microfluid Nanofluid **3**, 245 (2007).
7. T. B. Jones, Langmuir **18**, 4437 (2002).
8. M. G. Pollack, R. B. Fair, and A. D. Shenderov, Appl. Phys. Lett. **77**, 1725 (2000).
9. S. K. Cho, H. Moon, and C.-J. Kim, J. Microelectromech. Syst. **12**, 70 (2003).

10. H. Ren, R. B. Fair, and M. G. Pollack, Sens. Actuators B, Chem. **98**, 319 (2004).
11. J. Berthier *et al.*, Sens. Actuators A, Phys. **127**, 283 (2006).
12. R. B. Fair *et al.*, in IEEE International Electron Devices Meeting (IEDM 2003) (IEEE, New York, 2003), pp. 32.5.1–32.5.4.
13. T. B. Jones and M. Washizu, J. Electrostatics **37**, 121 (1996).
14. P. R. C. Gascoyne and J. V. Vykoukal, Proc. IEEE **92**, 22 (2004).
15. D. Chatterjee *et al.*, Lab Chip **6**, 199 (2006).
16. S.-K. Fan, T.-H. Hsieh, and D.-Y. Lin, Lab Chip **9**, 1236 (2009).
17. T. B. Jones, K.-L. Wang, and D.-J. Yao, Langmuir **20**, 2813 (2004).
18. K.-L. Wang and T. B. Jones, J. Micromech. Microeng. **14**, 761 (2004).
19. M. Bienia *et al.*, Physica A **339**, 72 (2004).
20. A. Staicu and F. Mugele, Phys. Rev. Lett. **97**, 167801 (2006).
21. J. Radulovic, K. Sefiane, and M. E. R. Shanahan, J. Colloid Interface Sci. **332**, 497 (2009).

Charge-Injection-Device Performance in the High-Energy-Neutron Environment of Laser-Fusion Experiments

Introduction

Electronic devices such as charge-coupled devices (CCDs)[1] or charge-injection devices (CIDs)[2] (the subject of this work) are used to image x rays emitted by laser-generated plasmas. The laser beam or beams interact with the target in various ways depending on the total energy- and intensity-generating, short-lived plasmas whose temperatures are such that either thermal or nonthermal x-ray emission takes place. X-ray imaging and x-ray spectroscopy are used in such research to diagnose conditions in the plasma. The laser–target interactions for laser intensities exceeding ~10^{14} W/cm^2 result in plasma temperatures in the keV regime. During ablation and implosion of targets in laser-driven fusion experiments, stagnation core temperatures as high as ~10 keV can be obtained[3] and are expected for conditions approaching ignition at the National Ignition Facility (NIF).[4] Simultaneously with the x-ray emission, a burst of fusion-generated neutrons is emitted by the imploding target at the time of implosion stagnation. Maximum neutron yields of ~10^{14} (DT, neutron energy 14.1 MeV) are currently generated at LLE's Omega Laser Facility[5] and are expected to be far exceeded on the NIF. At a yield of 10^{14} the neutron fluence at 1 m from the target, if unattenuated, is ~8×10^8 neutrons/cm^2. In a typical 25-μm × 25-μm pixel region of an imaging array, this neutron fluence corresponds to ~5×10^3 neutrons per pixel. Clearly, if the solid-state device is sensitive to either the neutrons or neutron-induced γ rays or neutron-generated charged particles, this flux level could cause the device to be incapable of being used for imaging x rays.

The effects of ionizing radiation, both γ rays and charged particles, on silicon[6] and on silicon-based photodetectors such CCDs[7] have been studied. γ rays and, therefore, neutron-induced γ rays, can cause bulk damage through Compton scattering of the γ rays by atomic electrons. The displaced Si atoms can permanently affect the noise level of the device or, if enough defects are created, render it unusable. While not immune to such effects, the unique architecture of the CID[2] makes it radiation tolerant.[8] CID cameras able to withstand radiation levels of 10^6-rad/h and 10^7-rad accumulated dose are available.[9]

In this work the effects of high-energy (DT) neutrons on the CID cameras are examined. The experiments were performed on the 60-beam, UV OMEGA Laser.[5] Implosions of DT-filled capsules on OMEGA can generate neutron yields of up to ~10^{14} (Ref. 10). CID cameras are used on this system in a number of x-ray imaging diagnostics[11] at a range of distances (0.8 to 2.6 m) experiencing neutron fluences ranging from 10^7 to 10^9 neutrons/cm^2. It is demonstrated in this work that the resulting background and noise levels in the CID cameras are a function of the neutron fluence and that usable images are obtained throughout this fluence range. Furthermore, numerical processing of the images reduces neutron-induced noise in the x-ray images obtained during high-yield target experiments, extending the useful range to higher neutron yields/fluences.

Neutron-Induced Signal in CID Cameras

The CID cameras used in this work (model CID4150-DX3)[12] are the primary means of image acquisition at the Omega Laser Facility in a set of x-ray pinhole cameras (XPHCs)[13] and an x-ray microscope that uses a Kirkpatrick–Baez reflection optic to obtain x-ray images. The x-ray microscope system, known as the gated monochromatic x-ray imager (GMXI),[14] was used with CID cameras at the image plane in a time-integrating broadband mode. The sensitive x-ray range of the GMXI is ~2 to 7 keV, limited at the low end by transmission through a Be blast shield and at the high end by Ir-mirror reflectivity.[14] The XPHCs are similarly limited at low x-ray energies but contain no high-energy mirror cutoff. Target-emission spectral shape makes the energy ranges comparable.

The model CID4150-DX3 is an 812 × 607-pixel array of square photodiodes with 38.5 μm center-to-center spacing. The active area is 31.3×23.2 mm^2 and is housed inside an aluminum case with 48- × 30-mm outside dimensions. The well depth for each pixel is ~1.4×10^6 e–h pairs and the depletion region depth is ~7 μm (Ref. 15). The sensors are front-side illuminated and have an equivalent dead layer of ~1 μm Si (Ref. 15). The sensors do not have a phosphor coating, and all cameras in this study were operated in vacuum with a 25-μm-thick Be window in front of the sensor (toward target). In general the images in this study consist of an accumulated signal caused by x rays in the range of 2 to 7 keV.

Figures 123.57 and 123.58 show example x-ray images taken on typical D–T neutron-generating target experiments with an XPHC and the GMXI. The images are displayed in units of ADUs (analog-to-digital units). The XPHC image [Fig. 123.57(a)] is at a high neutron fluence (~4×10^8 neutrons/cm^2) because of its proximity to the target (0.8 m), while the GMXI image [Fig. 123.58(a)] was taken at a much lower neutron fluence (~3×10^7 neutrons/cm^2). Both target shots had the same approximate yield (3×10^{13} neutrons). The images are improved [Figs. 123.57(c) and 123.58(c)] by processing the images using deglitching and filtering (described later in the text).

The neutron-induced effects in a set of images (~100) with neutron yields ranging from 3×10^{12} to 6×10^{13}, with CID cameras in both XPHCs and the GMXI, were determined as follows: The average signal level in the camera was determined in a 400 × 400-pixel region not containing the x-ray image and not shielded by any of the pinhole-camera support structure. The root-mean-square fluctuations (σ_{rms}) were computed from the variations of the mean signal in the same region. In all cases, the images are corrected for non-target–induced background (primarily dark current) by subtracting a frame taken before the laser shot (1.2 s before shot). The subtraction of the background frame is always a good idea and in the mode of operation of the CID cameras used in this work (uncooled) is essential. All values of background and σ_{rms} are plotted as a function of neutron fluence (yield over $4\pi d^2$, where d is the distance). Two CID cameras were in XPHC's at a distance of 0.8 m to the target, and one was in an XPHC at a distance of 1.9 m. Additionally, two CID cameras were in the GMXI at a distance of 2.6 m. The DT-neutron yields were obtained from a fully cross-calibrated set of neutron detectors.[16] The absolute neutron yields measured by these detectors are accurate to better than 10%.

Figure 123.59 shows the average neutron-induced signal level for all cameras as a function of neutron fluence. The signal level is seen to follow a straight line of slope ~1, meaning

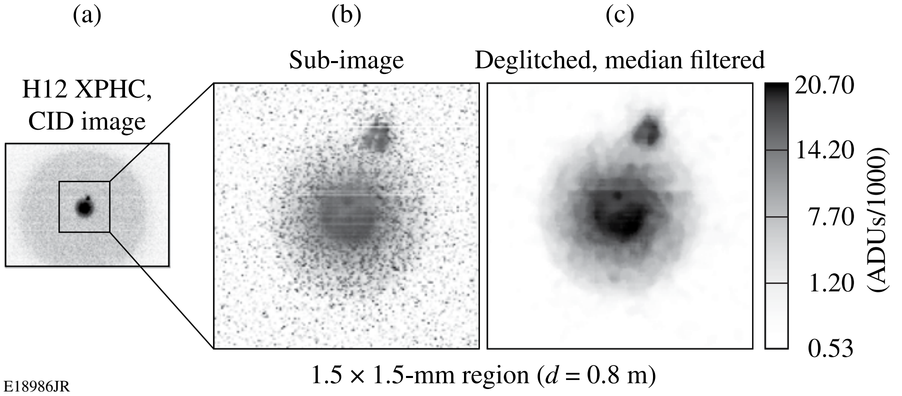

Figure 123.57
An x-ray image obtained with a CID camera in an OMEGA XPHC on a high-(DT) neutron-yield target shot (yield ~3×10^{13}). (a) The full image with neutron-induced background and noise, (b) An unprocessed sub-image representing a 2 × 2-mm region at the target. Single-pixel events are evident as are some line upsets. (c) A deglitched and median-filtered version of the same sub-image.

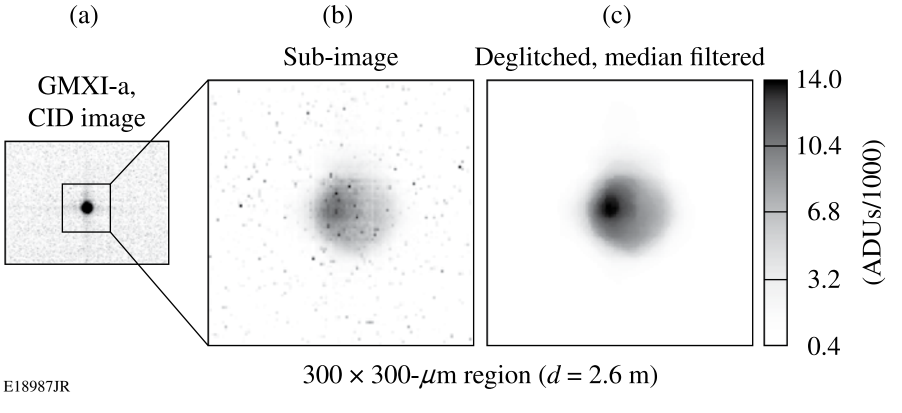

Figure 123.58
An x-ray image obtained with a CID camera in the GMXI on a target shot with similar yield to the XPHC image in Fig. 123.57 (yield ~3×10^{13}). (a) Full image, (b) unprocessed sub-image representing a 500 × 500-μm region at the target, and (c) a deglitched and median-filtered version of the same.

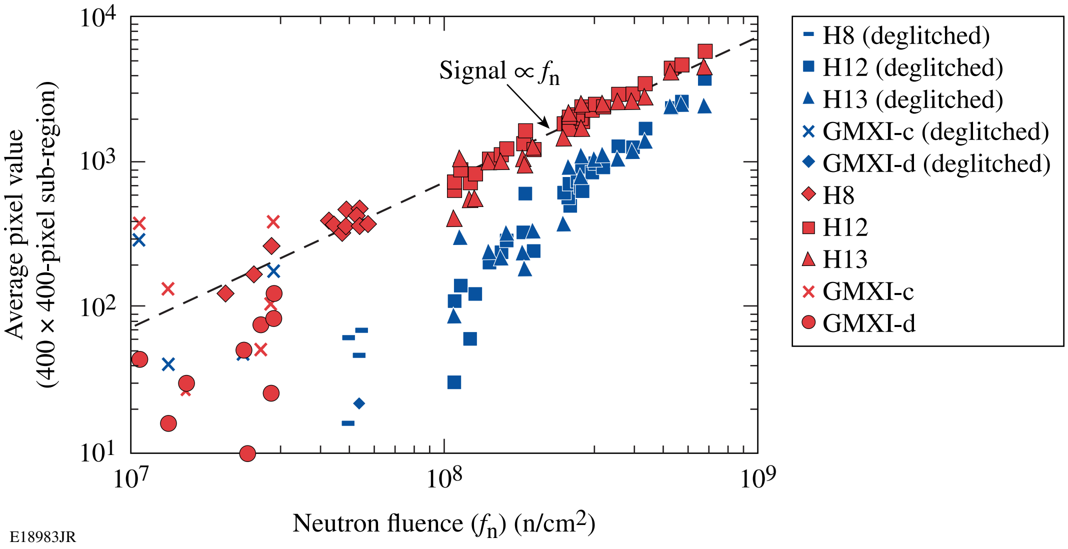

Figure 123.59
The average pixel value in ADUs for 400 × 400-pixel regions in all of the CID cameras for regions not containing x-ray images as a function of the neutron fluence. The red (upper) values are from non-deglitched images and the blue (lower) values are from deglitched images.

it is proportional to the neutron fluence (f_n). As is noticed in Figs. 123.57 and 123.58, the neutron-induced signal consists of a near-single-pixel component as well as a more-uniform background. The single-pixel events are likely to be induced by n–p protons generated by neutron interaction with the 25-μm-thick Be window just in front of the CID sensor, while the uniform background is a consequence of n-gammas interacting with the CID sensor. (A study of the charged-particle sensitivity of this model of CID camera can be found in Fletcher *et al.*[17]). Jaanimagi *et al.*[18] found a similar phenomenological effect on CCDs used for streak-camera recording at the Omega Facility.

The single-pixel events are effectively removed by deglitching the images. That is accomplished here by running a program that tests the values found in a 5 × 5-pixel region. If the value of the pixel is greater than 1.25 times the median of that region, then the value is replaced by the median. This first step removes most of the high-signal-level single-pixel events. A second pass over the image, where the pixel value is replaced by the median of the pixel values resulting from the first pass, further reduces noise in the image. (More sophisticated noise-removal algorithms such as those compared in Chen and Yang[19] are capable of even more thorough noise removal but are outside the scope of this article.) Examples of the improvements in the images are shown in Figs. 123.57(c) and 123.58(c). The lowering of the average signal level caused by deglitching is seen in the lower curve of values in Fig. 123.59 (deglitched values are those of step 1; no additional median filtering is applied).

The variation of the neutron-induced signal σ_{rms} is shown in Fig. 123.60. The variation is seen to follow a curve of slope ~1/2 making it proportional to $(f_n)^{1/2}$. Again, deglitching suppresses the noise by eliminating the high-signal-level single-pixel events (lower curve of values seen in Fig. 123.60). The maximum signal level detected in any given pixel (taken here to be ~1.4 × 10^6 electron-hole pairs, corresponding to ~20,000 ADUs) limits the maximum detected x-ray signal. For instance, at 1 keV for an assumed e–h pair energy of 3.3 eV, the maximum number of absorbed photons is 4600. The maximum signal-to-noise ratio (SNR$_{\text{max}}$) achievable is therefore ~$(n)^{1/2}$, where n is the number of photons absorbed. At 1 keV this is ~68 per pixel for the CID camera or, using the same argument, ~21 at 10 keV.

Figure 123.61 shows the computed SNR$_{\text{max}}$ after background subtraction, with and without deglitching, for the same set of target experiments. Usable images are obtained for the highest neutron fluences encountered, with deglitching increasing the SNR by a factor of 3 or more. For comparison, the SNR$_{\text{max}}$ achievable from photon-counting statistics for the 1-keV and 10-keV photon-energy cases are shown as horizontal dashed lines in Fig. 123.61. For the non-deglitched images the SNR is affected above neutron fluences of ~3 × 10^7 neutrons/cm^2. For the deglitched images the SNR is restored to more than can be achieved with counting statistics alone for neutron fluences of up to ~10^8 neutrons/cm^2 for 1-keV photons or ~3 × 10^8 neutrons/cm^2 for 10-keV photons.

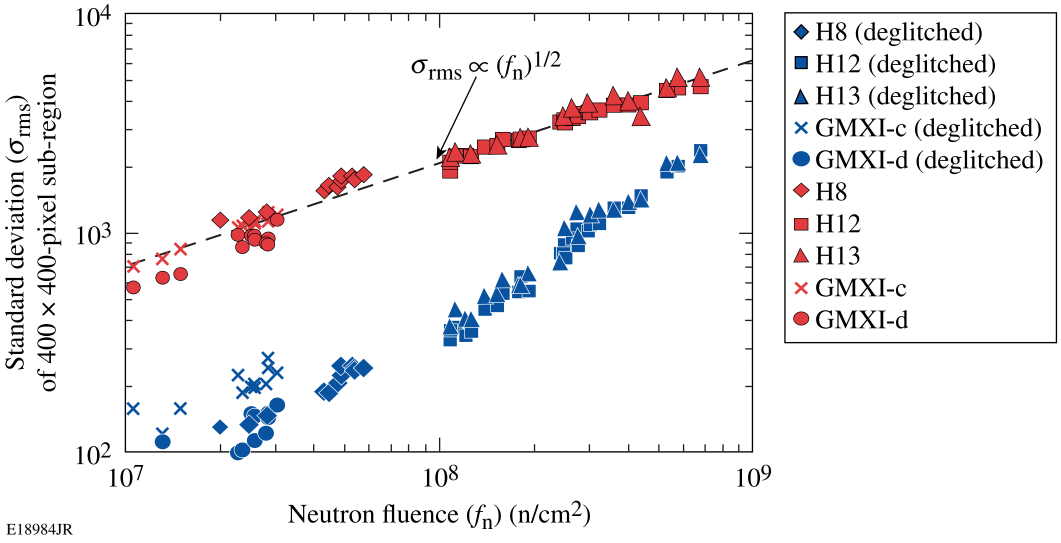

Figure 123.60
The standard deviation of the pixel values σ_{rms} as a function of neutron fluence for CID images from non-deglitched (red, upper) and deglitched (blue, lower) images.

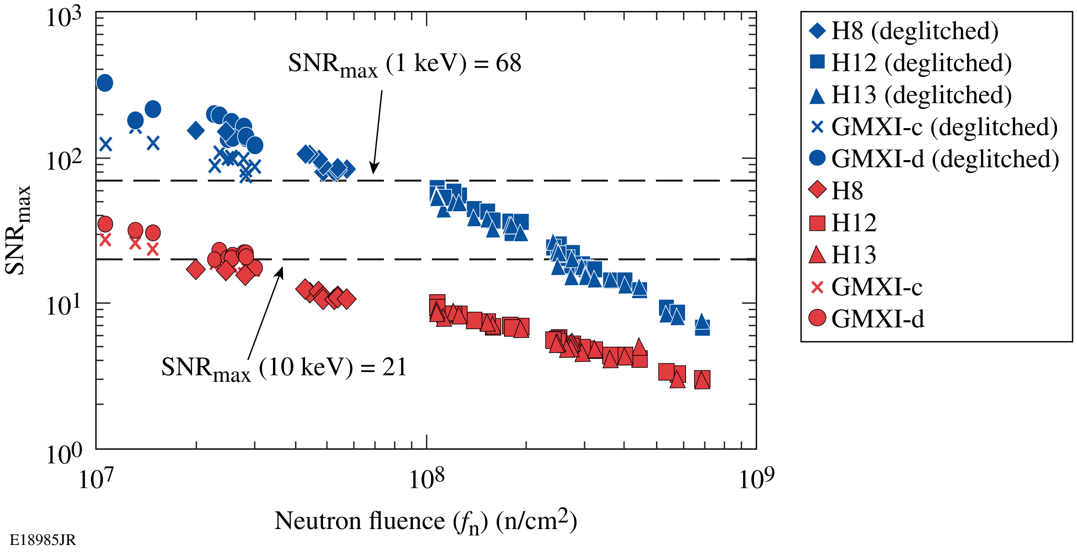

Figure 123.61
The computed maximum signal-to-noise ratio (SNR$_{max}$) as a function of neutron fluence from non-deglitched and deglitched images from all CID cameras. The dashed lines are the maximum SNR's obtainable from photon-counting statistics for 1- and 10-keV photons.

A further improvement of the SNR is achieved if the CID camera is shielded from the direct line of sight to the target with sufficient material to attenuate the neutron-induced signal. In the case described here (Fig. 123.62) the regions of the CID cameras in the XPHCs that are shielded by the body of the pinhole camera (~13 mm of stainless steel in the path) have a reduced background signal induced by the high-energy neutrons. For the cases shown, the shielding decreases the background and noise and increases the SNR, making it possible to use the CID cameras at inferred neutron fluences up to ~10^{10} neutrons/cm^2 (extrapolation of the shielded SNR trend). At 1 m this corresponds to a neutron yield of ~10^{15}. To make practical use of shielding, however, the direct path to the target must be blocked. The diagnostic must therefore incorporate reflectors such as grazing-incidence mirrors, as in a KB microscope, or crystal-diffraction elements, as in a spectrometer.

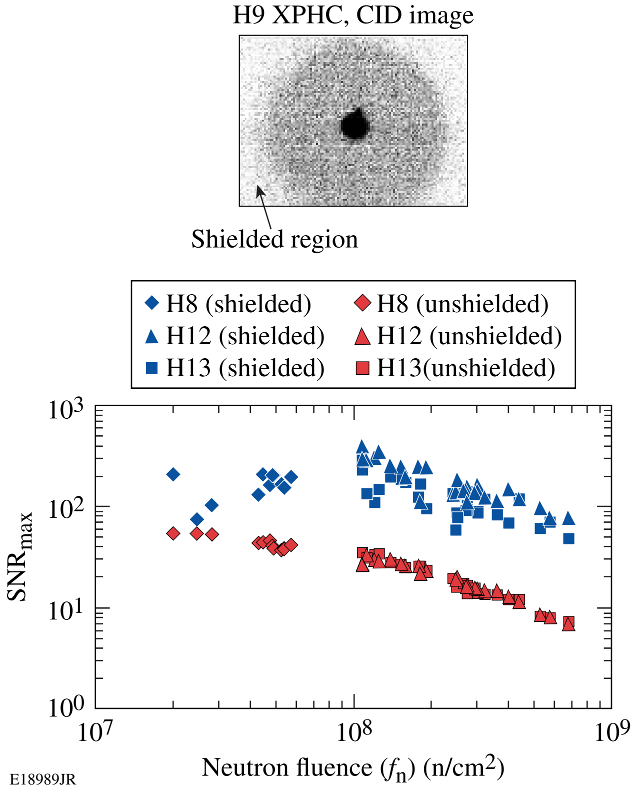

Figure 123.62
The computed SNR_{max} for shielded and unshielded regions of CID cameras in OMEGA XPHCs as a function of neutron fluence. Both cases are for deglitched images.

Conclusions

The CID camera used in this work (model CID4150-DX3)[11] is seen to maintain usability in the high-energy neutron environment of DT-bearing target experiments currently being undertaken at the Omega Laser Facility, where yields up to ~10^{14} can be generated. The neutron-induced effects on the cameras are seen to scale with neutron fluence and therefore are inversely proportional to the square of the distance from the target to the camera. Deglitching the x-ray images obtained during high-energy neutron-target experiments reduces the noise and increases the fluence range that useful x-ray images can be obtained up to ~3 × 10^8 neutrons/cm^2. Shielding the cameras from the direct line of sight to the target can further reduce the neutron-induced background, and an inferred yield of ~10^{15} at 1 m could be tolerated if shielding comparable to or better than that used in this study is incorporated into the diagnostic. This, however, requires the use of reflectors or diffractors. This study indicates that the CID camera will be a useful means of obtaining time-integrated x-ray images on the NIF up to yields of ~10^{15} or more depending on distance to the target and shielding.

ACKNOWLEDGMENT

This work was supported by the U.S. Department of Energy Office of Inertial Confinement Fusion under Cooperative Agreement No. DE-FC52-08NA28302, the University of Rochester, and the New York State Energy Research and Development Authority. The support of DOE does not constitute an endorsement by DOE of the views expressed in this article.

REFERENCES

1. J. R. Janesick *et al.*, Opt. Eng. **26**, 156 (1987).
2. J. Carbone *et al.*, in *Solid State Sensor Arrays: Development and Applications II*, edited by M. M. Blouke (SPIE, Bellingham, WA, 1998), Vol. 3301, pp. 90–99.
3. J. D. Lindl, *Inertial Confinement Fusion: The Quest for Ignition and Energy Gain Using Indirect Drive* (Springer-Verlag, New York, 1998).
4. W. J. Hogan, E. I. Moses, B. E. Warner, M. S. Sorem, and J. M. Soures, Nucl. Fusion **41**, 567 (2001).
5. T. R. Boehly, D. L. Brown, R. S. Craxton, R. L. Keck, J. P. Knauer, J. H. Kelly, T. J. Kessler, S. A. Kumpan, S. J. Loucks, S. A. Letzring, F. J. Marshall, R. L. McCrory, S. F. B. Morse, W. Seka, J. M. Soures, and C. P. Verdon, Opt. Commun. **133**, 495 (1997).
6. R. Korde *et al.*, IEEE Trans. Nucl. Sci. **36**, 2169 (1989).
7. J. Janesick, T. Elliott, and F. Pool, IEEE Trans. Nucl. Sci. **36**, 572 (1989).
8. J. Carbone, S. Czebiniak, and R. Carta, in *Robotics and Remote Systems*, edited by L. M. Kostelnik, Proceedings of the Conference on Robotics and Remote Systems (American Nuclear Society, La Grange Park, IL, 1996), Vol. 43, pp. 43–50.
9. J. J. Zarnowski *et al.*, in *Charge-Coupled Devices and Solid State Optical Sensors IV*, edited by M. M. Blouke (SPIE, Bellingham, WA, 1994), Vol. 2172, pp. 187–198.

10. J. M. Soures, R. L. McCrory, C. P. Verdon, A. Babushkin, R. E. Bahr, T. R. Boehly, R. Boni, D. K. Bradley, D. L. Brown, R. S. Craxton, J. A. Delettrez, W. R. Donaldson, R. Epstein, P. A. Jaanimagi, S. D. Jacobs, K. Kearney, R. L. Keck, J. H. Kelly, T. J. Kessler, R. L. Kremens, J. P. Knauer, S. A. Kumpan, S. A. Letzring, D. J. Lonobile, S. J. Loucks, L. D. Lund, F. J. Marshall, P. W. McKenty, D. D. Meyerhofer, S. F. B. Morse, A. Okishev, S. Papernov, G. Pien, W. Seka, R. Short, M. J. Shoup III, M. Skeldon, S. Skupsky, A. W. Schmid, D. J. Smith, S. Swales, M. Wittman, and B. Yaakobi, Phys. Plasmas **3**, 2108 (1996).

11. F. J. Marshall, T. Ohki, D. McInnis, Z. Ninkov, and J. Carbone, Rev. Sci. Instrum. **72**, 713 (2001).

12. Thermo Fisher Scientific Instruments Division, CIDTEC Cameras and Imagers, Liverpool, NY 13088.

13. R. A. Forties and F. J. Marshall, Rev. Sci. Instrum. **76**, 073505 (2005).

14. F. J. Marshall and J. A. Oertel, Rev. Sci. Instrum. **68**, 735 (1997).

15. R. Forties, *2000 Summer Research Program for High School Juniors at the University of Rochester's Laboratory for Laser Energetics*, Rochester, NY, LLE Report No. 319, LLE Document No. DOE/SF/19460-383 (2000).

16. V. Yu. Glebov, C. Stoeckl, T. C. Sangster, S. Roberts, G. J. Schmid, R. A. Lerche, and M. J. Moran, Rev. Sci. Instrum. **75**, 3559 (2004).

17. K. A. Fletcher, B. Apker, S. Hammond, J. Punaro, F. J. Marshall, J. Laine, and R. Forties, Rev. Sci. Instrum. **78**, 063301 (2007).

18. P. A. Jaanimagi, R. Boni, and R. L. Keck, Rev. Sci. Instrum. **72**, 801 (2001).

19. S. Chen and X. Yang, Opt. Eng. **46**, 097003 (2007).

Publications and Conference Presentations

Publications

S.-W. Bahk, E. Fess, B. E. Kruschwitz, and J. D. Zuegel, "A High-Resolution, Adaptive Beam-Shaping System for High-Power Lasers," Opt. Express **18**, 9151 (2010).

M. A. Barrios, D. G. Hicks, T. R. Boehly, D. E. Fratanduono, J. H. Eggert, P. M. Celliers, G. W. Collins, and D. D. Meyerhofer, "High-Precision Measurements of the Equation of State of Hydrocarbons at 1–10 Mbar Using Laser-Driven Shock Waves," Phys. Plasmas **17**, 056307 (2010).

Z. Bei, T. B. Jones, and D. R. Harding, "Electric Field Centering of Double-Emulsion Droplets Suspended in a Density Gradient," Soft Matter **6**, 2312 (2010).

R. Betti, P. Y. Chang, B. K. Spears, K. S. Anderson, J. Edwards, M. Fatenejad, J. D. Lindl, R. L. McCrory, R. Nora, and D. Shvarts, "Thermonuclear Ignition in Inertial Confinement Fusion and Comparison with Magnetic Confinement," Phys. Plasmas **17**, 058102 (2010).

P. Y. Chang, R. Betti, B. K. Spears, K. S. Anderson, J. Edwards, M. Fatenejad, J. D. Lindl, R. L. McCrory, R. Nora, and D. Shvarts, "Generalized Measurable Ignition Criterion for Inertial Confinement Fusion," Phys. Rev. Lett. **104**, 135002 (2010).

C. Dorrer and J. Bromage, "High-Sensitivity Optical Pulse Characterization Using Sagnac Electro-Optic Spectral Shearing Interferometry," Opt. Lett. **35**, 1353 (2010).

V. N. Goncharov, T. C. Sangster, T. R. Boehly, S. X. Hu, I. V. Igumenshchev, F. J. Marshall, R. L. McCrory, D. D. Meyerhofer, P. B. Radha, W. Seka, S. Skupsky, C. Stoeckl, D. T. Casey, J. A. Frenje, and R. D. Petrasso, "Demonstration of the Highest Deuterium-Tritium Areal Density Using Multiple-Picket Cryogenic Designs on OMEGA," Phys. Rev. Lett. **104**, 165001 (2010).

W. Guan and J. R. Marciante, "Power Scaling of Single-Frequency Hybrid Brillouin/Ytterbium Fiber Lasers," IEEE J. Quantum Electron. **46**, 674 (2010).

W. Guan and J. R. Marciante, "Single-Frequency Hybrid Brillouin/Ytterbium Fiber Laser with 1-W Output Power," in the *2010 Conference on Optical Fiber Communication and National Fiber Optic Engineers Conference* (IEEE, New York, 2010), Paper OThQ4.

S. X. Hu, "Optimizing the FEDVR-TDCC Code for Exploring the Quantum Dynamics of Two-Electron Systems in Intense Laser Pulses," Phys. Rev. E **81**, 056705 (2010).

S. X. Hu, B. Militzer, V. N. Goncharov, and S. Skupsky, "Strong Coupling and Degeneracy Effects in Inertial Confinement Fusion Implosions," Phys. Rev. Lett. **104**, 235003 (2010).

H. Irie and R. Sobolewski, "Terahertz Electrical Response of Nanoscale Three-Branch Junctions," J. Appl. Phys. **107**, 084315 (2010).

A. M. Kaplan, G. P. Agrawal, and D. N. Maywar, "Optical Square-Wave Clock Generation Based on an All-Optical Flip-Flop," IEEE Photonics Technol. Lett. **22**, 489 (2010).

J. P. Knauer, O. V. Gotchev, P. Y. Chang, D. D. Meyerhofer, O. Polomarov, R. Betti, J. A. Frenje, C. K. Li, M. J.-E. Manuel, R. D. Petrasso, J. R. Rygg, and F. H. Séguin, "Compressing Magnetic Fields with High-Energy Lasers," Phys. Plasmas **17**, 056318 (2010).

J. R. Marciante, R. G. Roides, V. V. Shkunov, and D. A. Rockwell, "Near-Diffraction-Limited Operation of Step-Index Large-Mode-Area Fiber Lasers Via Gain Filtering," Opt. Lett. **35**, 1828 (2010).

R. L. McCrory, D. D. Meyerhofer, S. J. Loucks, S. Skupsky, R. Betti, T. R. Boehly, M. J. Bonino, R. S. Craxton, T. J. B. Collins, J. A. Delettrez, D. H. Edgell, R. Epstein, V. Yu. Glebov, V. N. Goncharov, D. R. Harding, R. L. Keck, J. H. Kelly, T. J. Kessler, J. P. Knauer, L. D. Lund, D. Jacobs-Perkins, J. R. Marciante, J. A. Marozas, F. J. Marshall, A. V. Maximov, P. W. McKenty, S. F. B. Morse, J. Myatt, S. G. Noyes, P. B. Radha, A. Rigatti, T. C. Sangster, W. Seka, V. A. Smalyuk, J. M. Soures, C. Stoeckl, K. A. Thorp, L. J. Waxer, M. D. Wittman, B. Yaakobi, J. D. Zuegel, K. A. Fletcher, C. Freeman, S. Padalino, J. A. Frenje, C. K. Li, R. D. Petrasso, and F. H. Séguin, "Direct-Drive Inertial Fusion Research at the University of Rochester's Laboratory for Laser Energetics: A Review," in *Current Trends in International Fusion Research—Proceedings of the Sixth Symposium*, edited by E. Panarella and R. Raman (NRC Research Press, Ottawa, Canada), pp. 155–176.

C. Miao, J. C. Lambropoulos, and S. D. Jacobs, "Process Parameter Effects on Material Removal in Magnetorheological Finishing of Borosilicate Glass," Appl. Opt. **49**, 1951 (2010).

P. M. Nilson, S. P. D. Mangles, L. Willingale, M. C. Kaluza, A. G. R. Thomas, M. Tatarakis, R. J. Clarke, K. L. Lancaster, S. Karsch, J. Schreiber, Z. Najmudin, A. E. Dangor, and K. Krushelnick, "Plasma Cavitation in Ultraintense Laser Interactions with Underdense Helium Plasmas," New J. Phys. **12**, 045014 (2010).

J. Qiao, A. W. Schmid, L. J. Waxer, T. Nguyen, J. Bunkenburg, C. Kinglsey, A. Kozlov, and D. Weiner, "*In Situ* Detection and Analysis of Laser-Induced Damage on a 1.5-m Multilayer-Dielectric Grating Compressor for High-Energy, Petawatt-Class Laser Systems," Opt. Express **18**, 10,423 (2010).

T. C. Sangster, V. N. Goncharov, R. Betti, T. R. Boehly, D. T. Casey, T. J. B. Collins, R. S. Craxton, J. A. Delettrez, D. H. Edgell, R. Epstein, K. A. Fletcher, J. A. Frenje, V. Yu. Glebov, D. R. Harding, S. X. Hu, I. V. Igumenshchev, J. P. Knauer, S. J. Loucks, C. K. Li, J. A. Marozas, F. J. Marshall, R. L. McCrory, P. W. McKenty, D. D. Meyerhofer, P. M. Nilson, S. P. Padalino, R. D. Petrasso, P. B. Radha, S. P. Regan, F. H. Seguin, W. Seka, R. W. Short, D. Shvarts, S. Skupsky, V. A. Smalyuk, J. M. Soures, C. Stoeckl, W. Theobald, and B. Yaakobi, "Shock-Tuned Cryogenic-Deuterium-Tritium Implosion Performance on Omega," Phys. Plasmas **17**, 056312 (2010).

J. E. Schoenly, W. Seka, and P. Rechmann, "Selective Near-UV Ablation of Subgingival Dental Calculus: Measurement of Removal Rates," in *Lasers in Dentistry XVI*, edited by P. Rechmann and D. Fried (SPIE, Bellingham, WA, 2010), Vol. 7549, p. 754906.

V. A. Smalyuk, R. Betti, J. A. Delettrez, V. Yu. Glebov, D. D. Meyerhofer, P. B. Radha, S. P. Regan, T. C. Sangster, J. Sanz, W. Seka, C. Stoeckl, B. Yaakobi, J. A. Frenje, C. K. Li, R. D. Petrasso, and F. H. Séguin, "Implosion Experiments using Glass Ablators for Direct-Drive Inertial Confinement Fusion," Phys. Rev. Lett. **104**, 165002 (2010).

L. Sun, S. Jiang, and J. R. Marciante, "All-Fiber Optical Magnetic Field Sensor Based on Faraday Rotation," in the *2010 Conference on Optical Fiber Communication and National Fiber Optic Engineers Conference* (IEEE, New York, 2010), Paper OWL3.

L. Sun, S. Jiang, and J. R. Marciante, "Compact All-Fiber Optical Faraday Components Using 65-wt%-Terbium–Doped Fiber with a Record Verdet Constant of –32 rad/(Tm)," Opt. Express **18**, 12,191 (2010).

R. Yan, A. V. Maximov, and C. Ren, "The Linear Regime of the Two-Plasmon Decay Instability in Inhomogeneous Plasmas," Phys. Plasmas **17**, 052701 (2010).

Forthcoming Publications

J. Bromage, C. Dorrer, J. R. Marciante, M. J. Shoup III, and J. D. Zuegel, "Modal Measurement of a Large-Mode-Area Photonic-Crystal Fiber Amplifier Using Spatially Resolved Spectral Interferometry," to be published in Solid State Diode Laser Technology Review.

J. Bromage, C. Dorrer, and J. D. Zuegel, "Angular-Dispersion–Induced Spatiotemporal Aberrations in Noncollinear Optical Parametric Amplifiers," to be published in Optics Letters.

E. Glowacki, K. Horovitz, C. W. Tang, and K. L. Marshall, “Photoswitchable Gas Permeation Membranes Based on Liquid Crystals,” to be published in Advanced Functional Materials.

S. X. Hu, V. N. Goncharov, P. B. Radha, J. A. Marozas, S. Skupsky, T. R. Boehly, T. C. Sangster, D. D. Meyerhofer, and R. L. McCrory, “Two-Dimensional Simulations of the Neutron Yield in Cryogenic-DT Implosions on OMEGA,” to be published on Physics of Plasmas.

V. Kaushal, I. Iñiguez-de-la-Torre, H. Irie, G. Guarino, W. R. Donaldson, P. Ampadu, R. Sobolewski, and M. Margala, “A Study of Geometry Effects on the Performance of Ballistic Deflection Transistors,” to be published in IEEE Transactions on Nanotechnology.

J. C. Lambropoulos, C. Miao, and S. D. Jacobs, “Magnetic Field Effects on Shear and Normal Stresses in Magnetorheological Finishing,” to be published in Optics Express.

N. Marrocco, G. P. Pepe, A. Capretti, L. Parlato, V. Pagliarulo, G. Pleuso, A. Barone, R. Cristiano, M. Ejrnaes, A. Casaburi, N. Kashiwazaki, T. Taino, H. Myoren, and R. Sobolewski, “Strong Critical Current Density Enhancement in NiCu/NbN Superconducting Nanostripes for Optical Detection,” to be published in Applied Physics Letters.

P. W. McKenty, R. S. Craxton, F. J. Marshall, T. C. Sangster, J. A. Marozas, A. M. Cok, M. J. Bonino, D. R. Harding, D. D. Meyerhofer, R. L. McCrory, J. D. Kilkenny, A. Nikroo, J. Fooks, M. Hoppe, J. M. Edwards, A. J. MacKinnon, D. H. Munro, and R. J. Wallace, “Design of High-Neutron-Yield Polar-Drive Targets for Diagnostic Activation Experiments on the NIF,” to be published in the Journal of Physics: Conference Series.

A. A. Solodov, M. Storm, J. F. Myatt, R. Betti, D. D. Meyerhofer, P. M. Nilson, W. Theobald, and C. Stoeckl, “Simulations of Electron-Beam Transport in Solid-Density Targets and the Role of Magnetic Collimation,” to be published in the Journal of Physics, Conference Series.

L. Sun, S. Jiang, and J. R. Marciante, “All-Fiber Optical Faraday Mirror Using 56-wt%-Terbium-Doped Fiber,” to be published in IEEE Photonics Technology Letters.

L. Zeng, T. N. Blanton, and S. H. Chen, “Modulation of Phase Separation Between Spherical and Rod-Like Molecules Using Geometric Surfactancy,” to be published in Langmuir.

L. Zeng, C. W. Tang, and S. H. Chen, “Effects of Active Layer Thickness and Thermal Annealing on Polythiophene: Fullerene Bulk Heterojunction Photovoltaic Devices,” to be published in Applied Physics Letters.

Conference Presentations

W. T. Shmayda and J. E. Fair, “Humidity and Temperature-Stimulated Outgassing from Contaminated Metal Surfaces,” Hydrogen and Helium Isotopes in Materials, Oak Ridge, TN, 20–21 April 2010.

J. F. Myatt, J. A. Delettrez, A. V. Maximov, D. D. Meyerhofer, R. W. Short, C. Stoeckl, M. Storm, S. C. Wilks, and H. Chen, “Optimizing Pair Production on Kilojoule-Class Lasers,” Workshop on Antimatter Using Intense Lasers, Berkeley, CA, 27–28 April 2010.

The following presentations were made at the OMEGA Laser Facility Users Workshop, Rochester, NY, 28–30 April 2010:

M. A. Barrios, D. G. Hicks, T.R. Boehly, D. E. Fratanduono, J. H. Eggert, P. M. Celliers, G. W. Collins, and D. D. Meyerhofer, “High-Precision Measurements of the Equation of State of Hydrocarbons at 1- to 10-Mbar Using Laser-Driven Shock Waves.”

C. Dorrer, D. Irwin, A. Consentino, and J. Qiao, “OMEGA EP Temporal Contrast Measurements.”

G. Fiksel, R. Jungquist, P. M. Nilson, W. Theobald, and C. Stoeckl, "Development of a Spherical Crystal X-Ray Imaging Diagnostic for OMEGA and OMEGA EP."

D. E. Fratanduono, M. A. Barrios, T. R. Boehly, D. D. Meyerhofer, J. H. Eggert, R. Smith, D. G. Hicks, P. M. Celliers, and G. W. Collins, "Measures of Strain-Induced Refractive-Index Changes in Ramp-Compressed Lithium Fluoride."

J. D. Hager, V. A. Smalyuk, S. X. Hu, D. D. Meyerhofer, and T. C. Sangster, "Rayleigh–Taylor Measurements in Planar CH and SiO_2 Foils on OMEGA."

B. E. Kruschwitz, S.-W. Bahk, J. Bromage, D. Irwin, and M. Moore, "On-Shot Focal-Spot Characterization on OMEGA EP."

S. F. B. Morse, "Facility Overview and Progress on 2009 OLUG Recommendations."

P. M. Nilson, R. Betti, J. A. Delettrez, L. Gao, P. A. Jaanimagi, J. F. Myatt, T. C. Sangster, A. A. Solodov, C. Stoeckl, W. Theobald, B. Yaakobi, J. D. Zuegel, A. J. Mackinnon, P. K. Patel, K. Akli, L. Willingale, and K. M. Krushelnick, "Intense-Energy Coupling with Multikilojoule, 10-ps Pulses on OMEGA EP."

G. Pien, "Diagnostic Qualification and Infrastructure Update."

W. Theobald, W. Seka, M. Bedzyk, R. Boni, R. Brown, R. S. Craxton, S. Ivancic, P. M. Nilson, J. Puth, A. V. Okishev, R. G. Roides, T. C. Sangster, C. Stoeckl, T. Duffy, D. Weiner, and J. Zuegel, "Fourth-Harmonic Probe Diagnostic for OMEGA EP."

K. A. Thorp, "Omega Facility Status and Performance Update."

The following presentations were made at the 18th Topical Conference on High-Temperature Plasma Diagnostics, Wildwood, NJ, 16–20 May 2010:

D. H. Edgell, W. Seka, V. N. Goncharov, I. V. Igumenshchev, R. S. Craxton, J. A. Delettrez, J. F. Myatt, A. V. Maximov, T. C. Sangster, and R. W. Short, R. E. Bahr, "Time-Resolved Scattered-Light Spectroscopy in Direct-Drive-Implosion Experiments on OMEGA."

G. Fiksel, C. Freeman, J. A. Frenje, J. C. Mileham, P. M. Nilson, N. Sinenian, C. Stoeckl, and W. Theobald, "Characterization of Composition and Energy Spectra of Laser-Produced Ions with Thomson Parabola."

V. Yu. Glebov, T. C. Sangster, C. Stoeckl, J. P. Knauer, W. Theobald, K. L. Marshall, M. J. Shoup III, T. Buczek, M. Cruz, T. Duffy, M. Romanofsky, M. Fox, A. Pruyne, M. J. Moran, R. A. Lerche, J. McNaney, J. D. Kilkenny, M. Eckart, D. Schneider, D. Munro, W. Stoeffl, R. A. Zacharias, J. J. Haslam, T. Clancy, M. Yeoman, D. Warwas, C. J. Horsfield, J.-L. Bourgade, O. Landoas, L. Disdier, G. A. Chandler, and R. J. Leeper, "The National Ignition Facility Neutron Time-of-Flight System and Its Initial Performance" (invited).

F. J. Marshall, T. DeHaas, and V. Yu. Glebov, "Charge-Injection-Device Performance in the High-Energy-Neutron Environment of Laser-Fusion Experiments."

C. Stoeckl, M. Cruz, V. Yu. Glebov, J. P. Knauer, R. Lauck, K. L. Marshall, C. Mileham, T. C. Sangster, and W. Theobald, "A Gated Liquid-Scintillator–Based Neutron Detector for Fast-Ignitor Experiments and Down-Scattered Neutron Measurements."

The following presentations were made at CLEO 2010, San Jose, CA, 16–21 May 2010:

J. Bromage, C. Dorrer, and J. D. Zuegel, "Eliminating Spatio-temporal Distortions from Angular Dispersion in Noncollinear Optical Parametric Amplifiers."

C. Dorrer, D. Irwin, A. Consentino, and J. Qiao, "Contrast Measurements of Kilojoule Laser Pulses at the Omega Laser Facility."

B. E. Kruschwitz, S.-W. Bahk, J. Bromage, D. Irwin, M. Moore, L. J. Waxer, J. D. Zuegel, and J. H. Kelly, "Improved On-Shot Focal-Spot Diagnosis on the OMEGA EP Short-Pulse Laser System."

J. Qiao, L. J. Waxer, T. Nguyen, J. Bunkenburg, C. Kingsley, J. H. Kelly, A. W. Schmid, and D. Weiner, "*In-Situ* Detection and Analysis of Laser-Induced Damage on a 1.5-m Multilayer-Dielectric Grating Compressor for High-Energy, Petawatt-Class Laser Systems."

R. C. G. Smith, A. M. Sarangan, and J. R. Marciante, "Direct Measurement of Bend-Induced Mode Deformation Using a Helical-Core Fiber."

L. Sun, S. Jiang, and J. R. Marciante, "A Compact All-Fiber Optical Faraday Mirror."

M. Vargas, Z. Zhao, K. L. Marshall, and C. Dorrer, "Optically Patterned Liquid Crystal Devices for High-Resolution Beam Shaping."

R. Xin and J. D. Zuegel, "Generation of CPA Seed Pulse by Direct Phase Modulation."

J. D. Zuegel, "Laser Fusion for Laser Jocks: Basic Principles of a Laser Application Meeting a Grand Challenge," CLEO Applications, San Jose, CA, 16–21 May 2010 (invited tutorial).

The following presentations were made at Optical Interference Coatings, Tucson, AZ, 6–11 June 2010:

K. L. Marshall, E. Glowacki, C. Sileo, L. Chockalingam, J. Lee, V. Guiliano, and A. Rigatti, "Improving the Abrasion Resistance of Organosilane-Modified Sol-Gel Coatings for High-Peak-Power Laser Applications."

J. B. Oliver, P. Kupinski, A. L. Rigatti, A. W. Schmid, J. C. Lambropoulos, S. Papernov, A. Kozlov, and R. D. Hand "Modification of Stresses in Evaporated Hafnia Coatings for Use in Vacuum."

J. B. Oliver, P. Kupinski, A. L. Rigatti, A. W. Schmid, J. C. Lambropoulos, S. Papernov, A. Kozlov, and R. D. Hand "Stress Compensation in Hafnia/Silica Optical Coatings by Inclusion of Alumina Layers."

J. B. Oliver, P. Kupinski, A. L. Rigatti, A. W. Schmid, J. C. Lambropoulos, S. Papernov, A. Kozlov, J. Spaulding, D. Sadowski, Z. Chrzan, R. D. Hand, D. R. Gibson, I. Brinkley, and F. Placido, "Large-Aperture Plasma-Assisted Deposition of ICF Laser Coatings."

A. L. Rigatti, J. B. Oliver, P. Kupinski, H. Floch, E. Lavastre, G. Ravel, and F. Geffraye, "CEA Deformable-Mirror Coating Test Results."

J. F. Myatt, R. Betti, J. A. Delettrez, L. Gao, P. A. Jaanimagi, A. V. Maximov, D. D. Meyerhofer, T. C. Sangster, R. W. Short, C. Stoeckl, M. Storm, W. Theobald, B. Yaakobi, J. D. Zuegel, S. C. Wilks, A. J. MacKinnon, P. K. Patel, H. Chen, and K. Akli, "High-Intensity Laser-Matter Interaction Experiments on the Kilojoule-Class OMEGA EP Laser," 2010 Canadian Association of Physicists Congress, Toronto, Canada, 7–11 June 2010.

The following presentations were made at Optical Fabrication and Testing, Jackson Hole, WY, 13–17 June 2010:

S. N. Shafrir, H. J. Romanofsky, M. D. Skarlinski, M. Wang, C. Miao, S. Salzman, T. Chartier, J. Mici, J. C. Lambropoulos, R. Shen, H. Yanh, and S. D. Jacobs, "Corrosion Resistant Zirconia Coated Carbonyl Iron Particle-Based Magnetorheological Fluid."

M. D. Skarlinski and S. D. Jacobs, "Modifying the Rheological Properties of Zirconia Coated Carbonyl Iron Suspensions Through Acid-Base Titration and the Addition of Di-Ammonium Citrate."

The following presentations were made at the 40th Annual Anomalous Absorption Conference, Snowmass Village, CO, 13–18 June 2010:

T. J. B. Collins, J. A. Marozas, S. Skupsky, P. W. McKenty, V. N. Goncharov, P. B. Radha, R. S. Craxton, F. J. Marshall, R. Epstein, D. Jacobs-Perkins, and A. Shvydky, "Preparing for Polar Drive at the National Ignition Facility."

D. H. Edgell, J. F. Myatt, W. Seka, J. A. Delettrez, A. V. Maximov, R. W. Short, and R. E. Bahr, "Anistropic Distribution of Hard X Rays from the Two-Plasmon-Decay Hot-Electron Distribution."

M. G. Haines, J. A. Delettrez, J. F. Myatt, A. A. Solodov, T. J. B. Collins, and J. A. Marozas, "Electrothermally Generated Filaments in Laser–Solid Interactions."

S. X. Hu, V. N. Goncharov, P. B. Radha, J. A. Marozas, S. Skupsky, T. R. Boehly, T. C. Sangster, D. D. Meyerhofer, and R. L. McCrory, "Two-Dimensional Radiation-Hydrodynamic Simulations of Cryogenic-DT Implosions at the Omega Laser Facility."

A. V. Maximov, J. F. Myatt, R. W. Short, R. Yan, and W. Seka, "Modeling of Two-Plasmon-Decay Instability in the Plasmas of Direct-Drive Inertial Confinement Fusion."

J. F. Myatt, J. A. Delettrez, W. Seka, D. H. Edgell, A. V. Maximov, R. W. Short, D. F. DuBois, D. A. Russell, and H. X. Vu, "Calculations of Preheat Caused by the Two-Plasmon-Decay Instability in Direct-Drive ICF Plasmas."

W. Seka, D. H. Edgell, J. F. Myatt, R. S. Craxton, A. V. Maximov, and R. W. Short, "SBS, SRS, and TPD in Planar Target Experiments Relevant to Direct-Drive ICF."

R. W. Short, "Anistropy of Collectively Driven Two-Plasmon Decay in Direct-Drive Spherical Irradiation Geometry."

H. X. Vu, D. F. DuBois, D. A. Russell, J. F. Myatt, and W. Seka, "Hot-Electron Generation by the Two-Plasmon-Decay Instability in Inhomogeneous Plasmas."

P. B. Radha, R. Betti, T. R. Boehly, J. A. Delettrez, V. N. Goncharov, I. V. Igumenshchev, J. P. Knauer, J. A. Marozas, F. J. Marshall, R. L. McCrory, D. D. Meyerhofer, S. P. Regan, T. C. Sangster, W. Seka, S. Skupsky, A. A. Solodov, C. Stoeckl, W. Theobald, J. A. Frenje, D. T. Casey, C. K. Li, and R. D. Petrasso, "Inertial Confinement Fusion Using the OMEGA Laser," 37th International Conference on Plasma Science, Norfolk, VA, 20–24 June 2010.

UNIVERSITY *of* ROCHESTER